

DISSERTATION

IMAGING INDIVIDUAL BARIUM ATOMS IN SOLID XENON BY SCANNING OF A
FOCUSED LASER FOR USE IN THE NEXO EXPERIMENT

Submitted by
Christopher Chambers
Department of Physics

In partial fulfillment of the requirements
For the Degree of Doctor of Philosophy
Colorado State University
Fort Collins, Colorado
Spring 2019

Doctoral Committee:

Advisor: William Fairbank

Siu Au Lee
Robert J. Wilson
Alan Van Orden

Copyright by Christopher Chambers 2019

All Rights Reserved

ABSTRACT

IMAGING INDIVIDUAL BARIUM ATOMS IN SOLID XENON BY SCANNING OF A FOCUSED LASER FOR USE IN THE NEXO EXPERIMENT

Neutrinoless double beta decay ($0\nu\beta\beta$) is a non-standard model decay process in which two simultaneous beta decays occur, with no emission of neutrinos. This decay is of great interest. If observed, it will demonstrate that the neutrino and anti-neutrino are not distinct. This decay also violates lepton number conservation, a requirement for some theories seeking to explain the matter-antimatter asymmetry of the universe. A measurement of the decay half-life will also give information on the absolute mass scale of the neutrinos. EXO-200 and nEXO use liquid xenon (LXe) time projection chambers (TPC) to search for $0\nu\beta\beta$ decay. EXO-200 first observed two neutrino double beta decay ($2\nu\beta\beta$) in xenon-136, the rarest decay ever observed. A low background measurement is vital to maximizing sensitivity to the $0\nu\beta\beta$ decay mode, yet to be observed. In this dissertation, research and development of a technique for positive identification of the barium-136 daughter (barium tagging) is presented. It is desirable to incorporate barium tagging into the future nEXO detector, as it provides discrimination against all background except for the $2\nu\beta\beta$ decay mode. The scheme being developed in this work involves extraction of the barium daughter in solid xenon with a cryogenic probe, followed by matrix-isolation fluorescence spectroscopy to tag the barium atom. This work focuses on the detection of individual barium atoms in a prepared solid xenon sample. Single atom sensitivity has been achieved, and a method for imaging of individual atoms by scanning of a focused laser has been demonstrated.

ACKNOWLEDGEMENTS

I would first and foremost like to thank my advisor, Prof. William Fairbank. His guidance, support and vision have given me the opportunity to grow as a physicist and pursue truly fundamental research in my graduate studies. His persistence and thoroughness as a scientist has made this thesis possible, and has set an excellent example for many students, myself included. Working with Prof. Fairbank has truly inspired me to pursue a career in exciting scientific research.

I especially thank Tim Walton for mentoring me on how to be effective in the lab and develop my skills as an experimentalist. I also thank him for many years of development of the apparatus used in this thesis. I thank Adam Craycraft and Jon Gilbert for many hours of fruitful discussion and companionship throughout my time here. I thank David Fairbank, James Todd and Danielle Yahne for their help in collecting data and running the experiment.

I would also like to thank my committee members, Profs. Siu Au Lee, Robert Wilson and Alan Van Orden. I especially thank Prof. Lee for her insightful conversations. I also thank the nEXO collaboration for their hard work developing an ambitious experiment, with which I am excited to be involved. This work was supported by the National Science Foundation under grant number PHY-1649324 and the Department of Energy under award number DE-FG02-03ER41255.

Finally, I thank my family for their unwavering support and encouragement throughout my life and especially as a graduate student. Without them, I would not have had the amazing opportunities to pursue my goals.

DEDICATION

to my parents, Will and Becky

TABLE OF CONTENTS

ABSTRACT	ii
ACKNOWLEDGEMENTS	iii
DEDICATION	iv
LIST OF TABLES	vii
LIST OF FIGURES	viii
Chapter 1 Introduction	1
1.1 Neutrinos	2
1.1.1 Neutrino Mass	2
1.1.2 Neutrinoless Double Beta Decay	5
1.2 Enriched Xenon Observatory	9
1.2.1 EXO-200	10
1.2.2 nEXO	16
1.3 Barium Tagging	19
1.3.1 Ba Fluorescence Tagging in Solid Xenon at CSU	20
Chapter 2 Theory	24
2.1 Barium Spectroscopy	24
2.1.1 Ba Transitions in Vacuum	24
2.2 Matrix Isolation Spectroscopy	25
2.2.1 Shifts of Transitions in SXe Matrix	26
2.2.2 Barium Guest Atom Sites in Xenon	28
2.2.3 Bleaching of Barium Fluorescence	34
2.3 Fluorescence Efficiency	36
2.4 Signal Models of Ba Atom Images	38
2.4.1 Fixed Laser Image Simulation	39
2.4.2 Laser Scan Simulations	40
2.4.3 Scanned Laser Image Simulation	42
Chapter 3 Experimental Apparatus and Method	45
3.1 Ion Deposition System	45
3.1.1 Ion Source	45
3.1.2 Mass Filter	47
3.1.3 Beam Focusing and Steering	50
3.1.4 Ion Beam Measurements	51
3.1.5 Ion Beam Pulsing	52
3.1.6 Calibration of Ion Deposits	55
3.2 Deposition of Ba ⁺ Ions into SXe Matrix	61
3.3 Laser Excitation System	64
3.3.1 Laser Scanning	67
3.4 Fluorescence Collection System	69

3.5	Imaging Analysis	70
3.5.1	Fixed Laser Analysis	70
3.5.2	Scanned Image Analysis	72
3.6	Laser Spot Size Determination	73
3.6.1	Ray Matrix Calculation	73
3.6.2	Gaussian Fit to Composite Images	76
3.7	Cryostat Vibration Compensation	77
3.7.1	Sapphire Background Reduction by Pre-Bleaching	82
Chapter 4	Results	86
4.1	Imaging of Ba Atoms with a Fixed Laser	86
4.2	Imaging of Ba Atoms with a Scanned Laser	90
4.3	Ba Fluorescence Turn-off	93
4.4	Additional Ba Scan and Fluorescence Turn-off Experiments	97
4.4.1	Scan Results	98
4.4.2	Additional Fluorescence Turn-off Results	103
Chapter 5	Conclusions	109
5.1	Future Work	110
Bibliography	112

LIST OF TABLES

1.1	Best-fit values for measured oscillation parameters	4
2.1	Wavelengths and decay rates of Ba atoms in vacuum.	25
2.2	Table of atom locations and fluorescence from simulated scans	44
3.1	Nominal parameters for E×B filter elements.	50
3.2	Nominal voltages on ion beam steering and focusing elements.	51
3.3	Values of ion beam deflection per volt of plate bias	55
3.4	Ba ⁺ ion beam fit parameters	57
3.5	Comparison of collected charge with Faraday cup electrodes biased	60
3.6	Ba ⁺ ion beam fit parameters for Faraday cup 4 replacement	60
3.7	Table of the quantities used in the ray matrix calculation	75
3.8	Laser spot sizes from fits to scanned images	77
4.1	Summary of SXe-only background laser scans	99
4.2	Table of data for each single Ba atom fluorescence peak observed	102
4.3	Fluorescence rates and efficiencies for all Ba atoms observed	103
4.4	Persistence times and the corresponding laser exposure	107
4.5	Collected photons and signal significance of Ba atom fluorescence	108

LIST OF FIGURES

1.1	Normal and Inverted hierarchies with flavor mixing	5
1.2	Double beta decay Feynman diagrams	6
1.3	Double beta decay energy spectrum with $0\nu\beta\beta$ contribution	7
1.4	Plot of effective neutrino mass with minimum neutrino mass for both mass hierarchies	8
1.5	Energy level diagram for $\beta\beta$ decay in ^{136}Xe	9
1.6	EXO-200 TPC instrumentation schematic	10
1.7	Anti-correlation of scintillation and charge signals with rotated energy shown	11
1.8	Cut-away drawing of the EXO-200 detector	12
1.9	Picture of the charge collection and APD planes in the EXO-200 detector	13
1.10	Drawing of the EXO-200 shielding scheme	14
1.11	Energy spectrum for $2\nu\beta\beta$ decay in EXO-200 detector	15
1.12	Energy spectrum for $0\nu\beta\beta$ decay search in EXO-200 detector	16
1.13	Drawing of the proposed nEXO detector	18
1.14	Drawing of the proposed nEXO detector in the SNOLAB cryopit	19
1.15	nEXO sensitivity with respect to $0\nu\beta\beta$ half-life and effective neutrino mass	19
1.16	Concept of Ba/SXe extraction via cryogenic probe	21
1.17	Conceptual drawing of the cryogenic extraction and fluorescence tagging probe under development at CSU	22
1.18	nEXO sensitivity with respect to $0\nu\beta\beta$ half-life with Ba-tagging implemented	23
2.1	Level diagram for neutral Ba	26
2.2	Illustration of the Franck-Condon Principle	28
2.3	Emission of Ba atoms in SXe for three excitation wavelengths	29
2.4	Excitation spectra for emission lines of Ba in SXe	30
2.5	Potential curves for Xe-Xe and alkaline earth metal-Xe interactions	31
2.6	Drawing of the 4- and 5-vacancy sites in SXe attributed to the 591 nm and 577 nm lines respectively	33
2.7	Cartoon of single vacancy site formation by Ba^+ implantation in solid Xe	33
2.8	Fluorescence spectra showing the relative bleaching rates of the dominant Ba emission lines	34
2.9	Calculated potentials for the excited states of the Ba-Xe system	36
2.10	Estimated absorption cross section for Ba atoms in SXe	38
2.11	Sample images of Ba atom placement in simulation	40
2.12	Modeled Ba atom response	40
2.13	Simulated laser grid intensity map	41
2.14	Laser coverage and overlap as a function of scan grid spacing	42
2.15	Composite images of simulated laser scans	44
3.1	Schematic of full ion beam system	46
3.2	Drawing of the barium ion source	47

3.3	Drawing of the Colutron 6" Wien ($E \times B$) mass filter (now Beam Imaging Solutions Model 600-B)	48
3.4	Cylindrical focusing of ions by a Wien ($E \times B$) filter.	49
3.5	CAD drawing of Faraday cup 4	52
3.6	Simplified circuit diagram for the preamplifiers used for reading out ion pulse signals.	54
3.7	Raw and reconstructed signals of ion pulses into Faraday cup 4.	54
3.8	Fitted profiles of the Ba^+ ion beam for cups 4 and w in the horizontal and vertical directions	56
3.9	Comparison of simulated Faraday cup profiles with different entry aperture sizes	57
3.10	Simulation of three Ba^+ ion beam positions and the collected area	58
3.11	Fitted profiles of the Ba^+ ion beam for cups 4 and w in the horizontal and vertical directions after replacement of cup 4	61
3.12	Sample deposition window geometry	62
3.13	Diagram of set-up for interference fringe measurement	63
3.14	Interference fringes for different needle valve settings	63
3.15	RGA data of SXe deposit melt	64
3.16	Schematic diagram of optical setup for Ba fluorescence detection	65
3.17	Plot of laser spot size extracted from fit to CCD images vs. lens position	66
3.18	Schematic representation of the scanning technique	68
3.19	Example image of fluorescence signal collected.	69
3.20	Examples of integration region selection	71
3.21	Schematic diagram of partial pixel integration	71
3.22	Fits to razor-blade profiles of the excitation laser at the focusing lens	73
3.23	Diagram of the optical components used in the ray matrix calculation of laser spot size	74
3.24	Comparison of data and fit for laser width fit by direct 2D Gaussian	77
3.25	Circuit diagram for processing piezo-accelerometer signal.	78
3.26	Sample signal from piezo-accelerometer with laser gate	79
3.27	Dust spot location during one period of cryostat vibration	81
3.28	Un-gated and gated laser coverage simulations	82
3.29	Image of the sapphire window illuminated by the excitation laser	83
3.30	Scanned image showing the photo-bleaching of the sapphire surface background	84
4.1	Plot of 619 nm Ba fluorescence vs. Ions in observation region	88
4.2	SXe-only background difference vs. Ba^+ ions deposited in previous sample.	89
4.3	Series of four images as the laser passes over a Ba atom in a scan	91
4.4	Images of a Ba peak showing the signal is mostly localized to one pixel	91
4.5	Composite images of two SXe-only deposits surrounding a Ba/SXe deposit.	92
4.6	Plot of fluorescence vs. time for a Ba atom and backgrounds	94
4.7	Composite images of Ba/SXe scans before and after fluorescence turn-off	95
4.8	3D plots of the composite images of one SXe-only and two different Ba/SXe deposits.	96
4.9	Plot of fluorescence vs. time for a second Ba atom	97
4.10	Examples of SXe-only background composite images for each experiment day	98
4.11	Two composite images of Ba/SXe deposits on 13 June 2018	100
4.12	Two composite images of Ba/SXe deposits on 14 June 2018	100
4.13	Two composite images of Ba/SXe deposits on 20 June 2018	101

4.14	Two composite images of Ba/SXe deposits on 21 June 2018	101
4.15	Ba Fluorescence vs. time for the 4 atoms observed on 13 June 2018.	104
4.16	Ba Fluorescence vs. time for the 4 atoms observed on 14 June 2018.	104
4.17	Ba Fluorescence vs. time for the 4 atoms observed on 20 June 2018.	105
4.18	Ba Fluorescence vs. time for the 4 atoms observed on 21 June 2018.	105

Chapter 1

Introduction

Neutrinos are elusive fundamental particles that interact only via the weak and gravitational forces, and as such interact very rarely with matter. This trait makes them difficult to study, however the last decades have seen ever more sensitive detectors built to precisely measure the behavior and properties of neutrinos. Neutrinos were first postulated by Wolfgang Pauli in 1930 to solve the problem of apparent energy non-conservation in beta decay. When a nucleus undergoes beta decay, a neutron decays to a proton, electron (beta particle), and the then unknown anti-neutrino. It was expected that the electrons produced in β decay would be mono-energetic, having the same energy as the change in nuclear energy, but experiments found a broad energy spectrum [1]. This led to the proposal of a neutral, undetected particle that carries away the missing energy of the decay. The neutrino was incorporated into the model of beta decay in 1934 by Enrico Fermi [2], establishing the beginning of weak interaction theory, and giving a framework for the detection and measurement of the neutrino. The elusive neutrino remained undetected until 1956, when Clyde Cowan and Fred Reines observed inverse beta decay in water resulting from electron anti-neutrinos produced by the nuclear reactor at the Savannah River Plant in South Carolina [3].

After the successful detection of reactor-generated neutrinos, larger and more sophisticated detectors were constructed to measure the neutrinos produced in the sun. Four such experiments, the Homestake Solar Neutrino Detector [4], Kamiokande [5], SAGE [6] and GALLEX [7] measured a significantly lower flux of solar neutrinos than predicted by solar models. The neutrino had been incorporated into the standard model of particle physics (SM) as massless fundamental particles of three flavors, partnering with the heavy leptons (electron, muon and tau particles). If the neutrinos have mass, they may change flavor over time, resulting in the observed lower flux of electron neutrinos from the sun. The SNO experiment [8, 9] was the first to offer evidence of this flavor oscillation in solar neutrinos in 2002, and neutrinos produced by cosmic rays striking the atmosphere had also been shown to oscillate by the Super-Kamiokande experiment in 1998 [10, 11].

These oscillation experiments, as well as many following them, have demonstrated that at least two neutrinos have a non-zero mass. This evidence of physics beyond the standard model opens exciting possibilities for neutrino experiments to explore.

Another potential property of a neutrino is for it to be its own anti-particle (called a Majorana particle), since it is chargeless. This would be unique among fundamental fermions, and could provide insight into the matter-antimatter asymmetry of the universe [12, 13]. The process of neutrinoless double beta decay ($0\nu\beta\beta$) is a direct search for the Majorana nature of neutrinos, as well as lepton number non-conservation. The EXO-200 experiment is a $0\nu\beta\beta$ search using ^{136}Xe decaying to ^{136}Ba , and has set a competitive limit on the neutrino mass of $\langle m_{\beta\beta} \rangle > 147 - 398$ meV [14] depending on the matrix element calculation used. nEXO is the proposed successor, using a larger mass and improved instrumentation to probe for $0\nu\beta\beta$ decay. The focus of this dissertation is a technique for detection of the ^{136}Ba daughter using fluorescence imaging in solid Xe. The implementation of a "barium tagging" technique to the nEXO detector would provide a nearly background-free measurement of $0\nu\beta\beta$, as well as an additional signature of the decay [15].

1.1 Neutrinos

Neutrinos carry no electromagnetic or color charge, and thus only interact via the weak force and gravity. They are partners to the charged leptons and come in three flavors, ν_e , ν_μ , and ν_τ . The flavor is defined by the charged lepton it accompanies in a weak interaction. Thus an electron anti-neutrino is produced with the electron and so on. These states are the eigenstates of the flavor basis. In the standard model, neutrinos were assumed to be massless, since their very small mass differences were unknown at the time.

1.1.1 Neutrino Mass

The fact that neutrinos have mass has been established by neutrino oscillation experiments, but the value of the masses are yet to be determined. Neutrinos exist in eigenstates of definite mass (ν_1, ν_2, ν_3) when propagating in space, and this forms a basis for describing their behavior. This

mass basis is not the same as the flavor basis, and this leads to mixing of neutrino flavor states, similar to the quark sector. The flavor states can be written in the mass basis as

$$|\nu_\alpha\rangle = \sum_{j=1}^3 U_{\alpha j}^* |\nu_j\rangle, \quad (1.1)$$

where $U_{\alpha j}$ is the Pontecorvo-Maki-Nakagawa-Sakata (PMNS) matrix. This 3-vector mixing matrix $U_{\alpha j}$ is described by 3 mixing angles (θ_{12} , θ_{13} , and θ_{23}), a Dirac CP-violating phase (δ), and 2 Majorana CP-violating phases (α_1 , and α_2). A standard parameterization of this matrix is

$$U = \begin{pmatrix} 1 & 0 & 0 \\ 0 & c_{23} & s_{23} \\ 0 & -s_{23} & c_{23} \end{pmatrix} \begin{pmatrix} c_{13} & 0 & s_{13}e^{i\delta} \\ 0 & 1 & 0 \\ -s_{13}e^{i\delta} & 0 & c_{13} \end{pmatrix} \begin{pmatrix} c_{12} & s_{12} & 0 \\ -s_{12} & c_{12} & 0 \\ 0 & 0 & 1 \end{pmatrix} \begin{pmatrix} 1 & 0 & 0 \\ 0 & e^{i\alpha_1} & 0 \\ 0 & 0 & e^{i\alpha_2} \end{pmatrix}, \quad (1.2)$$

$$\text{where } c_{ij} = \cos(\theta_{ij}) \text{ and } s_{ij} = \sin(\theta_{ij})$$

This mixing of flavor states leads to oscillation of the probability of detecting a given flavor with respect to time. To demonstrate this, a two-neutrino approximation without CP-violating phases can be used. This model has only one mixing angle, θ , and the mixing matrix is simply

$$U = \begin{pmatrix} \cos(\theta) & \sin(\theta) \\ -\sin(\theta) & \cos(\theta) \end{pmatrix} \quad (1.3)$$

Assuming we start with a pure ν_e state, the time-evolved state of the neutrino can be written in the mass basis as

$$|\nu_e(t)\rangle = \cos(\theta)e^{-iE_1t} |\nu_1\rangle + \sin(\theta)e^{-iE_2t} |\nu_2\rangle \quad (1.4)$$

projected into the flavor basis, it becomes

$$|\nu(t)\rangle = (\cos^2(\theta)e^{-iE_1t} + \sin^2(\theta)e^{-iE_2t}) |\nu_e\rangle + \sin(\theta)\cos(\theta)(e^{-iE_1t} - e^{-iE_2t}) |\nu_\mu\rangle \quad (1.5)$$

The energies E_1 and E_2 are the energies associated with the mass states. The probability of observing the ν_μ state is

$$P(\nu_e \rightarrow \nu_\mu) = |\langle \nu_\mu | \nu_e(t) \rangle|^2 = \sin^2(2\theta) \sin^2\left(\frac{E_2 - E_1}{2}t\right) \quad (1.6)$$

Due to the very small mass of the neutrino relative to its momentum and assuming a specific momentum for the particle, the energy difference can be approximated as

$$E_2 - E_1 \approx \frac{m_2^2 - m_1^2}{2E} = \frac{\Delta m^2}{2E} \quad (1.7)$$

Combining this with equation (1.6), the oscillation of the probability of flavor change is related to both the mixing angle and the mass square difference. These mass splittings are written as $\Delta m_{ij}^2 = m_i^2 - m_j^2$ with $i, j = 1, 2, 3$ for the full three neutrino solution. The measurement of these parameters have been undertaken by many experiments throughout the last 30 years. For example, the observation of muon neutrino appearance in atmospheric neutrinos is sensitive to θ_{12} and Δm_{12}^2 . The current best measurements as compiled by the particle data group are given in Table 1.1 [16].

Table 1.1: Best-fit oscillation parameters from a global fit of all experimentally determined values. Note that some parameters depend on the mass hierarchy (NH or IH), and the atmospheric mass parameter is defined as $|\Delta m^2| = m_3^2 - \frac{m_2^2 - m_1^2}{2}$. Values obtained from particle data group (PDG) tables [16]

Parameter	Best Fit	3σ Range
$\Delta m_{21}^2 [10^{-5} eV^2]$	7.37	6.93 - 7.97
$ \Delta m^2 [10^{-3} eV^2]$ (NH)	2.50	2.37 - 2.63
$ \Delta m^2 [10^{-3} eV^2]$ (IH)	2.46	2.33 - 2.60
$\sin^2(\theta_{12})$	0.297	0.250 - 0.354
$\sin^2(\theta_{23}), \Delta m^2 > 0$	0.437	0.379 - 0.616
$\sin^2(\theta_{23}), \Delta m^2 < 0$	0.569	0.383 - 0.637
$\sin^2(\theta_{13}), \Delta m^2 > 0$	0.0214	0.0185 - 0.0246
$\sin^2(\theta_{13}), \Delta m^2 < 0$	0.0218	0.0186 - 0.0248
δ/π (NH)	1.35	0.92 - 1.99
δ/π (IH)	1.32	0.83 - 1.99

Since the absolute value of the Δm^2 parameter is unknown, there are two possibilities for the ordering of the neutrino mass states. These are called the "normal" (NH) and "inverted" (IH) hierarchies and are shown in Figure 1.1. Oscillation experiments demonstrate that the neutrinos have mass, but are only sensitive to the mass-square differences. To measure the absolute mass of the neutrinos, other approaches must be used. Cosmological studies done by the Planck collaboration set a limit on the sum of the neutrino masses of $\sum_i m_i < 0.12$ eV [17]. The KATRIN experiment aims to measure the endpoint discrepancy of tritium decay, with an expected sensitivity of $m_{\bar{\nu}_e} < 0.2$ eV [18]. The next section will discuss the possibility of accessing the absolute neutrino masses via observation of neutrinoless double beta decay.

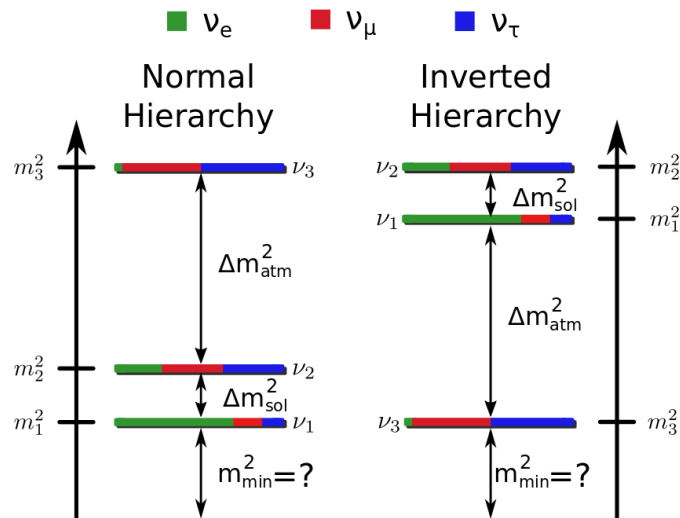


Figure 1.1: A depiction of the two mass hierarchies and the mass square differences (not to scale). The colors represent the mixing of the flavor states in the mass basis.

1.1.2 Neutrinoless Double Beta Decay

Double beta ($\beta\beta$) decay is a process in which two beta decays occur simultaneously in one nucleus. This is a second-order process and can be observed in even-even nuclei for which single beta decay is energetically forbidden. In the two-neutrino ($2\nu\beta\beta$, left in Fig. 1.2) mode, two neutrons decay to two protons and two electrons, with two anti-electron neutrinos produced [19]. As

in single beta decay, the production of neutrinos causes the observed energy of the decay products to be distributed in a continuous spectrum up to the Q-value of the decay. Neutrinoless double beta decay ($0\nu\beta\beta$, right in Figure 1.2) is a non-standard model process in which the neutrino is exchanged as a virtual particle in the decay. In this case, the neutrino is its own anti-particle (a Majorana particle), and lepton number is not conserved [20]. This decay mode can be distinguished from the $2\nu\beta\beta$ mode by measuring the energy of the electrons. Without neutrinos to carry away energy in the $0\nu\beta\beta$ mode, the sum of the electron energies will be at the Q-value of the decay. This will be observed as a peak in the electron energy spectrum at the Q-value as illustrated in Figure 1.3.

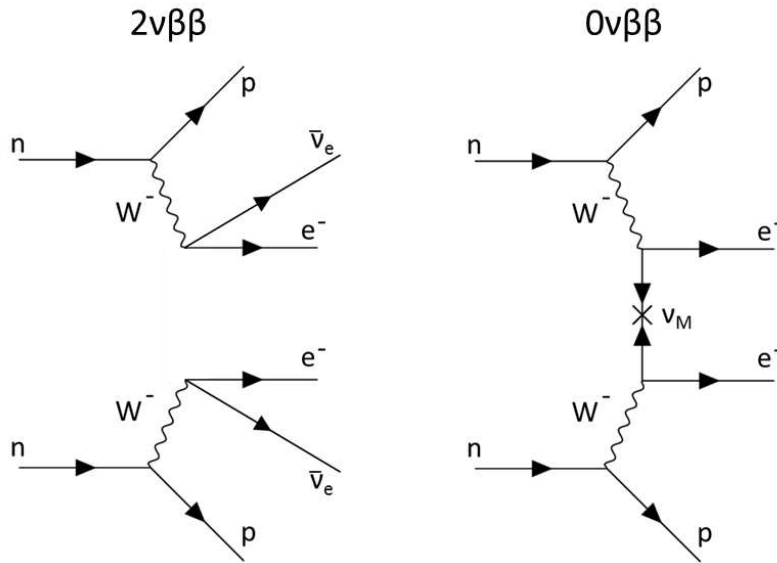


Figure 1.2: Feynman diagrams for the two modes of double beta decay.

Observation of $0\nu\beta\beta$ decay will directly demonstrate that the neutrino is a Majorana particle, and that lepton number is not conserved. The former would be a significant discovery of physics beyond the standard model, and the latter has the potential to provide insight into the matter-antimatter asymmetry of the universe. The discovery of Majorana neutrinos would lend significant experimental validity to the see-saw mechanism [22–25], a “simple” extension of the standard model that explains the relative lightness of the electron, muon and tau neutrinos as compared to

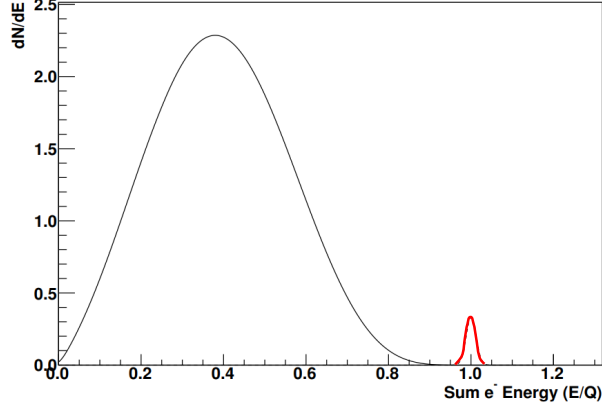


Figure 1.3: The $0\nu\beta\beta$ contribution to the double beta decay spectrum is seen as a peak at the endpoint of the $2\nu\beta\beta$ spectrum. Figure adapted from [21]

their lepton partners. The addition of a right-handed Majorana neutrino state to the standard model would give a mass matrix in which the eigenstates consist of one heavy and one light particle. This gives a somewhat “natural” explanation for the lightness of the observed neutrino masses with minimal extension of the standard model. By explicitly violating lepton number, $0\nu\beta\beta$ is a leptogenic process, which combined with potential CP violation expressed in the PMNS matrix has the basic required ingredients to explain the matter-antimatter asymmetry in the universe [26]. This asymmetry is not currently explained by the processes already discovered in the quark sector, and thus the neutrino sector may be required to shed light on this outstanding mystery.

Observation of the $0\nu\beta\beta$ mode will also provide a measure of the absolute mass scale of the neutrinos. The half-life of this decay is related to the neutrino masses by Eq 1.8 [27].

$$T_{1/2}^{0\nu} = (G^{0\nu}(Q, Z)|M^{0\nu}|^2\langle m_{\beta\beta}\rangle^2)^{-1} \quad (1.8)$$

$T_{1/2}^{0\nu}$ is the half-life of the $0\nu\beta\beta$ decay mode, $G^{0\nu}$ is a known phase space factor and $M^{0\nu}$ is the nuclear matrix element, calculated with several models. $\langle m_{\nu}\rangle$ is the effective Majorana neutrino mass, and is defined as

$$\langle m_{\beta\beta}\rangle = \sum_i U_{ei}^2 m_i. \quad (1.9)$$

In this equation, U_{ei} is the PMNS matrix element evaluated for the mixing of mass state i with the electron flavor state. These elements contain the mixing parameters in Table 1.1, as well as the unknown CP-violating phases. If the possible mass range of $\langle m_{\beta\beta} \rangle$ is plotted against the minimum neutrino mass for both mass hierarchies (Figure 1.4), there is separation of the hierarchies below $\langle m_{\beta\beta} \rangle \approx 0.03$ eV. The area above this is called the Quasi-Degenerate region. In this region, the hierarchies are not well distinguished by a $0\nu\beta\beta$ search. Below this, it is possible for a $0\nu\beta\beta$ search to make a determination of the mass ordering of the neutrinos [15].

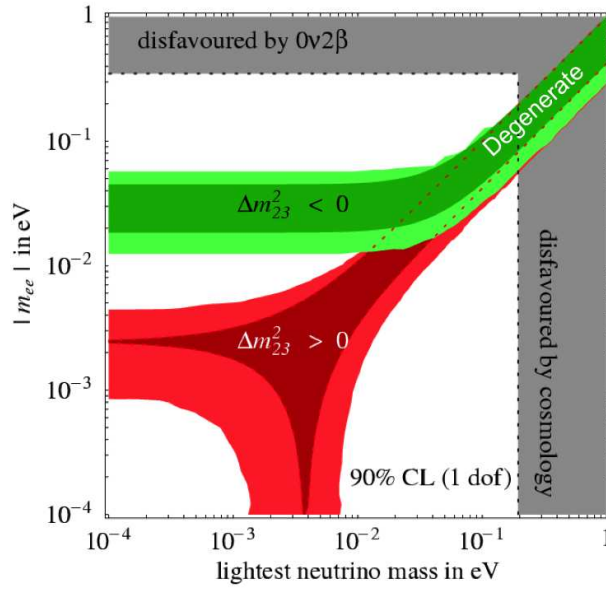


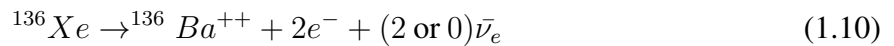
Figure 1.4: Effective neutrino mass (written as $|m_{ee}|$ in this figure) plotted against minimum neutrino mass (m_1 for NH, and m_3 for IH). The current exclusion limits for both cosmological studies and $0\nu\beta\beta$ searches are shown as shaded areas. Figure from [28].

Double beta decay is a very rare process, and requires extremely low background to observe. The $2\nu\beta\beta$ mode has been directly observed for ten isotopes, with half-lives in the range of 10^{18} - 10^{22} years [29]. Strict limits on backgrounds from cosmic and radioactive sources must be achieved to accomplish such observations, as well as the implementation of sophisticated background rejection techniques. The observation of $0\nu\beta\beta$ requires still lower backgrounds, since it is significantly rarer with half-life limits of over 10^{20} - 10^{25} years [30]. In the following section, the search for

$0\nu\beta\beta$ decay in ^{136}Xe by the Enriched Xenon Observatory (EXO) experiment is discussed as well as the potential decay daughter tagging technique being developed.

1.2 Enriched Xenon Observatory

The Enriched Xenon Observatory (EXO) project is a double beta decay experiment using liquid xenon (LXe) time projection chamber (TPC) technology [31]. Xenon-136 is among the even-even nuclei that can undergo double beta decay with a Q-value of 2.457 MeV [32], with the reaction



The single beta decay to ^{136}Cs is energetically forbidden, as shown in Fig. 1.5. Thus the $\beta\beta$ mode will dominate. The following sections will discuss the currently operational EXO-200 detector, as

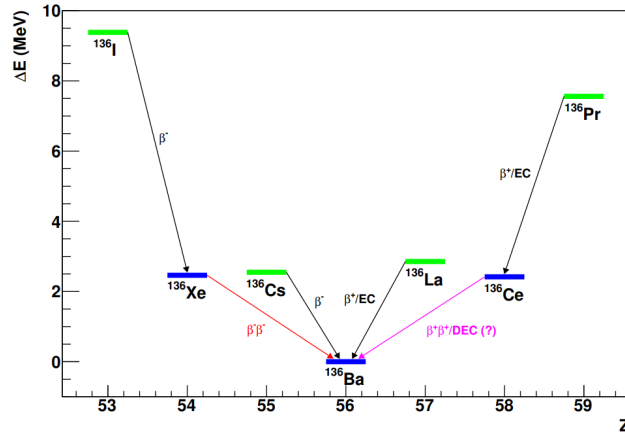


Figure 1.5: The single beta decay mode to ^{136}Cs is energetically forbidden. The double beta decay to ^{136}Ba is then the dominant mode for decay of ^{136}Xe . Figure from [21]

well as the next-generation nEXO detector, currently undergoing research and development. Part of the work in this dissertation involved operation of the EXO-200 detector during its data-taking lifetime.

1.2.1 EXO-200

Detector

The EXO-200 detector uses 200 kg of Xe enriched to 80.6% in the isotope ^{136}Xe to search for $2\nu\beta\beta$ and $0\nu\beta\beta$ decay [31]. Of the 200 kg available, 110 kg are in the active region of the detector where events are recorded. Xenon is unique as a double beta decay candidate since it can be used as both the active element and medium in a liquid or gas-phase TPC, which can be used to search for $\beta\beta$ decays. TPCs measure both light and charge signals from events in the detector, and this can be used to reconstruct the event location in 3D. First, the scintillation light is observed, as it travels at the speed of light in the liquid. Second, the charge produced is drifted via an applied electric field towards a collection grid. This grid consists of two parallel planes of wires, one in front of the other with the wires oriented at 60° to each other. The first plane detects an induction signal as the charge passes it, and is collected on the second plane of wires, as shown schematically Fig. 1.6). The induction wires are biased to ensure transmission to the collection wires. Since the wires form a grid, the 2-D position on the plane where the charge was collected can be determined. To reconstruct the third dimension (called "z" by convention) the time

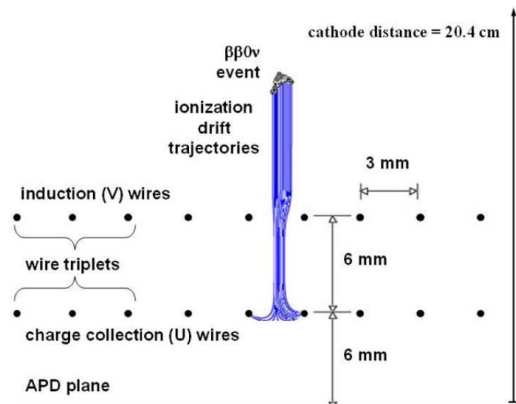


Figure 1.6: Schematic drawing of TPC instrumentation in EXO-200. The uppermost plane of wires represent the induction wires (V-wires for EXO-200), the lower wires represent the collection wires (U-wires for EXO-200). The two planes are shown as colinear for ease of illustration, but the actual wires in the TPC are at a 60° angle to one another. The bottom of the schematic shows the light collection plane (LAAPDs for EXO-200) behind the charge planes.

between the light and charge signal arrivals and the measured drift velocity of charges in the LXe are used. This approach has many advantages. Three dimensional reconstruction of events allows for strong rejection of non $\beta\beta$ -like events. A $\beta\beta$ event will be localized (single site), whereas most backgrounds have interactions in the LXe in multiple locations (multi-site) [19]. Another useful measurement that can be done is the light to charge ratio of the event, which is used to reject α particles created in the TPC. The anti-correlation between these channels is used to improve the resolution of the detector using the "rotated energy", calibrated by a ^{228}Th source as shown in Fig. 1.7. This correlation is caused by fluctuations in the recombination of ionized electrons in the LXe when energy is deposited. These fluctuations lead to proportional fluctuations in light, and anti-correlated fluctuations in charge. It is also helpful in rejecting α decays, as these produce a much higher ratio of scintillation light to charge than $\beta\beta$ events [19].

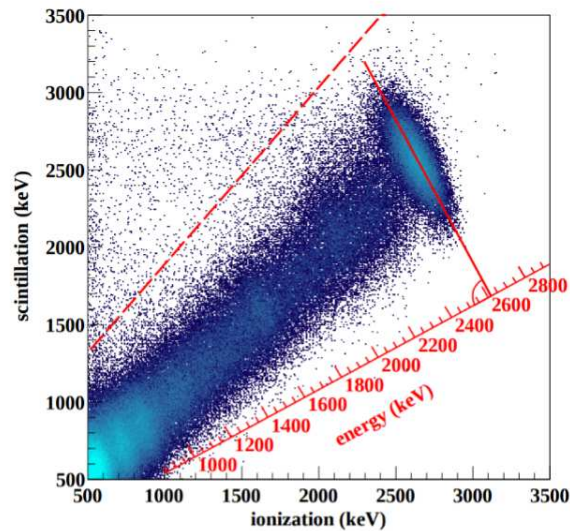


Figure 1.7: The anti-correlation between the scintillation and charge signals produced by a ^{228}Th calibration source. The red axis shows how the "rotated energy" can be used to leverage this effect for better resolution. The large ellipse is near the Q-value and the shape of this known energy deposit is used to define the optimal rotation for the energy scale.

The EXO-200 detector is described in detail in [31]. It utilizes a cylindrical cryostat instrumented with two TPCs sharing a common cathode in the center, and identical collection planes at

the endcaps. Each TPC is 22 cm long, with a drift length of 19.2 cm (the z direction), and 40 cm in diameter arranged as shown in Figure 1.8. The drift field is applied with a -12 kV (recently

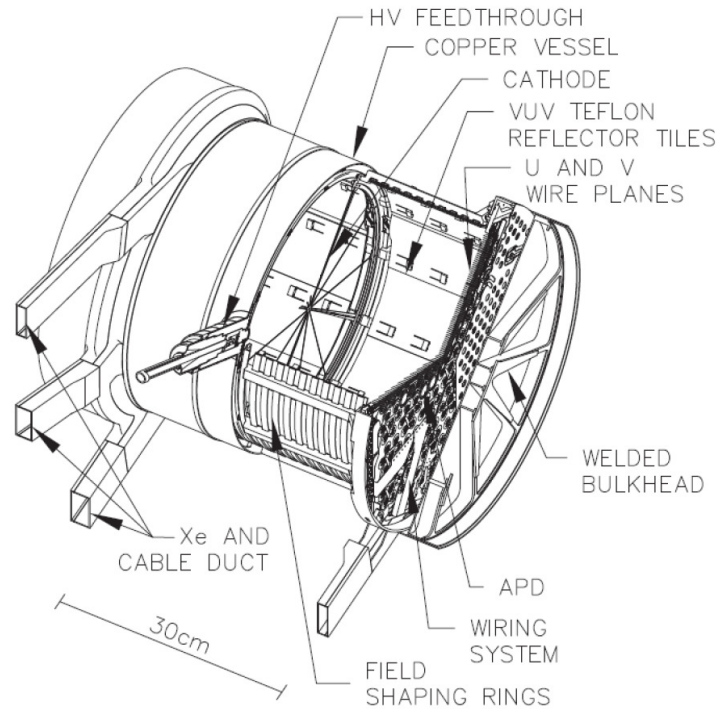


Figure 1.8: Cut-away drawing of the EXO-200 detector. One of the TPC’s is shown with the cathode in the middle, and the charge and light instrumentation on the endcap.

increased from -8kV [20]) bias on the central cathode, and field shaping rings are used to ensure a uniform and axial field. This gives the TPC a drift field of 567 V/cm, in which electrons drift at 1.85 mm/s [33]. The light is collected by an array of large area avalanche photodiodes (LAAPDs). The LAAPDs are held in holes behind the charge collection planes as seen in Figure 1.9. The LXe is held at a temperature of 167 K by a surrounding bath of HFE-7000 cryogenic fluid. The TPC vessel is made of ultra-pure copper, and a cylinder of Teflon was inserted inside the field shaping rings along the outside of the TPC active volume to increase the reflectivity, and thus the light collected by the LAAPDs. The xenon is continuously recirculated via an ultra-clean magnetically coupled pump [34] and purified, with 175 kg of the 200 kg available being inside the detector at any given time.



Figure 1.9: This picture shows the holes into which the LAAPDs were be mounted. The wire planes are already installed in front of the holes. The top of the cylinder is the cathode plane, though the cathode was not yet installed.

All of the detector and support hardware are housed in a class 1000 cleanroom located at the Waste Isolation Pilot Plant (WIPP) near Carlsbad, New Mexico. This facility for the disposal of low-radioactivity nuclear waste is 660 m (1585 meters water equivalent) underground. It is a particularly attractive site for low-background experiments, since the salt bed in which it is located has much lower levels of U and Th than most hard-rock mines. In addition to the overburden shielding from cosmic radiation, two layers of lead shielding are placed around the cryostat. Scintillating muon veto panels are mounted on the exterior of the cleanrooms to allow for an active rejection of cosmic backgrounds. The layout of the cryostat and shielding is shown in Figure 1.10. To further reduce backgrounds, all materials used in the detector are thoroughly measured for trace radioactive impurities, such as U and Th [35], and the cleanest materials available are used in the detector. To minimize the background from radon in the air, the area around the cryostat has been sealed, and a supply of air that has been scrubbed for Rn by a “deradonator” is continuously pumped in [36].

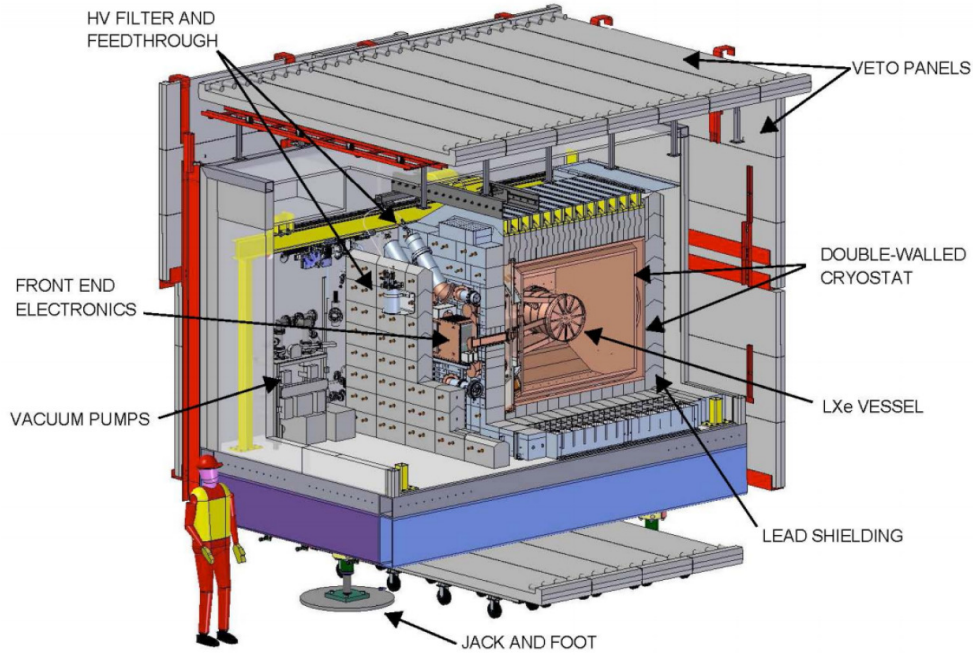


Figure 1.10: Schematic diagram of the EXO-200 detector installed in the cleanroom. The Detector has many layers of shielding. The innermost is the HFE-7000 used as a cryogenic fluid. Outside of the cryostat is a lead shield, and another lead wall. Outside the lead shield is an airgap flushed with radon-scrubbed air. Outside of the cleanroom are scintillating muon veto panels for active veto.

Results

The half-life of the $2\nu\beta\beta$ decay mode of ^{136}Xe has been measured in EXO-200. Using data taken between Sept 2011 and April 2012, corresponding to 23.14 kg-yr exposure of ^{136}Xe , the half-life was measured to be

$$T_{1/2}^{2\nu\beta\beta} = 2.165 \pm 0.016(\text{stat}) \pm 0.059(\text{sys}) \times 10^{21} \text{years}. \quad (1.11)$$

This is the longest-lived decay yet directly detected. The energy spectrum is shown in Figure 1.11, with the $2\nu\beta\beta$ contribution shown as the gray filled area. A resolution of $1.84 \pm 0.03\% \sigma/E$ at the Q-value was achieved for this dataset. This is the most precise measurement of a $2\nu\beta\beta$ decay to date.

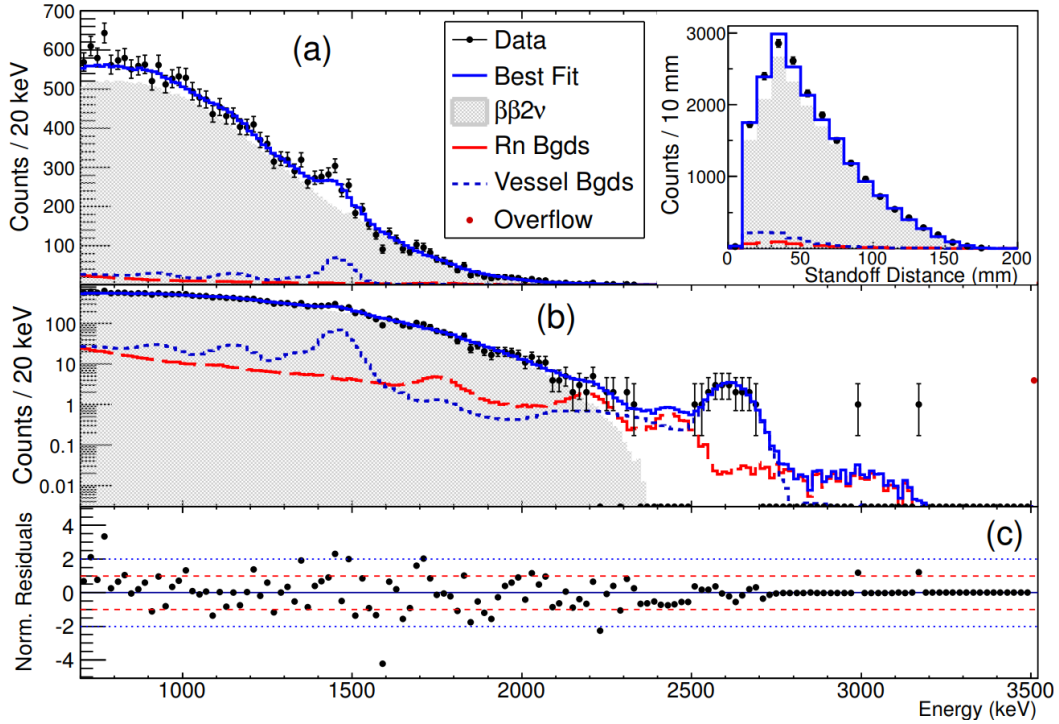


Figure 1.11: The measured energy spectrum from the EXO-200 detector with best fit. It is shown in linear (a), log (b), and with its residuals (c). The $2\nu\beta\beta$ contribution is shown in gray [37].

EXO-200 has also set a competitive limit for $0\nu\beta\beta$ decay. Using data spanning from Sept 2011 to April 2017, 868.5 days of livetime were accumulated, following data quality cuts. This is split into Phases I and II, with Phase II constituting the data taken after the electronics and cathode voltage upgrades installed in May 2016. The total exposure for this limit is 177.6 kg·yr, of which 55.6 kg·yr was from Phase II. The energy spectrum, with a zoom-in on the endpoint for the $0\nu\beta\beta$ contribution is shown in Figure 1.12. Having no statistically significant contribution from $0\nu\beta\beta$ decay, a half-life limit of

$$T_{1/2}^{0\nu\beta\beta} > 1.8 \times 10^{25} \text{ yr} \quad (1.12)$$

has been set [14]. The 90% confidence level sensitivity was 3.7×10^{25} yr, and the resolution was improved to $\sigma/E = 1.23\%$ at the Q-value of 2.457 MeV. EXO-200 has recently stopped taking data. It is expected that the sensitivity will be improved upon with the additional data.

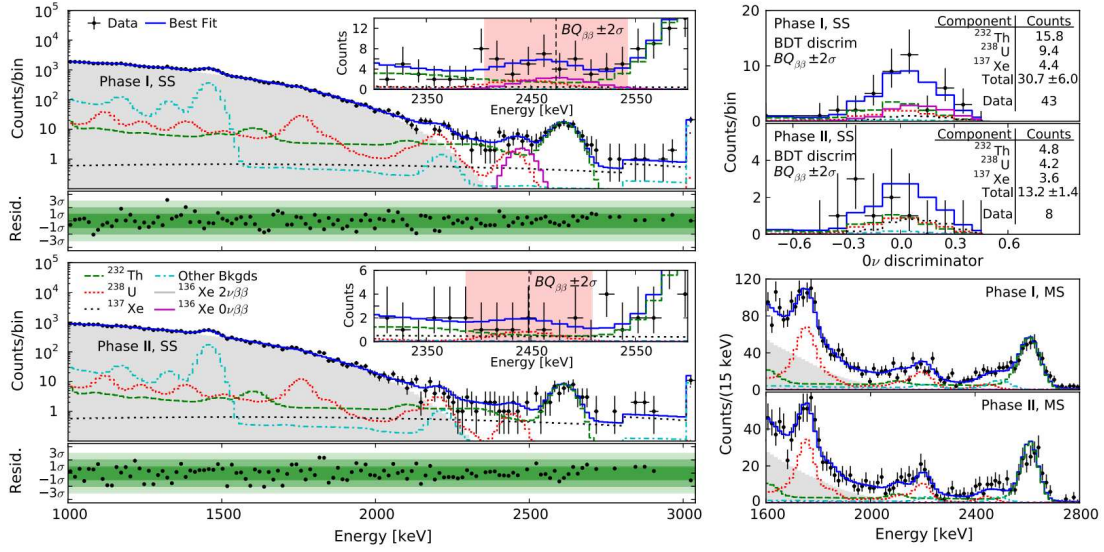


Figure 1.12: The measured energy spectrum for Phase I (upper left) and Phase II (lower left), with best fit and backgrounds. The region around the Q-value is shown in the upper right, with the background fit levels in the ROI. The data are consistent with no $0\nu\beta\beta$ events, thus a limit has been reported [14].

1.2.2 nEXO

Building on the success of the EXO-200 experiment, the nEXO detector is a proposed next-generation 5 tonne LXe TPC currently being developed for a more sensitive $0\nu\beta\beta$ decay search. It is described in detail in [38]. One possible location for the nEXO detector is the cryopit at SNO-LAB, located at the 6800' level (6010 m.w.e. overburden [39]) of the INCO Ltd. Creighton Mine near Sudbury, Ontario. The target sensitivity at the 90% confidence limit for nEXO is $T_{1/2}^{0\nu\beta\beta} > 9.2 \times 10^{27}$ yr, which corresponds to an effective neutrino mass limit of approximately 10 meV, depending on the nuclear model used [15]. To achieve the more than two order of magnitude increase in sensitivity compared to EXO-200, the nEXO detector has been designed using the proven concepts from EXO-200, while incorporating new technologies that have since been developed. The leading contribution is the $25\times$ increase in mass, however significant improvements in instrumentation and self-shielding will maximize the discovery potential of nEXO.

The nEXO design consists of a single, cylindrical TPC with a drift length of 125 cm and diameter of 115 cm, with the cathode and charge collection at either endcap. By constructing a monolithic TPC, the fiducial volume of LXe at the center will be better self-shielded from both

backgrounds coming from outside the vessel, as well as the materials of the vessel itself. In particular, the choice for a single drift volume (a departure from EXO-200) allows the inner Xe to be better shielded from gamma rays originating from impurities at the cathode, most relevantly ^{214}Bi , a daughter of ^{222}Rn . The design for the cathode is a $\sim 125\ \mu\text{m}$ thick sheet of copper (as opposed to the mesh used in EXO-200), coated with aluminum for reflectivity in the VUV (where the scintillation light is), and protected from oxidation by a Mg_2F coating. The drift field will be similar to EXO-200 at $\sim 400\ \text{V/cm}$, and thus the voltage on the cathode will need to be increased to $\sim -50\ \text{kV}$ with the longer drift length. As in EXO-200, the vessel will be constructed of low-radioactivity copper, with field shaping rings along the drift length to maximize the uniformity of the drift field. The design of the instrumentation and vessel have been done with the intention to reduce plastic components as much as possible, to avoid outgassing negatively affecting Xe purity. The large volume to surface area ratio also aids in reducing the effect of impurities outgassing from the surfaces.

The instrumentation for nEXO has been significantly modified from EXO-200 given the much larger volume to be instrumented, as well as the rapid development of technologies in the TPC sector. Fused silica tiles metalized with interleaved pads forming a grid pattern will be used for charge collection instead of wires, which are challenging to tension especially given the length required. These tiles will be approximately $10\times 10\ \text{cm}$, with the grid spacing of the pads being nominally 3 mm. nEXO will use silicon photomultipliers (SiPMs) on the inside of the barrel walls of the TPC for light collection, instead of LAAPD's mounted behind the charge collection plane, since neither the cathode nor charge tiles are opaque. This geometry has several advantages. The area covered by the SiPMs is greater than that of the LAAPDs in EXO-200, and VUV-reflective teflon is no longer required to line the TPC given the increase in light collection coverage. In addition to this, VUV reflective coatings will be applied to passive TPC components to maximize scintillation light collection efficiency. The charge and light collection can be seen in the cut-away drawing in Fig. 1.13. These improvements on the EXO-200 instrumentation provide a base design to achieve the sensitivity projected for nEXO.

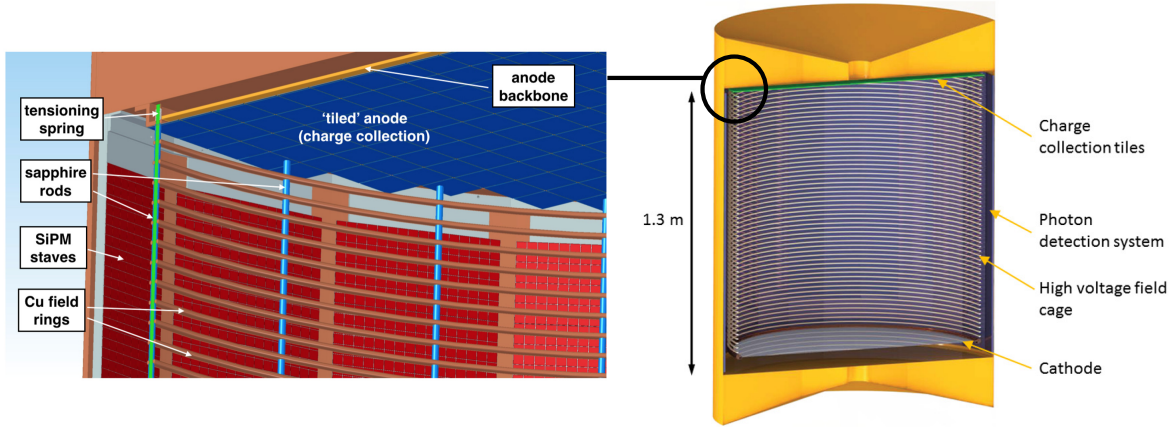


Figure 1.13: The basic layout of the nEXO detector is shown. The instrumentation is shown schematically, without the feedthroughs for high voltage, Xe recirculation or readout. The close-up view of the anode of the nEXO TPC shows the charge detection tiles and the SiPMs are shown in more detail as well as the field shaping rings with sapphire supports and spacers [38].

The exterior design of the nEXO TPC into a cryostat in the cryopit at SNOLAB provides multiple layers of shielding. The cryostat is comprised of two nested spherical vessels made of carbon composite, separated by vacuum insulation, shown schematically in Fig. 1.14. The inner vessel will contain the HFE-7000 coolant, the same as used for EXO-200. The outer vessel will be held at vacuum to insulate the inner cryostat. The large thermal mass of the cryogenic system means that the system is stable, and a loss of cooling will not be catastrophic. The outer vessel will be supported from above in a water bath in the cryopit itself. The water shield attenuates cosmic rays and radioactivity from the rock walls, and is instrumented with photomultiplier tubes (PMTs) to provide an active muon veto using the Cherenkov light from the muons traversing the water.

The second layer of shielding is the HFE-7000, and the final layer of shielding is the LXe itself. Using the detailed background model developed in [15], the half life sensitivity as a function of operation time is shown in Fig. 1.15 (a), with an expected sensitivity of $T_{1/2}^{0\nu\beta\beta} > 9.2 \times 10^{27}$ yr. Converting to effective neutrino mass this limit corresponds to $\langle m_{\beta\beta} \rangle < (5.7-17.7)$ meV depending on the nuclear matrix element used. This allows for complete coverage of the inverted mass hierarchy after 10 years, as shown in Fig. 1.15 (b).

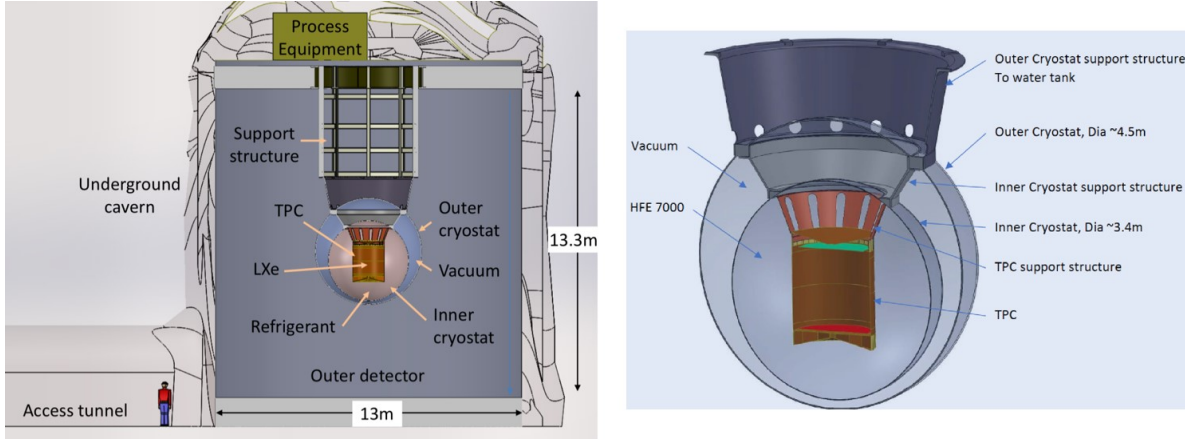


Figure 1.14: The nEXO detector in the SNOLAB cryopit, showing the TPC, cryostat, water shield and support structure, as described in [38].

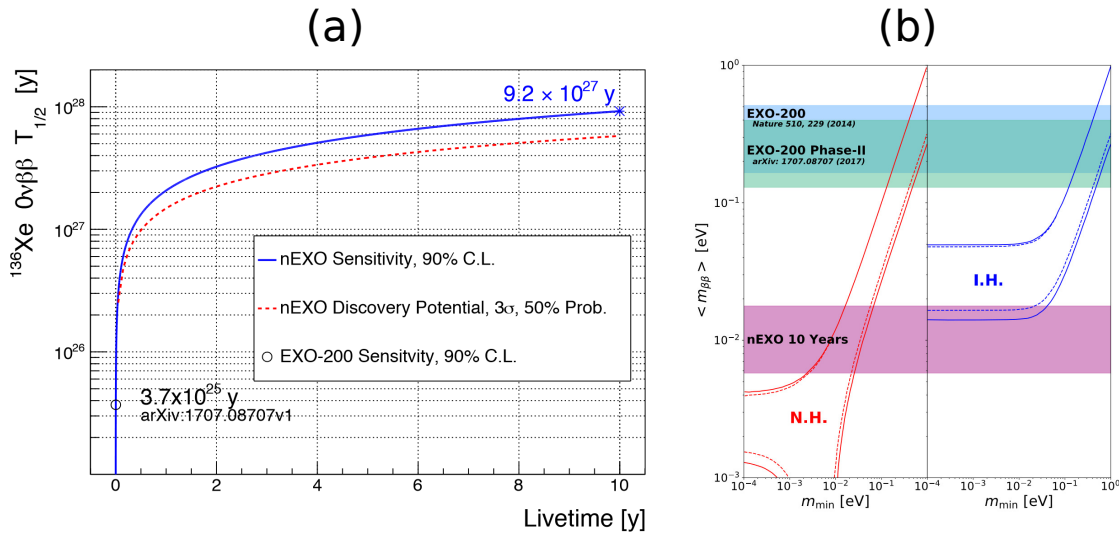


Figure 1.15: Simulated nEXO sensitivity curve, plotted out to ten years of operation, (a). The sensitivity reaches $T_{1/2}^{0\nu\beta\beta} > 9.2 \times 10^{27}$ yr. The effective neutrino mass sensitivity after ten years of operation, (b), reaches $\langle m_{\nu} \rangle \sim 10^{-2}$ eV. This provides coverage of the inverted Hierarchy (IH), and approaches the flat portion of the normal hierarchy (NH). Figures from [15].

1.3 Barium Tagging

The limiting factor for the sensitivity of nEXO is the small background in the region of interest (ROI) from radioactive sources. A powerful way to reject backgrounds for $0\nu\beta\beta$ decay is to identify the Ba daughter ion [40]. A positive identification or "tag" of this daughter will provide discrimination against for all non- $\beta\beta$ events, such as the ^{232}Th , ^{238}U and ^{134}Xe gamma rays in the ROI from the EXO-200 data. The only remaining background will be the $2\nu\beta\beta$ mode, which is

very small at the endpoint (Q-value) of the energy spectrum, and ultimately limits the resolution after 10 yr. The 3-D reconstruction capability of a LXE TPC such as nEXO offers a unique opportunity to implement a Ba tagging scheme. Since the location of any potential $0\nu\beta\beta$ is known, a probe could be sent to that location to extract and tag the barium daughter.

Several tagging schemes are being considered by the nEXO collaboration. A technique by which the barium daughter is extracted on a conducting probe and then desorbed via infrared laser light, followed by resonance ionization and time-of flight spectroscopy has been investigated at Stanford University. It is described in [41] with some preliminary results. Another approach is to extract the Ba^+ ion via a capillary from LXe to gaseous Xe and use an RF-funnel system to transport the barium ion while the neutral xenon is pumped away. The ion would then be trapped in an ion trap and tagged by laser fluorescence and mass spectroscopy. This is being pursued at Carleton and McGill Universities as well as at TRIUMF [42].

1.3.1 Ba Fluorescence Tagging in Solid Xenon at CSU

An alternative technique being developed at Colorado State University, the Ba daughter would be extracted in solid Xe (SXe) and tagged via laser fluorescence imaging in the SXe layer. To implement this in the nEXO detector, a cryogenic probe would be deployed to the decay site. A small amount of LXe would be frozen onto the probe, trapping the decay daughter in the SXe layer, a conceptual drawing of the extraction probe is shown in Fig. 1.16. The probe would then be extracted and further cooled to low temperature (~ 10 K) in a separate chamber to improve the fluorescence efficiency of the Ba daughter. It is suspected that the Ba^{++} daughter of $\beta\beta$ decay will charge exchange quickly with Xe and become Ba^+ , since the LXe band gap is slightly less than the ionization potential for Ba^+ [40]. Observation of single beta decay of Rn in the EXO-200 detector shows that 76% of the Po^+ daughters remain as ions, indicating some Ba^+ ions may neutralize via recombination. There is also a possibility that the Ba^+ ion will neutralize during the freezing process prior to extraction [43]. Thus, the ability to extract, image and count both Ba^+ ions and Ba atoms is desirable for the tagging technique.

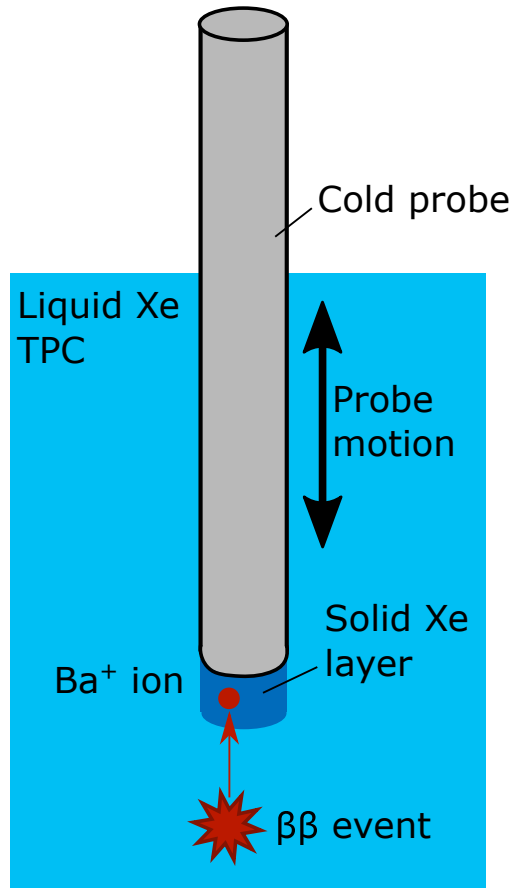


Figure 1.16: Concept drawing of dipping a cryogenic probe into LXe TPC to extract Ba daughter.

A drawing of a potential cryogenic tagging probe design using cryogenic helium to cool the tip is shown in Figure 1.17. A small copper mount is attached to the end of the probe, and holds a sapphire window upon which a SXe layer is grown, trapping the Ba daughter. A heater would be used to control the growth rate and thickness of the SXe layer. After the probe has been extracted to an isolated chamber for observation, the probe would be further cooled to < 50 K for fluorescence tagging. The pressure in the chamber would be maintained at the SXe vapor pressure as the probe is cooled to prevent any net evaporation of the SXe layer or further freezing of Xe onto the probe which may degrade the optical quality of the SXe. A prototype probe and extraction system is currently being developed at CSU in parallel with this work. A laser would then be sent into the observation cell to excite the Ba fluorescence, which would be collected to provide the Ba tag. The goal of the fluorescence tagging technique is to count the Ba or Ba⁺ daughters in the SXe.

A count of 1 would indicate a $\beta\beta$ event, and a count of 0 would indicate a background event. The fluorescence may be imaged through an optical filter, or analyzed by a spectrometer. The development and demonstration of the optical component of this Ba tagging method, i.e. imaging single Ba atoms deposited from an ion beam source into SXe on a window, is the focus of this work.

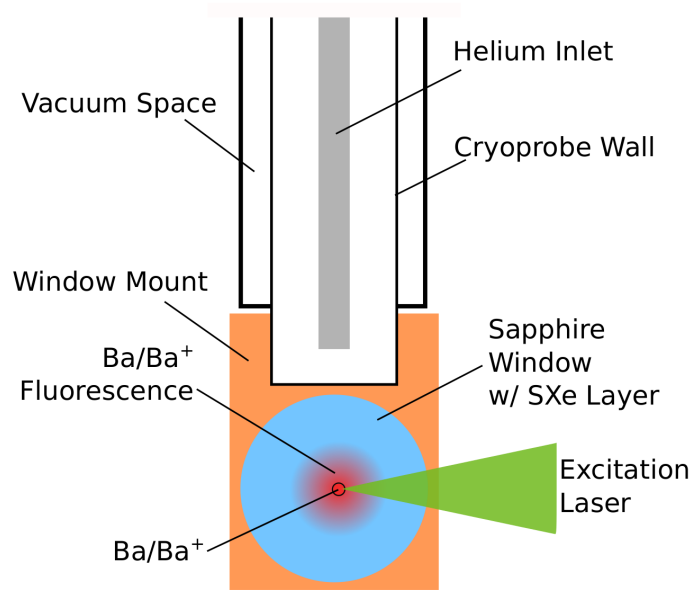


Figure 1.17: A potential SXe tagging probe concept is shown. The barium ion/atom is held in the SXe matrix frozen on the sapphire window. The excitation and collection of the Ba fluorescence is done through windows in an observation cube.

The sensitivity of nEXO could increase by up to a factor of 4 if a $2\nu\beta\beta$ -only background is achieved. As shown in Figure 1.18, in addition to the improved sensitivity, the positive tag of the decay daughter combined with well reconstructed energy and topology of the event will provide very strong, complimentary evidence that the observed event is in fact $0\nu\beta\beta$ decay.

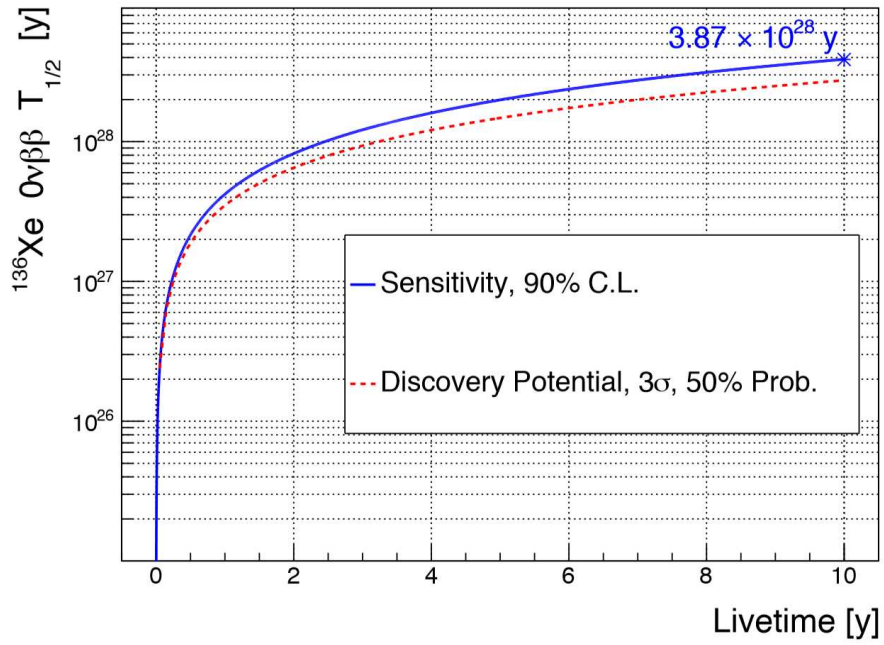


Figure 1.18: Simulated nEXO sensitivity curve, plotted out to ten years of operation with Ba-tagging implemented ($2\nu\beta\beta$ -only background model). The sensitivity reaches $T_{1/2}^{0\nu\beta\beta} > 3.87 \times 10^{28}$ years, an increase of a factor of ~ 4 over the non-Ba-tagging case [15].

Chapter 2

Theory

Successful barium tagging in solid xenon (SXe) relies on fluorescence spectroscopy of Ba/Ba⁺ isolated in a Xe matrix. This work focuses on the imaging of Ba atoms in a specific Xe matrix site. The electronic structure and transition energies of Ba atoms are discussed in Sec. 2.1. Interactions with the xenon matrix cause modifications to the absorption and emission spectra of Ba. This and the assignment of emission lines of Ba in SXe to specific matrix sites are discussed in Sec. 2.2. The method used to calculate the fluorescence efficiency and absorption cross-section from a measured excitation spectrum is outlined in Sec. 2.3. The final section, Sec. 2.4, a model is presented to simulate the signal expected from the Ba atoms using the technique developed in this work.

2.1 Barium Spectroscopy

The lowest lying vacuum energy levels of Ba and the transitions between them are shown in Fig. 2.1 [44–46]. The transitions of interest for this work are shown with their vacuum wavelengths and decay rates in Table 2.1. The detection of single Ba atoms requires many cycles of a recycling transition for a significant signal to be detected. Any process by which the fluorescence signal is terminated is a potential challenge for the high sensitivities required for practical Ba tagging.

2.1.1 Ba Transitions in Vacuum

The fluorescence transition used in this work is $6s6p\ ^1P_1 \leftrightarrow 6s^2\ ^1S_0$, with a vacuum wavelength of 553.5 nm. The decay from the $6s6p\ ^1P_1$ state to the $6s^2\ ^1S_0$ state is the dominant decay path, but the decays to the $6s5d$ states also occur. Comparing the decay rates shown in Table 2.1 [47], it is expected in vacuum that for every 330 decays to the $6s^2$ state, the $6s6p$ state will decay once to one of the $6s5d$ states. These states are metastable (decay rates < order $1\ \text{s}^{-1}$), as the decay to the $6s^2$ state is electric-dipole forbidden, with $\Delta l = 2$. Since these states can take a significant fraction of a second or more to decay, this would limit the number of photons that could be collected in

Table 2.1: Wavelengths and decay rates for the principle transitions of Ba atoms in vacuum of interest to this work. The transition wavelengths and decay rates are taken from NIST tables [44], unless otherwise noted.

Transition	Vacuum Wavelength (nm)	Decay Rate (s ⁻¹)
$6s6p\ ^1P_1 \leftrightarrow 6s^2\ ^1S_0$	553.5	1.19×10^8
$6s6p\ ^1P_1 \leftrightarrow 6s5d\ ^1D_2$	1500.0	2.5×10^5
$6s6p\ ^1P_1 \leftrightarrow 6s5d\ ^3D_2$	1130.0	1.1×10^5
$6s6p\ ^1P_1 \leftrightarrow 6s5d\ ^3D_1$	1107.6	3.1×10^3
$6s6p\ ^3P_2 \leftrightarrow 6s5d\ ^3D_3$	2552.2	$5.57 \times 10^5\ ^a$
$6s6p\ ^3P_2 \leftrightarrow 6s5d\ ^3D_2$	2326.0	$1.28 \times 10^5\ ^a$
$6s6p\ ^3P_2 \leftrightarrow 6s5d\ ^3D_1$	2231.8	$1.00 \times 10^4\ ^a$
$6s6p\ ^3P_2 \leftrightarrow 6s5d\ ^1D_2$	4718.3	$4.48 \times 10^2\ ^a$
$6s6p\ ^3P_1 \leftrightarrow 6s5d\ ^3D_1$	2775.7	$1.27 \times 10^5\ ^a$
$6s6p\ ^3P_1 \leftrightarrow 6s5d\ ^3D_2$	2923.0	$3.15 \times 10^5\ ^a$
$6s6p\ ^3P_1 \leftrightarrow 6s5d\ ^1D_2$	8056.2	$3.26 \times 10^2\ ^a$
$6s6p\ ^3P_0 \leftrightarrow 6s5d\ ^3D_1$	3094.0	$3.50 \times 10^5\ ^a$
$6s6p\ ^3P_1 \leftrightarrow 6s^2\ ^1S_0$	791.1	2.98×10^5
$6s5d\ ^1D_2 \leftrightarrow 6s^2\ ^1S_0$	877.6	$4\ ^b$
$6s5d\ ^3D_2 \leftrightarrow 6s^2\ ^1S_0$	1085.1	$1.45 \times 10^{-2}\ ^a$
$6s5d\ ^3D_1 \leftrightarrow 6s^2\ ^1S_0$	1106.9	unknown

^aReference [45]

^bReference [46]

a reasonable interrogation time. However, by using additional lasers tuned to 1107 nm, 1130 nm and 1550 nm, the $6s6p$ state could be re-populated from the $6s5d$ states. By re-pumping these IR transitions as well as two red transitions from the $6s5d\ ^3D_{1,2}$ states to the $5d6p\ ^3D_1$ state, single Ba atoms have been trapped and imaged in a magneto-optical trap [48]. For the specific matrix site investigated here, it was found that this optical pumping effect is less severe than expected for a Ba atom in vacuum. That is, more cycles of the recycling transition occur before the fluorescence signal is reduced significantly [49]. Possible explanations for this are discussed in Sec. 2.2.3 after considering the interactions of the Ba atom with the SXe matrix.

2.2 Matrix Isolation Spectroscopy

Matrix isolation spectroscopy is a technique that uses a noble gas host species to isolate potentially reactive guest atoms, such that they can be studied with minimal perturbations [50]. Since the

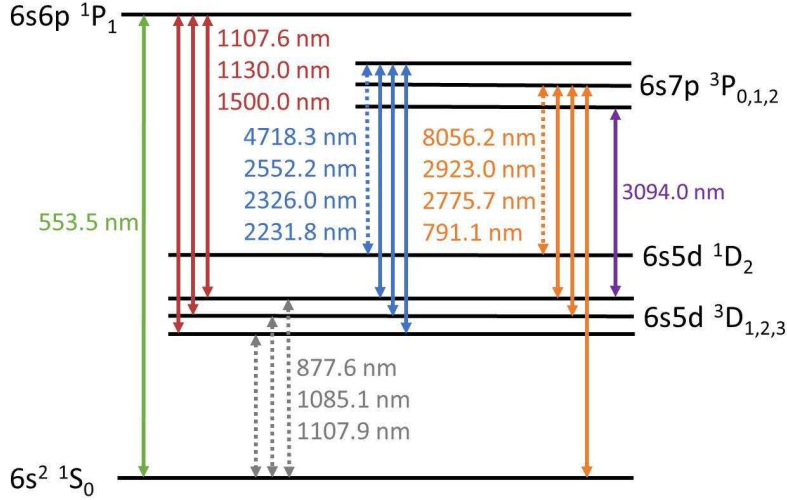


Figure 2.1: Energy Level diagram for Ba atoms in vacuum. The recycling transition used in this work is $6s6p\ ^1P_1 \leftrightarrow 6s^2\ ^1S_0$.

Ba is being produced in LXe by double beta decay, it is already isolated in a liquid noble element. To utilize matrix isolation spectroscopy, the sample must be cooled and kept at cryogenic temperature to isolate the Ba in solid phase xenon. These conditions can be achieved by extracting the single Ba atom from the high purity Xe in the TPC with a cryogenic probe, and then imaging the Ba atom by observing its laser induced fluorescence in the SXe sample, as discussed in Sec. 1.3. The advantage of matrix isolation for the proposed Ba tagging technique is the ability to isolate the Ba atom for as long as is required, allowing sensitive imaging to be done.

2.2.1 Shifts of Transitions in SXe Matrix

The potential created by the Xe atoms surrounding a Ba atom causes a perturbation to the vacuum energy levels described in Sec. 2.1. The full Xe matrix potential may be modeled using the diatomics-in-molecule (DIM) method [51], that utilizes the Xe_2 and BaXe diatomic molecular potentials. At long range, the Van der Waals component exhibiting r^{-6} behavior dominates, consistent with an induced dipole-dipole interaction described by London dispersion [52]. A pseudopotential derived from the overlapping of wavefunctions represents the repulsive effect of the Pauli exclusion principle at short range [53, 54]. These diatomic potentials have been modeled using an array of methods from Lennard-Jones-like potentials [55, 56] to Coupled-Cluster quantum

chemistry simulations [57–59]. Once the diatomic Hamiltonians are determined, the total Hamiltonian of the system (Xe matrix with embedded Ba atom) can be expressed in terms of the atomic and diatomic fragment potentials. The Hamiltonian matrix elements are calculated over a chosen basis set of wavefunctions for the Ba atom. By enlarging the basis set of wavefunctions, this method approaches the exact Born-Oppenheimer energy of the molecule [60]. The DIM method has been effectively used previously to study other alkali-earth/noble element systems [61, 62].

The thermal energy of the atoms in the matrix leads to vibrational motion, which is quantized into modes as in the quantum harmonic oscillator, though the potential is in general anharmonic [63]. These modes are represented as vibrational states within the more widely spaced electronic states, drawn schematically in Fig. 2.2. An electronic transition occurs nearly instantaneously relative to the vibrational motion of the nuclei of the atoms. Thus, an electronic transition is treated as a vertical line in the energy diagram (Fig. 2.2). The Franck-Condon Principle [64, 65] states that the excitation will be strongest where the vibrational wavefunctions of the ground and excited states overlap. The probability of a particular transition occurring is proportional to the square of the overlap integral of the vibrational states, called the Franck-Condon factor.

$$P_{i \rightarrow f} \propto |\langle \psi_{\nu',f}^* | \psi_{\nu',i} \rangle|^2 = \left| \int \psi_{\nu',f}^* \psi_{\nu',i} dq \right|^2 \quad (2.1)$$

In this equation, $\psi_{\nu',i}$ and $\psi_{\nu',f}$ are the initial and final vibrational states, and the integration is done over q , the coordinate of motion along the potential surface. This leads to broadening of the absorption spectrum, as these excitations can occur to many vibrational states with varying Franck-Condon factors. Furthermore, as indicated by the green arrow in Fig. 2.2, the peak wavelength of this excitation is not only determined by the binding energy difference of the two electronic states, but by the energies of the vibrational modes excited as well. Thus, the peak excitation wavelength of a transition is blue shifted from the transition between the two $\nu = 0$ states, called the zero phonon line. When the electron is excited, it will quickly and non-radiatively decay to a low vibrational state of the excited electronic state by phonon interactions with the surrounding matrix. The most probable decay may occur to excited vibrational levels of the ground state (Fig. 2.2). The

emission is thus red-shifted compared to the zero phonon line and the absorption, as indicated by the shorter emission arrow (red) in Fig. 2.2. The absorption spectrum can be further complicated by triplet structures introduced via Jahn-Teller distortion [66]. This effect causes a three-fold splitting of the absorption by removing the spatial degeneracy of the excited P state of the atom via geometrical distortion of the crystal structure. The shifting and broadening of the $6s6p\ ^1P_1 \leftrightarrow 6s^2\ ^1S_0$ transition in the Ba-Xe system has been studied experimentally and theoretically [43, 58, 67]. The results of these studies are summarized in the following section.

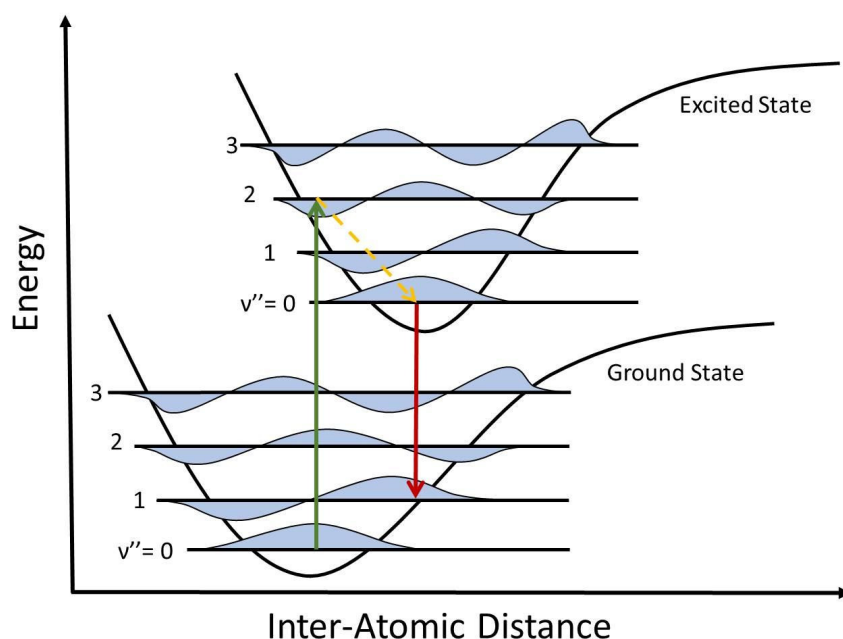


Figure 2.2: Schematic diagram of emission red shift relative to absorption. Vibrational modes introduced by the host matrix are shown as levels within the ground and excited electronic states, with the vibrational wavefunction represented by the blue-filled curves.

2.2.2 Barium Guest Atom Sites in Xenon

The perturbation of transition energies of the guest Ba atoms depends on the configuration of Xe atoms surrounding the Ba impurity. That is to say, the geometry of the Xe vacancy filled by the Ba atom is important to both the absorption and emission spectra of the Ba atom to be tagged. Work done by this group [43] and the McCaffery group [58, 67] have identified several emission

lines of Ba in SXe. The most prominent are shown in Figure 2.3. The excitation spectra for the six lines identified as Ba in SXe shown in Figure 2.4 are distinct in shape and position. Thus each emission line corresponds to a different geometry of trapping site in the SXe matrix.

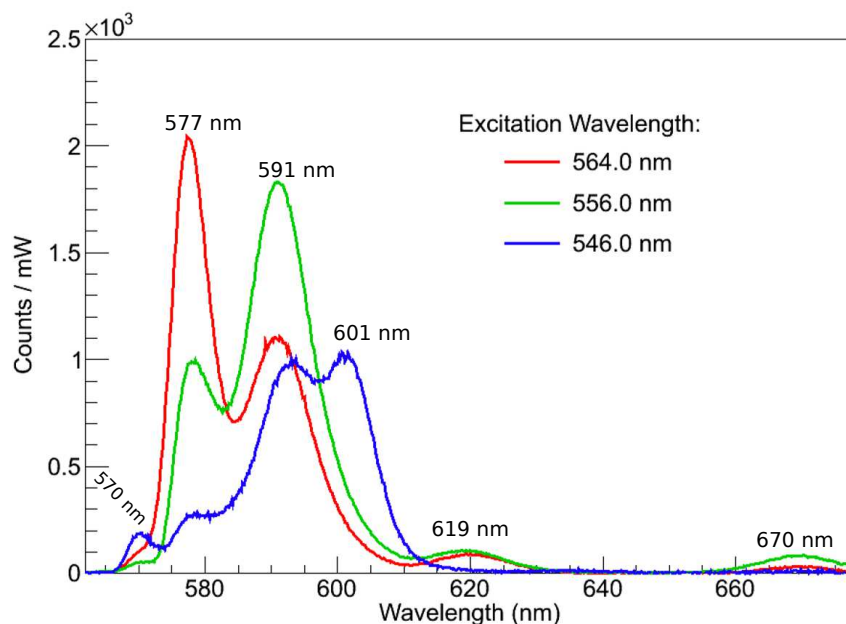


Figure 2.3: Emission spectrum of Ba in SXe excited with a laser at three different wavelengths. The emission lines at 570 nm, 577 nm, 591 nm, 601 nm, 619 nm and 670 nm are labeled. Figure from Ref. [49].

Assignment of specific matrix sites in SXe to the strongest emission peaks at 577 nm and 591 nm has been done by Davis, Gervais and McCaffrey [67]. The excitation spectra in Fig. 2.4 of the two emission lines can be used to deduce the vacancy site corresponding to the emission. The 591 nm line shows symmetric three-fold Jahn-Teller splitting, a common feature of $S \rightarrow P$ transitions in noble gas matrices with highly symmetric trapping sites [68]. The 577 nm line exhibits an asymmetric $(2+1)$ splitting, with two low wavelength peaks, and one high wavelength peak, which could be explained by a trapping site with one long axis, where the electron cloud is less confined.

To match these spectral features to trapping sites, the crystal structure of Xe must be considered. Xe forms a face-centered cubic lattice (*fcc*) [69] with nearest neighbor distance of 4.33 \AA in the absence of impurities, while the inter-nuclear distance of the BaXe dimer was calculated

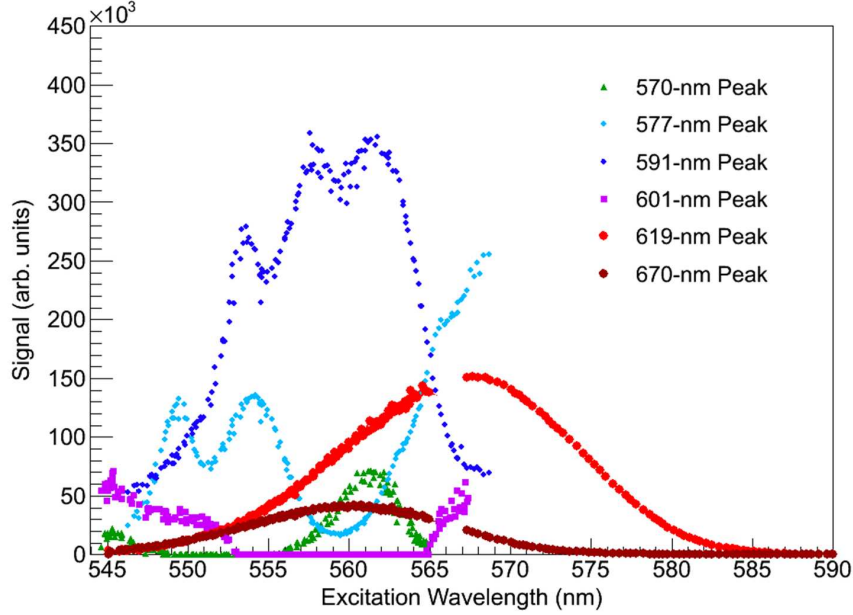


Figure 2.4: Excitation spectra for the lines identified in Fig. 2.3. Figure from Ref. [49].

to be 5.55 \AA via coupled-cluster simulations [58]. Due to this difference in bond length, a Ba atom does not fit well in a single, double or triple vacancy site. Several larger vacancy sites have been investigated, and the nearest neighbor distances are shown relative to the Ba-Xe interaction potential in Figure 2.5. A 4-vacancy, tetrahedrally symmetric (TV- T_d) site, where a tetrahedron of Xe atoms are removed along the (111) axis of the crystal is more favorable (shown in Fig. 2.6). This site has a nearest neighbor distance of 5.08 \AA , which is more similar to the preferred diatomic Ba-Xe bond length. A 6-vacancy octahedrally symmetric (HV- O_h) site, formed by removing the 6 Xe atoms surrounding the center of the unit cell has a nearest neighbor distance of 5.35 \AA . This site might be a better match for Ba than the TV- T_d site, but the removal of additional Xe atoms lowers the cohesion energy of the crystal, and could make the HV- O_h site overall less energetically favorable. The largest vacancy site considered was the 13-vacancy CO site where an entire unit cell is removed. This site has a nearest-neighbor distance of 6.2 \AA which accommodates the Ba atom, but lowers the cohesion energy of the crystal even more than the HV- O_h site

With the high degree of symmetry in the TV- T_d and HV- O_h sites, the classic Jahn-Teller triplet structure would be expected in the excitation spectra, which is observed for the 591 nm emission

peak in Figure 2.3. This emission line is assigned to the TV- T_d site, as the calculated excitation spectrum agrees well with the simulation presented in [67]. The other prominent emission line at 577 nm does not exhibit symmetric Jahn-Teller splitting, thus is not likely to be associated with the HV- O_h site. A suitably asymmetric trapping site can be formed by removing 5 Xe atoms in a double-pyramid shape (5V- D_{3h} site) at a grain boundary between an fcc crystal and a hexagonal-close-packed (*hcp*) crystal structure, sometimes observed in SXe samples (shown in Fig. 2.6). This site has one long axis, and 2 short axes, which matches the expected structure for the 577 nm line's excitation spectrum. The emission and excitation spectra of this site were simulated and found to agree with experimental data [67]. Therefore the 591 nm line is assigned by Davis et al. to the TV- T_d site, and the 577 nm line is assigned to the 5V- D_{3h} site [67].

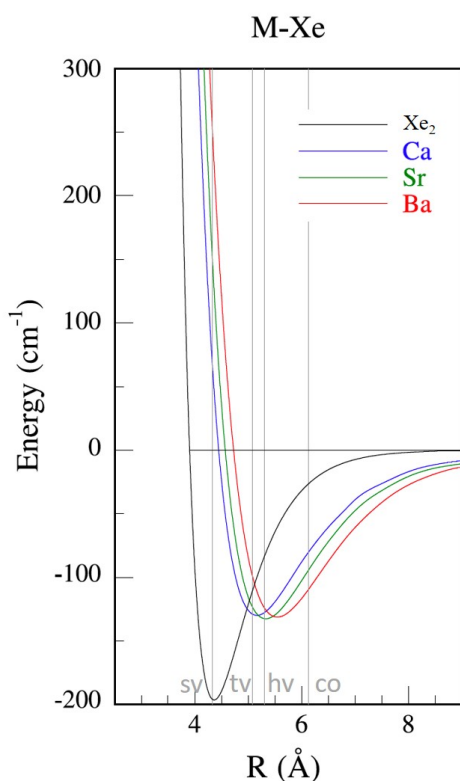


Figure 2.5: The potential as a function of inter-nuclear distance is shown for a Xe dimer, and alkaline earth metal-Xe molecules, simulated using a coupled-cluster (CCSD(T)) method. The black curve shows the Xe-Xe bond length to be 4.33Å, as expected in the pure Xe crystal. The red curve shows the interaction potential for the Ba-Xe system. The different vacancy site nearest neighbor distances are shown as vertical gray lines. Figure from Ref. [58].

The assignment of the 619 nm line to a matrix site via the excitation spectrum presents a challenge, since the excitation spectrum consists of a single, broad peak. The suggestion that a single vacancy (SV) site is responsible for the 619 nm emission was made by J.G. McCaffrey [70]. A possible mechanism for formation of these size-mismatched sites was developed by Silverman and Fajardo [71] for Na atoms trapped in solid Ar (SAr). This is a good analogy for the Ba/SXe system since there is a similar mismatch in the Ar-Ar (3.76 Å [72]) and Na-Ar (4.9 Å [54]) bond lengths, compared to 4.33 Å for Xe-Xe and 5.55 Å for Ba-Xe. It was found that when Na was deposited from an ion source or by laser ablation, a higher fraction of Na atoms were formed in the SV site compared to deposition by a thermal Na atom source [71,73–75]. In the mechanism proposed, Na⁺ ions prefer the SV site due to their tighter binding with Ar (2.79 Å [76]) than Na atoms. Similarly for Ba in SXe, the Ba⁺-Xe bond length is 3.619 Å [59], which is easily accommodated by the Xe matrix. The ions later neutralize, but are strongly confined in the SV site by the surrounding Ar matrix resulting in a cramped configuration. Upon neutralization, the Ba atoms are stuck in the cramped SV site, and the creation of additional vacancies is energetically unfavorable due to the cohesion energy of the Xe matrix. A cartoon of the difference in atomic and ionic deposition is shown in Fig. 2.7.

Models of Ba excitation and emission in SV sites of SXe have been done by B. Gervais [77]. The simulated excitation spectrum predicts weak three-fold JT splitting, but the structure is unresolved resulting in the broad single peak that is observed. The width of the simulated excitation spectrum agrees reasonably well with experiment. The peak positions of the excitation and emission spectra disagree with the observed values. However, the uncertainty in the models used is greater in the repulsive part of the potential, which is more important in the Ba/SXe SV site. Work is ongoing to improve the model of the cramped configuration of the SV site. Given the spectral shape agreement of the preliminary model, and good analogy to the Na/SAr site formation mechanism, the 619 nm line is assigned to Ba atoms in SV sites of the SXe matrix.

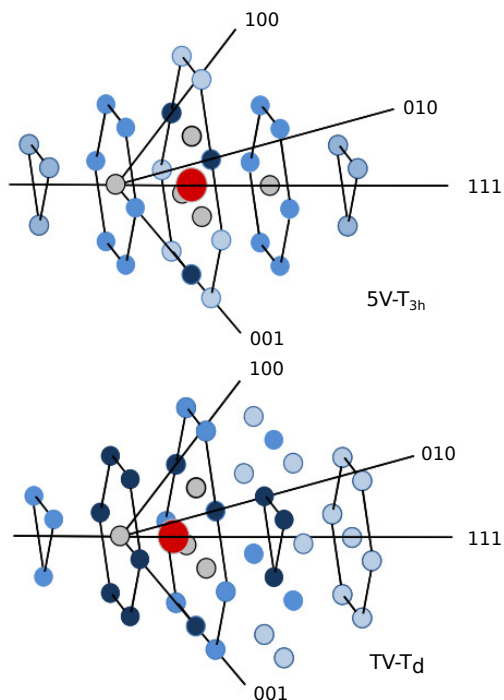


Figure 2.6: Diagrams of the vacancy sites assigned to the 577 nm (upper) and 591 nm (lower) emission lines. The gray circles represent the Xe atoms that are removed to make the vacancy site, and the red circles represent the Ba atom in the site. Figure from Ref. [67].

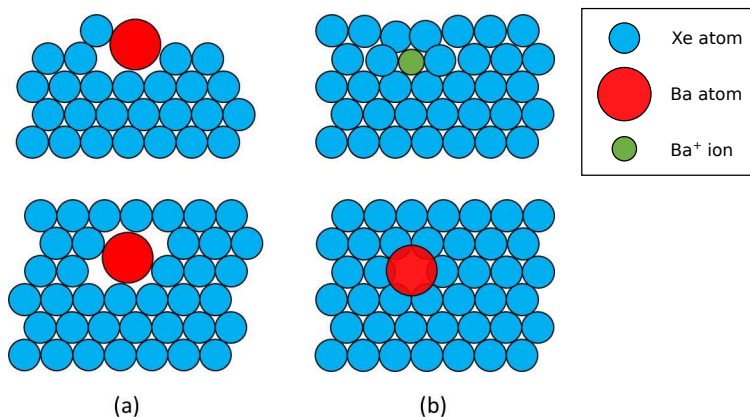


Figure 2.7: Formation of trapping sites when deposited as Ba atoms (a) and Ba⁺ ions (b) in a co-deposited SXe matrix. In the Ba atom case, the atom is too large (5.5 Å) to fit in an SV site (4.33 Å), and forms a larger vacancy site as the SXe matrix grows. In the Ba⁺ ion case, the tighter binding of the ion (3.619 Å) with the Xe atoms allows it to occupy an SV site. After neutralization (b, lower panel), the Ba atom is trapped by the cohesion energy of the matrix to the cramped SV site.

2.2.3 Bleaching of Barium Fluorescence

A limiting factor for the sensitivity of single atom fluorescence imaging is the number of photons that can be collected from the atom to be imaged. In the case of large Ba deposits in SXe, it has been shown that the rate of fluorescence photon emission drops with increased laser exposure [43], a process known as bleaching. The smooth decay of fluorescence signal is an ensemble effect that arises from individual atoms ceasing to fluoresce with some characteristic lifetime. When considering a single atom, this slow decay becomes an abrupt drop when the atom stops fluorescing. The two strongest emission lines at 577 nm and 591 nm exhibit bleaching, as shown in Figure 2.8. The 619 nm line shows little or no bleaching at the relatively low laser intensity used for that data, but has been observed to bleach at the higher intensities of a focused laser beam [49]. This low bleaching rate allows for more total fluorescence photons to be emitted, increasing the achievable sensitivity using the 619 nm emission line relative to the faster bleaching lines at 577 nm and 591 nm.

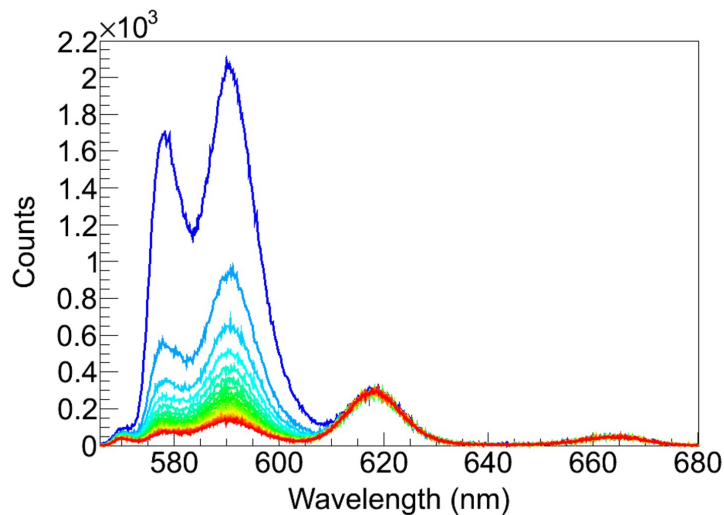


Figure 2.8: Successive spectra of Ba fluorescence with excitation at 556.9 nm. Each spectra has an exposure time of 1s, with every tenth exposure plotted from dark blue to dark red. The 577 nm and 591 nm lines exhibit fluorescence bleaching, while the 619 nm line shows nearly no loss of fluorescence [49].

One possible mechanism to consider to explain the observed bleaching effect is transitions to metastable states such as the $6s5d^{1,3}D$ states shown in Figure 2.1. If the electron makes a transition

to one of these states, the decay to the ground $6s^2\ ^1S_0$ state is parity forbidden in vacuum, and the electron may remain in the metastable state for a significant amount of time. While the electron is in this metastable state, it will not be excited by the laser, and thus will not fluoresce. For our Ba/SXe system, transitions from the 1P_1 state to the 1D_2 and $^3D_{1,2}$ states occur in vacuum at rates $>10^3\ \text{s}^{-1}$. The $^3,^1D$ states have quite long lifetimes of over $\sim 0.25\ \text{s}$ (see Table 2.1). This can cause a significant population to build up in the $^3,^1D$ states, leading to bleaching of the fluorescence. A 5-level model of Ba atoms using the $6s^2\ ^1S_0$, $6s6p\ ^1P_1$, $6s5d\ ^1D_2$, $6s5d\ ^3D_2$, and $6s5d\ ^3D_1$ states was used in Ref. [49] to model the bleaching process of Ba atoms in SXe. When the vacuum transition rates were used, the simulated fluorescence bleaching rate only agreed with experiment for the first few hundred excitations of the most rapidly bleaching 591 nm line, after which the predicted bleaching rate is greater than observed. The 577 nm and 619 nm lines bleach more slowly, and the vacuum model clearly disagrees with experiment.

The Ba atom wavefunctions in SXe are modified from those in vacuum by the interactions with the SXe matrix. This could change the transition rates from their vacuum values and alter the selection rules for the transitions. In the $^3,^1D \rightarrow ^1S$ case, the odd parity component of the Ba-Xe interaction could mix these even parity states with the odd parity $^3,^1P$ states, relaxing the parity selection rule. If so, the $^3,^1D \rightarrow ^1S$ transition rate would be increased, which would mitigate the bleaching effect, since less population builds up in the metastable $^3,^1D$ states.

The $^3,^1D$ states are not the only states between the 1S and 1P states of the recycling transition. There are three 3P states as well (shown in Fig. 2.1). Transitions from the 1P state to the 3P states are parity forbidden ($\Delta l = 0$) in vacuum. In the BaXe molecule, however, the $^1\Pi$ (light blue) and $^3\Sigma$ (yellow) molecular states derived from the 1P and 3P atomic states, cross as shown in Figure 2.9. This may allow for a non-radiative transition from the $^1\Pi$ state to the $^3\Sigma$ state. In gas-phase studies [78], collisions with noble gases have been found to exclusively populate the 3P_2 state. This level crossing is understood to be the mechanism for this population transfer. The probability of this transition may be matrix site specific, since the crossing point may be different when Ba interactions with multiple neighbor Xe atoms are included [67, 79]. This has been suggested as a

possible mechanism for the fluorescence bleaching observed [67]. However, this 3P_2 state has fairly fast (order $10^2 - 10^5 \text{ s}^{-1}$) transitions to the $^3,^1D$ states in vacuum (see Table 2.1), from which the atom could further decay to the 1S ground state by the process described in the previous paragraph.

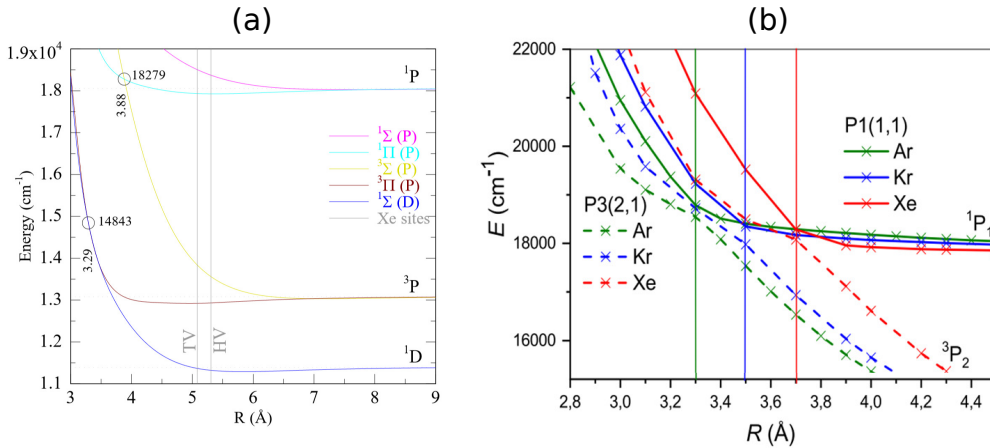


Figure 2.9: The potential curves, calculated by MCRI, for the principal excited states of the Ba-Xe molecule. The crossing between the 1P and 3P states in (a) is of particular note, allowing population transfer non-radiatively. However, with spin-orbit coupling included in the model, (b), this crossing is avoided. Figures from Refs. [67] and [79] respectively.

2.3 Fluorescence Efficiency

Fluorescence efficiency (ϵ_f) is defined as the ratio of fluorescence photons emitted to the excitation photons absorbed. In vacuum, the fluorescence efficiency for the $553.5 \text{ nm } ^1P \rightarrow ^1S$ emission is determined by branching ratios, and is very high. In SXe, non radiative transitions may compete with the fluorescence transition, reducing the efficiency. Fluorescence efficiency can be calculated from experimentally determined quantities with equation 2.2.

$$\epsilon_f = \frac{F}{W_{12}N_1\epsilon_{tot}} \quad (2.2)$$

In this equation, F is the number of fluorescence photons observed per atom per second, $W_{12}N_1$ is the excitation rate from the ground state, and ϵ_{tot} is the total efficiency of the light collection and detection system. For low excitation rates where population does not build up in other states,

$N_1 \approx 1$, which is assumed for this work. W_{12} is the excitation rate, calculated by

$$W_{12} = \frac{\sigma I}{h\nu} \quad (2.3)$$

where σ is the absorption cross section, I is the excitation laser intensity, and $h\nu$ is the excitation photon energy.

For an atom in vacuum, the absorption cross section as a function of photon frequency (ν) is given by

$$\sigma(\nu) = A_{21} \frac{g_2}{g_1} \frac{c^2}{8\pi n^2 \nu^2} g(\nu) \quad (2.4)$$

Here, A_{21} is the spontaneous emission rate, g_1 and g_2 are the degeneracies of the ground and excited states respectively, and $g(\nu)$ is the normalized lineshape of the transition. For natural (lifetime) broadening of a transition, the lineshape is Lorentzian, given by equation 2.5,

$$g(\nu) = \frac{\Delta\nu_N/2\pi}{(\nu - \nu_o) + (\Delta\nu_N/2)^2} \quad \Delta\nu_N = \frac{A_{21}}{2\pi} \quad (2.5)$$

where $\Delta\nu_N$ is the natural linewidth, and ν_o is the central frequency. The maximum cross-section at the central frequency, considering only natural broadening is

$$\begin{aligned} \sigma_{max} &= A_{21} \frac{g_2}{g_1} \frac{c^2}{8\pi n^2 \nu_o^2} g(\nu_o) \\ g(\nu_o) &= \frac{2}{\pi \Delta\nu_N} = \frac{4}{A_{21}} \\ \sigma_{max} &= \frac{g_2}{g_1} \frac{c^2}{2\pi n^2 \nu_o^2} \end{aligned} \quad (2.6)$$

Since a Ba atom in SXe experiences perturbations from the potential of the surrounding Xe matrix, the absorption cross-section in SXe (σ_{SXe}) is broadened beyond the natural linewidth. If the integrated cross-sections are assumed to be equal, the cross-section is given by

$$\sigma_{SXe} = \sigma_{max} \frac{\Delta\nu_N}{\Delta\nu_{SXe}} g_{SXe}(\nu) \quad (2.7)$$

where σ_{max} is defined in Eq. 2.6 above, $\Delta\nu_N$ and $\Delta\nu_{SXe}$ are the natural and excitation spectrum linewidths respectively, and $g_{SXe}(\nu)$ is the lineshape of the excitation spectrum with the peak normalized to unity. The result is shown in Fig. 2.10. Using the estimated cross-section and the parameters used for the excitation, the fluorescence efficiency can be estimated from Eq. 2.2.

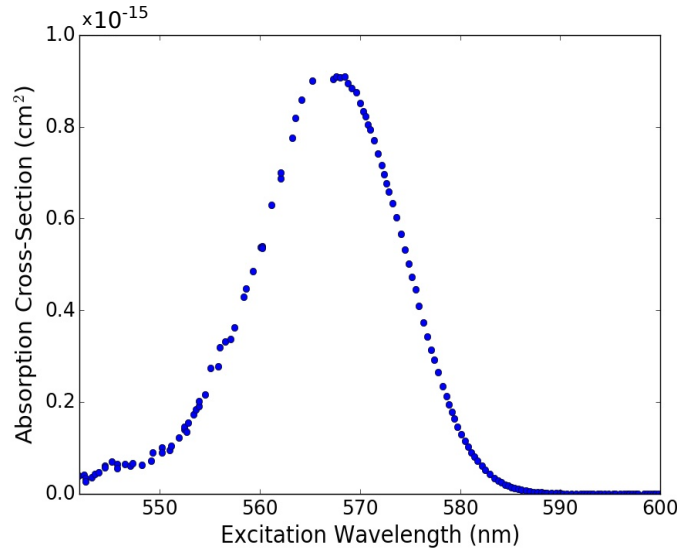


Figure 2.10: Estimated absorption cross section for Ba atoms in SXe.

2.4 Signal Models of Ba Atom Images

The expected signal from a given density of Ba atoms has been modeled for the case of a fixed laser position, and then extended to simulate scanning the laser over a very sparse deposit. The expected signal from a barium deposit is modeled in two steps. First, the barium atoms are placed randomly according to the specified area density of the atoms in the SXe matrix. Second, the response from each Ba atom in the laser region is modeled. A study of the ideal parameters for laser scanning experiments can be determined.

2.4.1 Fixed Laser Image Simulation

The placement of the Ba atoms is done randomly in either a square or a circular area. Each simulation uses 1×10^4 Ba atoms, and the area is varied to yield the different Ba atom densities. For example, to achieve a density of 1 atom per laser area, the area over which the atoms are distributed is set to 1×10^4 times the laser area. The laser area is calculated by measuring the beam width at the focusing lens and then propagating the Gaussian wavefront through the remaining optical elements and finding the minimum spot size as the beam exits the surface of the sapphire window. The spot sizes are $3.22 \mu\text{m}$ in x and $2.85 \mu\text{m}$ in y. The 45° tilt of the window introduces a factor of $\sqrt{2}$ to the spot size in the plane of the window for the y direction, with this taken into account, the y spot size used in the model is $4.03 \mu\text{m}$. Since the area over which the Ba atoms are distributed is much larger than a single laser area, the border shape of the distribution (square or circular) does not affect the results from the simulation.

After the Ba atoms are placed, the total signal is simulated by summing the contributions of each atom. A plot of the laser intensity and Ba atoms is shown in Fig. 2.11. The signal of each atom is assumed to be proportional to the laser intensity at the Ba atom position. A Ba atom centered in the laser emits the “full” response. After running many simulations at various Ba atom densities, the slope of a weighted linear fit to the simulated data vs. number of Ba atoms in the laser area is 1.00 ± 0.03 , shown in Fig. 2.12. The average fluorescence is proportional to the number of atoms in the laser region as expected. Variations in fluorescence signal at low atom density are significant. At one atom on average per laser region, the standard deviation of the signal level in 1000 simulations is 0.72 of the one atom average signal. Thus, the peak signal at a Ba density of one atom per laser area will vary significantly in any given observation. For the examples shown in Fig. 2.11 (a), (b), and (c), the integrated emission is 0.30, 0.98, and 1.61 times the single atom level respectively. In actual deposits, the number of SV-site Ba atoms per laser region is not measured. Instead, the density of the Ba^+ ions being deposited by an ion beam source is measured. Since the imaging technique is only sensitive to SV-site Ba atoms, when comparing these results to experimental data, this factor needs to be taken into account.

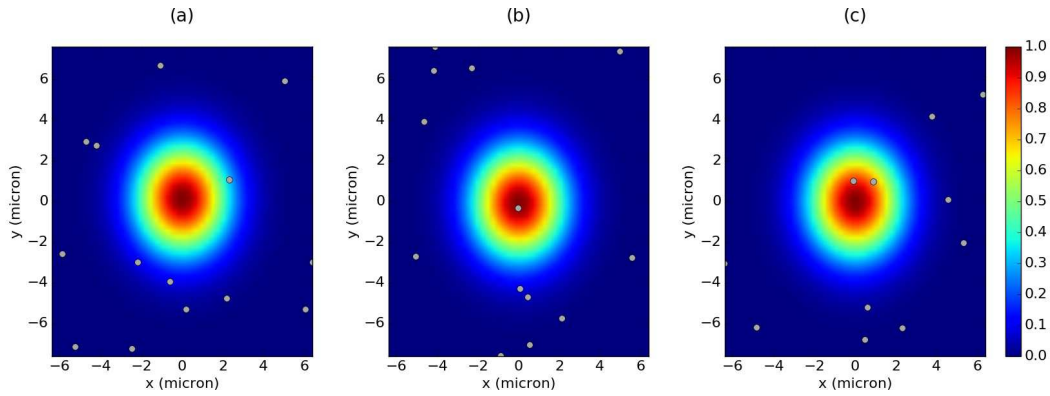


Figure 2.11: Sample images of Ba atom placement in simulation. The gray circles represent the locations of atoms randomly distributed at a density of one atom per laser region. The color scale represents the Gaussian laser beam intensity

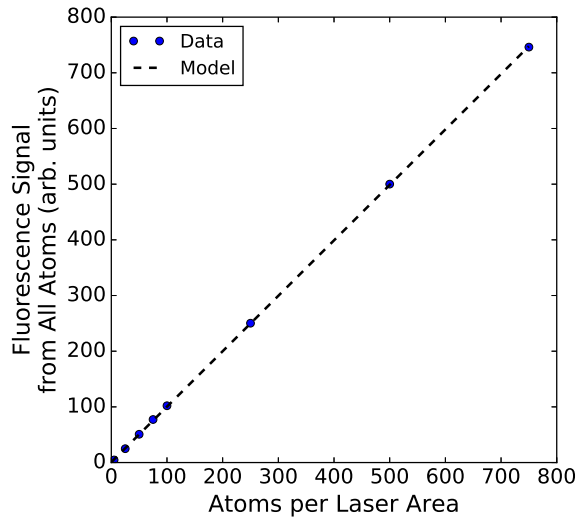


Figure 2.12: The average fluorescence signal is plotted against the Ba atom density per laser area. Each point is the average of 25 simulations. The weighted linear fit shows the average signal to be consistent with the average number of atoms in the laser region.

2.4.2 Laser Scan Simulations

To image individual atoms, a very sparse Ba deposit is made, and the laser is scanned across the sample in a grid pattern. The step size of this grid is a key parameter for achieving single atom imaging. The ideal step size allows for the complete coverage of the scanned area, such that no Ba atoms are missed, but also minimizes overlap to avoid optical bleaching and to allow for a larger area to be scanned. This depends on the spot size of the laser, and for the calculations in this section, the calculated spot size of $w_x = 3.22 \mu\text{m}$ and $w_y = 2.85 \mu\text{m}$ is used. The calculation

of this spot size is given in Sec. 3.6. In Fig. 2.13, three examples of 5×5 grids with step sizes of $2 \mu\text{m}$, $4 \mu\text{m}$ and $6 \mu\text{m}$ are shown. The first position of each grid is half a step size in from the upper left corner of the scan area. The size of the scan area is defined as the number of positions on each side times the step size of the grid, i.e. the 5×5 grids of spacing $4 \mu\text{m}$ are $400 \mu\text{m}^2$. Each simulation evaluates the laser intensity over a mesh of 500×500 points. The grid with $2 \mu\text{m}$ step size (a), has excessive overlap, while the $6 \mu\text{m}$ step size (c) does not cover the region sufficiently. Fig. 2.13 (b) shows a compromise that corresponds to the actual spacing of $4 \mu\text{m}$ used in the scanning experiments presented in Chap. 4.

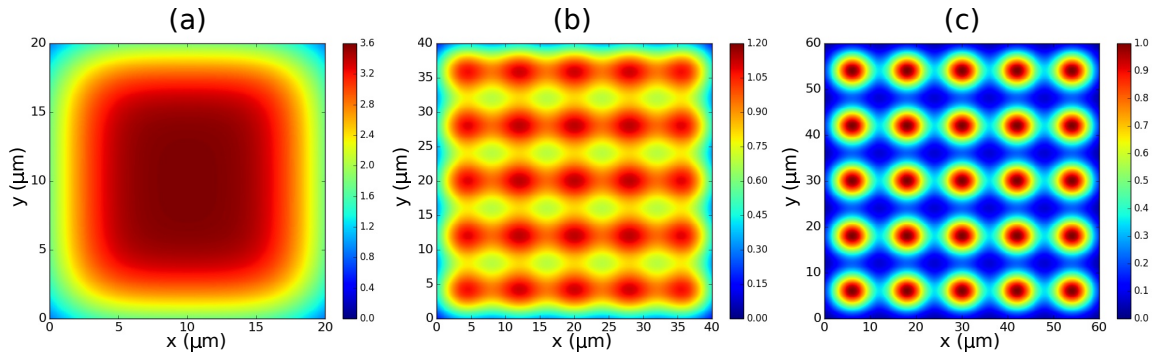


Figure 2.13: Three scan grids with x-spacings of (a) $2 \mu\text{m}$, (b) $4 \mu\text{m}$, and (c) $6 \mu\text{m}$. The area plotted in the figures are the scan areas as defined in the text.

The coverage and overlap parameters can be quantified by analyzing the simulated laser grids shown in Fig. 2.13. The coverage is defined as the area that would be considered “inside” the e^{-1} laser beam intensity area for fixed laser experiments. The overlap is defined as the area that experiences more than the peak laser intensity. These areas were calculated by using the value at each point in the finely pitched grids used to create the images in Fig. 2.13. If the value is over e^{-1} (0.37), it counts as a covered spot. If the value is over 1 (the maximum laser intensity), it counts as an overlapped spot. The ratios of the number of these points to the total number of points in the simulation give the coverage and overlap ratios respectively. These are plotted against step size in Fig. 2.14. The ideal step size region with full coverage and minimal overlap is between about $4 \mu\text{m}$ and $5 \mu\text{m}$.

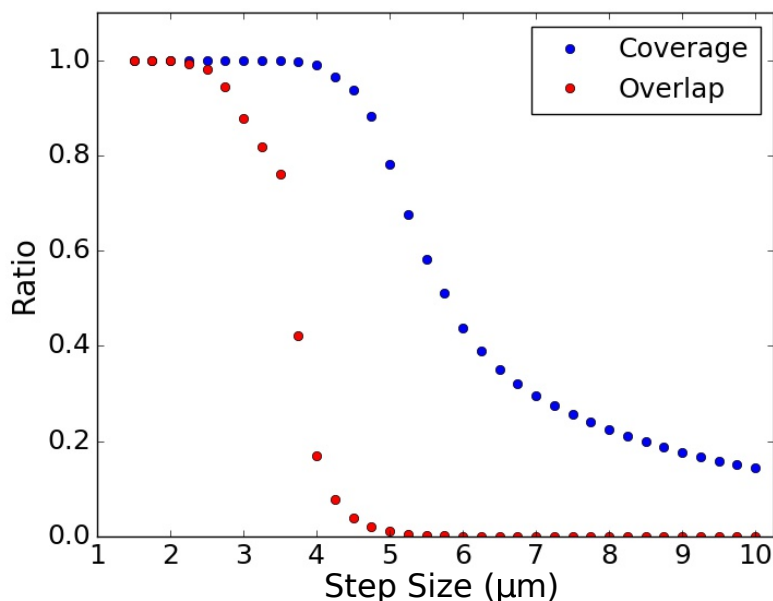


Figure 2.14: Coverage and overlap ratios are plotted as a function of step size. The step sizes between 4 μm and 5 μm provide nearly full coverage of the area with low overlap.

2.4.3 Scanned Laser Image Simulation

A simulation of the scanning procedure is done by moving the laser center location in a step-wise raster scan pattern. A set number of resonant Ba atoms are placed randomly within the scanned area, each assumed to have the same fluorescence response, and no bleaching effect. The total signal for each laser position is calculated in the same way as the fixed laser simulation described in Sec. 2.4.1. In these simulations, no background fluctuations have been added. A composite image of the surface is created by arranging the integrals from each individual laser position into a 2D array corresponding to the laser position as is done experimentally. A 2D heat map as well as a 3D plot of two such simulations are shown in Fig. 2.15, with the locations of the three simulated atoms shown as gray dots in the heat map. In (a) and (b), the calculated laser spot size of $w_x = 3.22 \mu\text{m}$ and $w_y = 2.85 \mu\text{m}$ is used with a step size of 4 μm , as used in experiments. In this simulated scan, most of the signal from the atoms is confined to one laser position, with minimal signal detected in adjacent laser positions. In Fig. 2.15 (c) and (d), another scan is simulated (different atom positions) with a larger laser spot size of $w_x = 5.72 \mu\text{m}$ and

$w_y = 6.64 \mu\text{m}$ and the same step size as in (a) and (b). This scan shows that significantly more signal is seen in laser positions adjacent to the atom position, similar to the experimental results. The locations of the atoms and the summed signal from the 3×3 pixels surrounding the atom position are given in Table 2.2. To investigate the average peak and total fluorescence of Ba atoms in a scan image, 100 such scan simulations were done. In these simulations, only one atom was placed in the scan area to avoid overlap of atom signals. For the scans with the calculated spot size of $w_x = 3.22 \mu\text{m}$ and $w_y = 2.85 \mu\text{m}$, the average peak signal is 0.64 ± 0.21 , and the average total signal is 0.91 ± 0.12 . The lack of laser overlap leads to the total signal being close to the full response, with about $2/3$ of the signal in the peak laser positions. When the laser size is increased to $w_x = 5.73 \mu\text{m}$ and $w_y = 6.62 \mu\text{m}$ to better reflect the experimental conditions, the average peak signal is 0.86 ± 0.08 , and the average total signal is 2.99 ± 0.29 . With the increased laser overlap, the total signal is more than the full response of the atom. The peak value is closer to the full response than in the ideal laser spot size case, and contributes only about $1/3$ of the total signal.

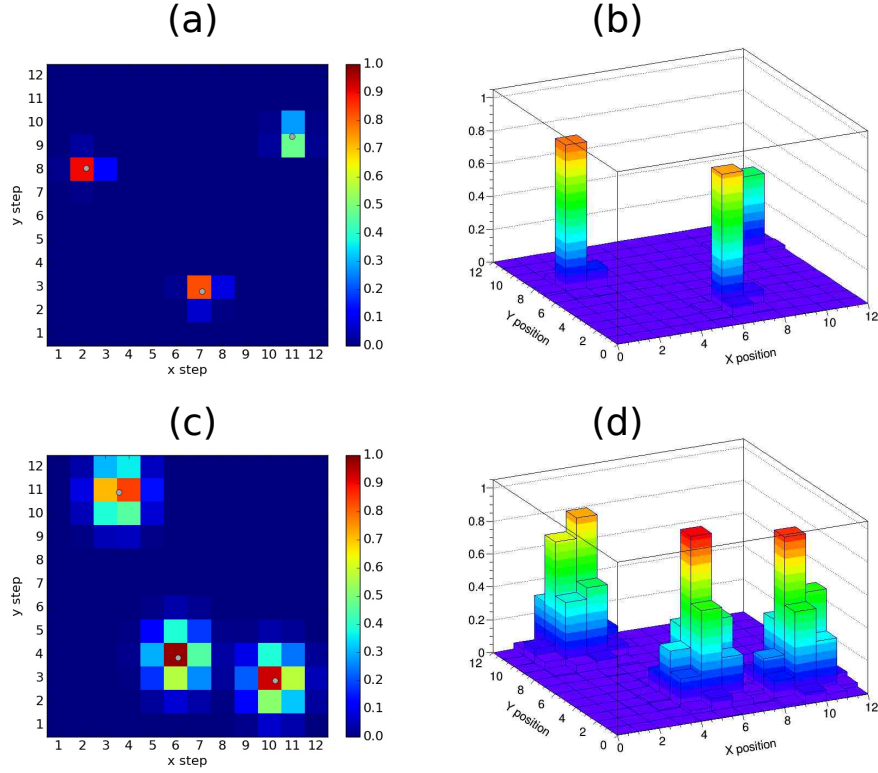


Figure 2.15: Two separate scanning images simulated with different laser spot sizes. The same step size of $4\ \mu\text{m}$ was used in both simulations and the experiment. In the first simulation ((a) and (b)), the calculated spot size of the laser was used ($w_x=3.2\ \mu\text{m}$, $w_y=3.8\ \mu\text{m}$). In the second scan ((c) and (d)), a larger spot size of $w_x=5.73\ \mu\text{m}$ and $w_y=6.62\ \mu\text{m}$ was used.

Table 2.2: Summary of the locations and fluorescence of the atoms simulated in Fig. 2.15.

w_x	w_y	Atom	Location (x,y)	Peak Signal	Total Signal
3.22 μm	2.85 μm	1	(7.1,2.8)	0.83	1.01
		2	(11.0,9.4)	0.48	0.80
		3	(2.1,8.1)	0.90	1.08
5.73 μm	6.62 μm	1	(10.3,2.9)	0.93	2.81
		2	(3.6,10.9)	0.84	2.64
		3	(6.1,3.9)	0.98	2.87

Chapter 3

Experimental Apparatus and Method

In this chapter, the apparatus and experimental conditions are described. Sec. 3.1 describes the accelerated ion beam used as a source of Ba/Ba⁺ for fluorescence tagging. The method for co-deposition of the barium ions into a SXe matrix is discussed in Sec. 3.2. The laser system used for excitation of Ba/Ba⁺ is described in Sec. 3.3, and the collection of the fluorescence is discussed in Sec. 3.4. The methods used to analyze the fluorescence images and laser exposure are discussed in Sec. 3.5. In Sec.3.6, the method for measuring the laser beam width by examining images of Ba atoms is described. Finally, the cryogenic system for achieving the temperatures needed for fluorescence is discussed in Sec. 3.7.

3.1 Ion Deposition System

The ion beam system to produce barium ions is shown in Figure 3.1. The source is a commercial Colutron G-2 ion gun. It produces a clean source of metal or gas ions by accelerating and collimating ions through a mass filter to select a particular isotope. This is followed by a series of Einzel lenses and deflection plates that direct the beam to the deposition window. A pair of pulsing plates are used to provide $\sim 1 \mu\text{s}$ bunches of ions, allowing for very low density deposits. The beam is measured by several Faraday cups, as well as induction plates.

3.1.1 Ion Source

The source of barium ions for the beam is the Colutron (now Beam Imaging Solutions) Model DCIS-101 ion gun, shown in Figure 3.2. This source is capable of producing ions with a low energy spread, suitable for mass selection by a velocity filter. The ions are produced in an alumina (Al₂O₃) chamber where the solid sample, held in a hollow stainless steel rod capped with a set-screw, is vaporized with a hot tungsten filament. This filament also acts as the cathode for the discharge, which ionizes the vaporized atoms. The anode for the discharge is a thin sheet of tantalum with

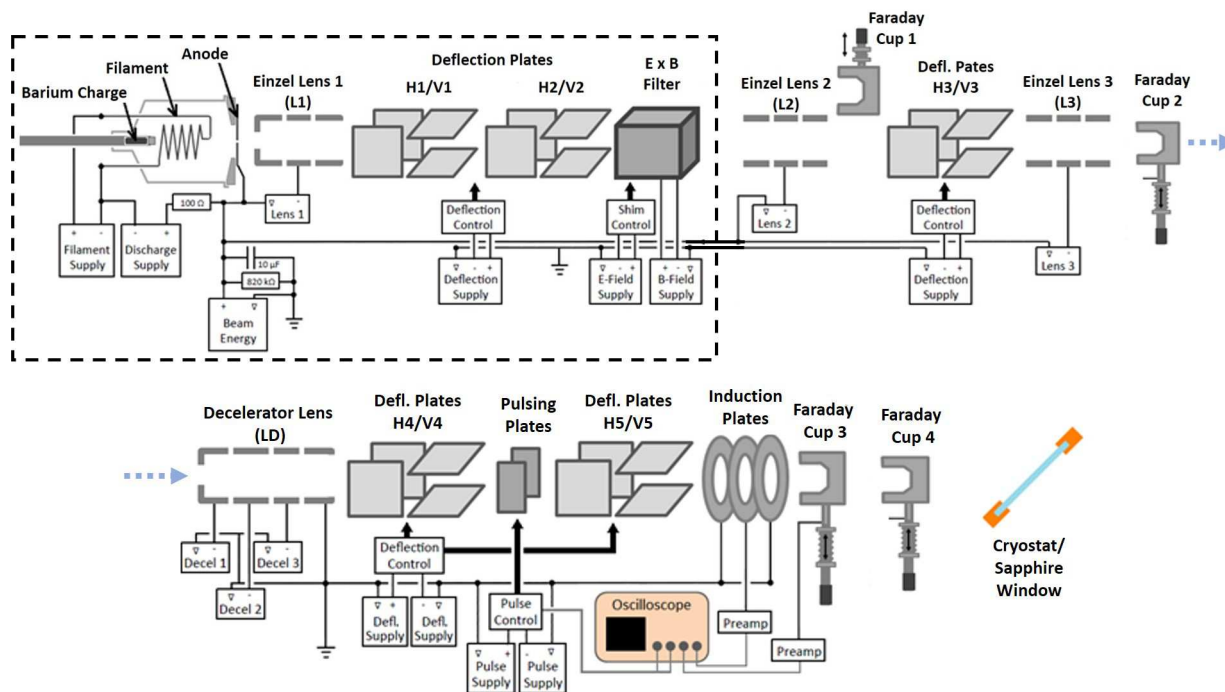


Figure 3.1: A schematic drawing of the ion beam system used for Ba^+ deposition. The dashed box contains the elements of the Colutron Model G-2 ion gun. The arrow indicates the path of the ions from the upstream section (upper) to the downstream section (lower).

a 0.5 mm hole in the center. The entire source chamber is held at the acceleration voltage for the ion beam, and is electrically isolated from the rest of the system. The is mounted onto the end of the chamber by an alumina cap, which contacts the heat-sink inside the vacuum system, cooled by recirculation of R-134a non-conductive coolant. The filament and anode are connected to stainless steel rods, which connect to the electrical feedthroughs on a 2-3/4" Conflat flange. This flange has a central gas tube that mates with the chamber to serve as the sample insertion tube, which is closed by an Ultra-Torr fitting between the tube and source rod. This modular design allows for the Ba sample to be changed without removing the entire source chamber, and for easy removal of the chamber for replacement of parts or cleaning as required.

The discharge in the vapor between the filament and anode creates a dense plasma of ions, preventing the field created by the acceleration voltage from penetrating into the chamber where the ions are produced through the anode hole [80]. This reduces the amount of mass spreading

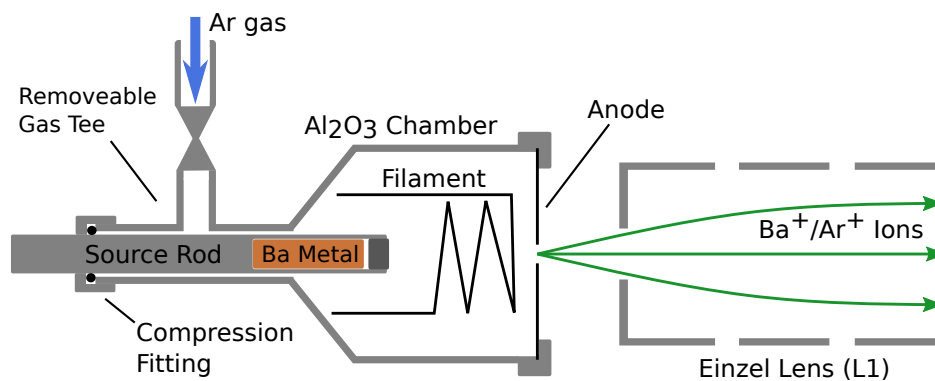


Figure 3.2: The Colutron (now Beam Imaging Solutions) ion gun source and Einzel lens (L1).

that would be introduced if the ions were accelerated through the aperture by the external field. Ions exit through the anode hole, and are focused by the plasma meniscus formed at the hole to a crossover point very near the anode, with a ~ 0.05 mm diameter. From this crossover point, the ions are accelerated by the anode through a 9.5 mm aperture at the entrance to the first Einzel lens (L1), held at -2000 V relative to the anode (at ground potential in this configuration). L1 is used to approximately collimate the ion beam for transmission through the $E \times B$ mass filter. Two sets of vertical and horizontal deflection plates after the lens are used to align the beam to the central axis before entering the mass filter, though the second set are not generally required, and are set to ground potential.

3.1.2 Mass Filter

The ions extracted from the source are mass-selected by a Wien filter, also known as an $E \times B$ velocity filter. This ensures that only Ba is present in the ion beam, producing a clean sample for single-atom detection. The Colutron 6" $E \times B$ filter (now Beam Imaging Solutions Model 600-B), shown schematically in Fig. 3.3, follows the source described in the previous subsection.

The filter separates masses by balancing the forces caused by the applied magnetic and electric fields, allowing ions with a specific velocity to pass undeflected to the sample window. Since all of the ions produced are accelerated to 2 keV, the different masses will have different velocities. The velocity as a function of mass can be derived via conservation of energy

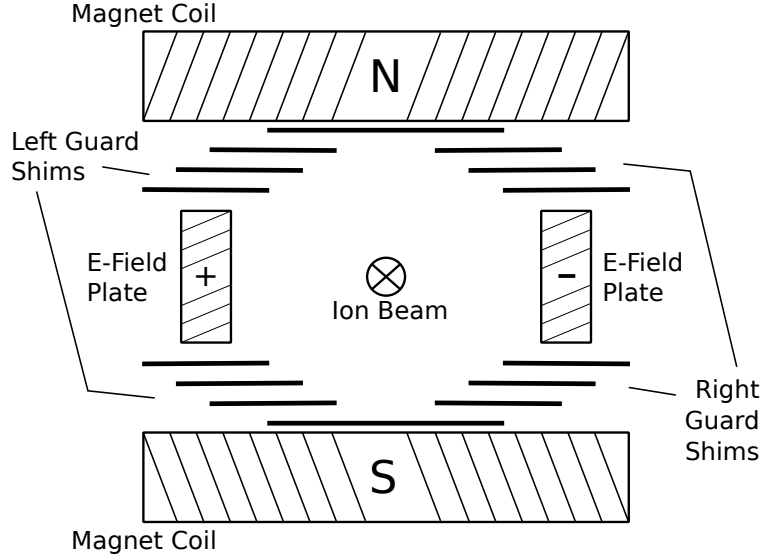


Figure 3.3: Drawing of the Colutron 6" E×B mass filter (now Beam Imaging Solutions Model 600-B). The left and right guard shims are wired symmetrically above and below the beam center to create no net vertical electric field.

$$\begin{aligned} \frac{1}{2}mv^2 &= qV \\ v &= \sqrt{\frac{2qV}{m}} \end{aligned} \quad (3.1)$$

where m is the mass of the ion, q is its charge, and V is the acceleration voltage.

The deflection of the ions is done with perpendicularly oriented electric and magnetic fields. The forces on the ions can be calculated, and the undeflected condition derived by setting the net force on the ion to zero.

$$\begin{aligned} \vec{F}_{EM} &= \vec{F}_E + \vec{F}_B = 0 \\ q\vec{E} + q\vec{v} \times \vec{B} &= 0 \\ \implies v &= \left| \frac{E}{B} \right| \end{aligned} \quad (3.2)$$

Thus, the ratio of the electric and magnetic fields determines the velocity that is passed by the filter.

To relate this to the mass, one can substitute into Equation 3.1, and solve for $\frac{m}{q}$.

$$\frac{m}{q} = 2V \frac{B^2}{E^2} \quad (3.3)$$

The E-field is supplied by two parallel plates, with the voltage split evenly between the two plates, i.e. if the voltage from the bipolar supply is 200 V, the plates will be at ± 100 V (relative to ground). The guard shims are used to create a uniform electric field perpendicular to the beam axis throughout the length of the filter. They are supplied in pairs symmetrically above and below the central axis, so as to create zero net vertical field in the center of the filter. However each vertical pair of plates on either side can be adjusted independently to optimize the beam shape. Fringe effects cause cylindrical focusing of the ion beam, diagrammed in Fig. 3.4. This focusing effect occurs as ions are accelerated or decelerated when they cross equipotential lines above and below the central plane of the filter. Since the ions change velocity, the Lorentz force is no longer zero, causing deflection of the ions towards the center of the beam. The guard shims counteract this effect by creating an electric field gradient that strengthens the field by the negative plate, and weakens it by the positive plate. Thus, the accelerated ions see a stronger electric field, and the decelerated ions see a weaker field, resulting in a Lorentz force of zero for the ions entering the filter off-axis as well as those on-axis at a given velocity.

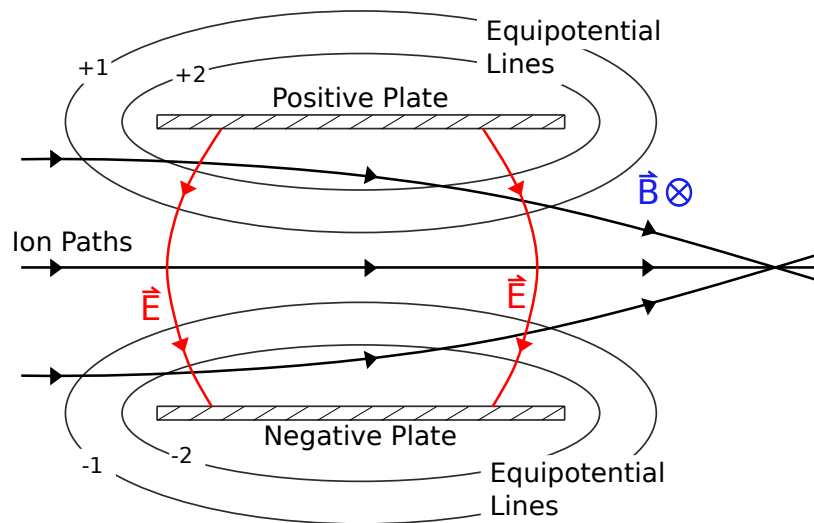


Figure 3.4: Three ion paths are shown passing through an un-shimmed $E \times B$ filter. The central path is undeflected, since it runs parallel to the equipotential line on the central axis of the filter. The upper path crosses positive equipotentials and is slowed, reducing the magnetic force and causing a downwards deflection by the greater electric force. The lower path is accelerated, thus resulting in an upwards deflection in the same manner. Overall, a net focusing effect occurs in the vertical direction, causing cylindrical lensing of the ion beam.

The parameters E and B are measured and adjusted to ensure transmission of Ba^+ through the filter. Two coils supply the B-field, and the field strength as a function of current has been measured [81]. The nominal values for the electric field plates, magnetic coils and guard shims are given in Table 3.1. Since the electric field is fairly uniform in the center of the filter, the equation $E = -\Delta V/d$ can be used to approximate the electric field from the supplied voltage. Thus, by measuring the voltage on the E-field power supply and the current on the B-field power supply, the mass of the undeflected beam can be calculated. The E-field can be swept while keeping the B-field constant to obtain a mass profile of the ion beam.

Table 3.1: Nominal parameters for $E \times B$ filter elements.

Element	Setting
Electrostatic Plates	180 V
Magnetic Coils	9.8 A
Left Shims (L1,L2,L3)	(67 V,45 V,22 V)
Right Shims (R1,R2,R3)	(-22 V,-45 V,-67 V)
Middle Shim	0 V

3.1.3 Beam Focusing and Steering

After exiting the mass filter described in the previous section, the ion beam passes through a series of ion optics. A full schematic diagram with all of the components is shown in Fig. 3.1. This ion beam system was originally designed to allow for deposition of atoms at energies from 200 eV to 2 keV [82,83]. In this work, it has been re-configured to run at 2 keV only. In short, the supplies for the ion optics excluding the Einzel lenses between the source and the decelerator lens (LD) are now referenced to ground instead of the acceleration power supply (called "Beam Energy" in Fig. 3.1). The wiring configuration of the power supplies for the ion beam is shown in Fig. 3.1.

The ions are weakly focused by Einzel lens 2 (L2), to ensure transmission through the apertures downstream in the system. A set of deflection plates (H3/V3) are used to keep the beam on-axis, though they are generally at $V = 0$ in normal operation. Following this, a pair of lenses are used to

Table 3.2: Nominal voltages on ion beam steering and focusing elements.

Element	Voltage (V)
Lens 1 (L1)	1610
Lens 2 (L2)	935
Lens 3 (L3)	0
Decelerator (LD)	-1800
H1/V1	30/-10 \pm 10
H2/V2	0/0
H3/V3	0/0
H4/V4	0/0
H5/V5	0/0 \pm 25

focus the beam onto the sample. The first lens (L3) is a simple Einzel lens, the second is a special deceleration lens. This lens was installed to allow for both focusing and slowing of the ions. Since the ion beam is operated at 2 keV for this work, it is used as a simple Einzel lens by setting all but the second electrode to ground potential. During normal operation, L3 is not used, i.e., the central electrode set to ground potential. The final focusing of the beam is done by LD, using a voltage that produces a desirable Ba⁺ density at the sample, i.e. it is not entirely focused at the sample. Two sets of deflection plates (H4/V4 and H5/V5) are used to make final adjustments to center the beam on the sample window. In normal operating conditions, only H5/V5 are used to make a slight adjustment to the beam direction. Table 3.2 summarizes the nominal voltages used during normal operation of the ion beam.

3.1.4 Ion Beam Measurements

The ions are measured by a series of four Faraday cups placed along the beam path. Faraday cups consist of a charge collecting electrode, shielded by a grounded cylinder with a small aperture to allow the ions to enter. A cut-away CAD model of cup 4 is shown schematically in Fig. 3.5. When the ions strike the electrode, a current is induced as electrons move to neutralize the charge deposited. This current is proportional to the rate of ions striking the electrode, and can be used to calculate the ion current in the beam. If the ions striking the electrode are of sufficient energy, they can cause emission of secondary electrons from the surface of the electrode. If the secondary

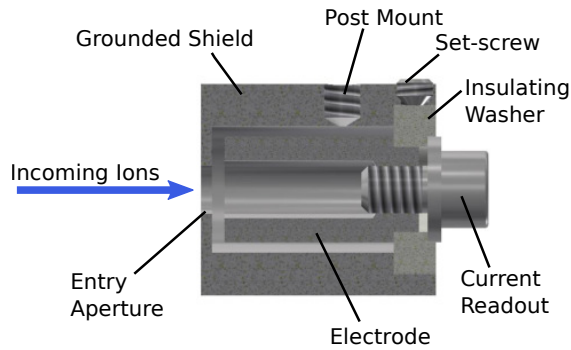


Figure 3.5: Cross-section of a CAD drawing of Faraday cup 4. The diameter of the grounded shield is 12.7 mm, with an entry aperture of 2.95 mm. The electrode has an inner diameter of 3.45 mm and depth of 8.89 mm. The insulating washer is made of Macor, and held in place by a set-screw. The current is read out by a coax wire connected between the bolt and the metal washer at the back of the cup.

electrons later strike the electrode, this does not affect the measured value of the ion current. If the secondary electron is not recaptured by the electrode, the loss of an electron appears as if an additional ion was collected, resulting in a measurement higher than the real ion current. For this reason, deep and narrow electrodes are used to limit the solid angle through which the secondary electrons can escape. The electrode can also be given a positive bias low enough to avoid reflecting the incoming ions, but large enough to cause the secondary electrons (which have lower energy than the ions) to return to the electrode. Faraday cups block the beam when making a measurement and thus cannot be used during a deposit. For this reason, the cups are mounted on bellows to allow the beam to be sampled before a deposit and passed during a deposit. The two upstream cups (1 and 2 in Fig. 3.1) are used to measure the current and check alignment before entering the final focusing section of the beam. The downstream cups (3 and 4 in Fig. 3.1) are placed close to the sample, and are used to ensure that the beam is directed straight along the beam axis at the sample. A fifth Faraday cup (w) was occasionally installed in place of the sapphire window and used for calibration as discussed in Sec. 3.1.6.

3.1.5 Ion Beam Pulsing

A pulsing system for the ion beam has been implemented to allow for low density barium deposits. A pair of pulsing plates, held at +200 V and -200 V deflect the beam off the sample

window. They are brought to 0 V for $\sim 1 \mu\text{s}$ during which a pulse of Ba^+ ions are allowed to pass undeflected. A LabVIEW program is used to trigger a Wavetek Model 162 function generator, with a 5 V TTL signal lasting 1 ms. The function generator produces a 5 V square wave lasting $\sim 1 \mu\text{s}$ triggered on both the rising and falling edges of the TTL signal from the LabVIEW program. This results in two pulses per repetition of the LabVIEW program. A fast high voltage pulser (Directed Energy PVM-4210) provides the deflection voltage and brings the plates to 0 V during the time the square wave signal is at 5 V. By selecting the number of repetitions of the LabVIEW program, the density of the ion deposit can be chosen.

The pulses can be measured by the Faraday cups described in the previous section and by a set of induction plates, located between the final deflection plates and Faraday cup 3. The induction plates are a set of 3 circular electrodes with a hole in the center of each. The first and last plates are held at ground to shield the center electrode until the ions are close. As the ions approach and recede, the center electrode experiences an induced current following Ramo's Theorem (Equation 3.4):

$$I = E_{1V} qv \quad (3.4)$$

Where I is the induced current, q is the charge, v is the velocity. E_{1V} is the electric field at the charge position when 1 V is applied to the electrode, with all other conductors at ground. Measuring this induced current gives a qualitative measure of the ion bunch quality, i.e. the induction signal on the oscilloscope should be fairly symmetric, indicating the bunch passes the plates with high transmission. When operated in pulsing mode, the Faraday cups and the induction plates are read out by an eV Products eV-5092 preamplifier which converts the current signal to a voltage signal recorded on a digital oscilloscope.

The effective circuit diagram for the preamplifiers is shown in Figure 3.6. Reconstruction of the current can be done with the following equation [49]

$$I = -\frac{1}{RM} \left(V_{out} + RC \frac{dV_{out}}{dt} \right) \quad (3.5)$$

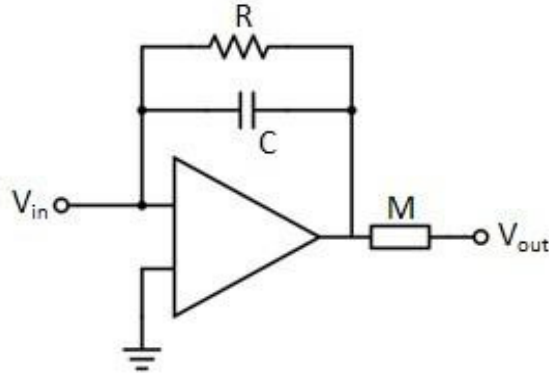


Figure 3.6: The simplified circuit of the eV Products preamplifiers is shown. The circuit uses an integrator block consisting of an op-amp and a parallel RC circuit feedback. It multiplies the output of the integrator by gain M , and this signal is recorded on the oscilloscope.

The parameters RM and RC were determined by inputting a square current pulse to the preamplifier through a calibrated capacitor [49]. RC was measured by fitting the exponential decay of the calibration signal. RM was then determined by matching the amplitude of the calculated current and the input current. The raw and reconstructed signals from the average of 128 1.2 fC pulses measured by cup 4 and the induction plates are shown in Figures 3.7.

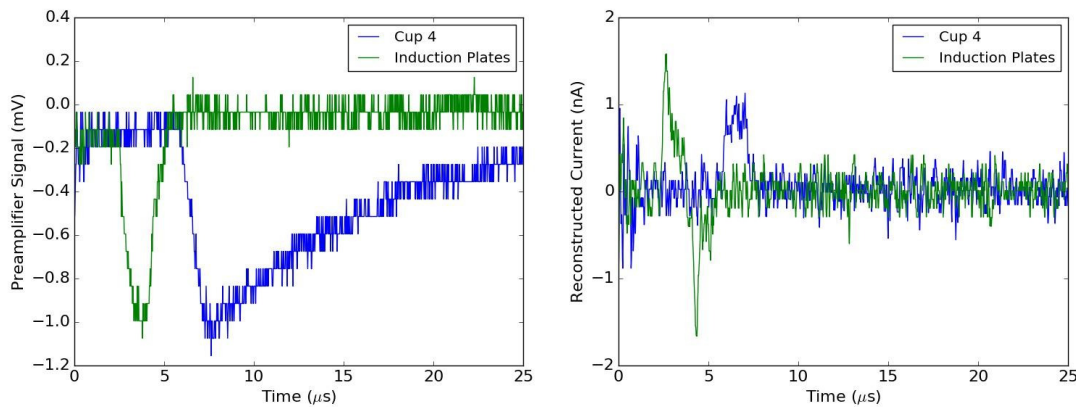


Figure 3.7: The (a) raw and (b) reconstructed signals of ion pulses into Faraday cup 4. The integrated current of reconstructed signal for cup 4, which is the total charge of the ion pulse, is 1.2 fC.

The velocity of the pulse can be measured using the delay between the induction signal and the cup signal and the distance between these components. By measuring the velocity, we can calculate

the mass of the ions in the beam. For cup 4 (cup w), the delay of $3.44 \pm .04 \mu\text{s}$ ($4.39 \pm .05 \mu\text{s}$) for a distance of $185 \pm 5 \text{ mm}$ ($230 \pm 5 \text{ mm}$), gives a mass of $133.0 \pm 5.5 \text{ amu}$ ($140.7 \pm 5.0 \text{ amu}$). Combining the mass measurements for both cups, the mass is $137.0 \pm 3.7 \text{ amu}$, confirming that the beam is composed of barium ions.

3.1.6 Calibration of Ion Deposits

At certain times a Faraday cup is installed in place of the sapphire window (cup w). By comparing the charge of pulses measured by Faraday cups 3 and 4 to a measurement by cup w, a calibration of the charge density at the window position was done. The beam profiles were measured by using the final deflection plates (H5/V5) to change the beam position. From the geometry and location of the deflection plates, the transverse deflection per volt of plate bias can be calculated using the equation

$$\frac{\text{deflection}}{\text{plate bias}} = \frac{z l}{2 d V_{acc}} \quad (3.6)$$

where z is the distance from the end of the plates to the measurement spot ($z = 19.6/22.6, 32.1/35.1, 36.6/39.6 \text{ cm}$ for H5/V5 to cups 3, 4, and w respectively), $V_{acc} = 2 \text{ kV}$ is the acceleration voltage, $l = 25.4 \text{ mm}$ is the length of the plates, and $d = 38.1 \text{ mm}$ is their separation distance. This was calculated for each cup and the values are given in Table 3.3. The deflection values were verified by comparing the deflected distance at several voltages to the horizontal displacement of cup 4 by a micrometer-actuated bellows that is needed to find the peak.

Table 3.3: Calculated values of transverse ion beam deflection per volt of plate bias for H5 and V5 at cups 3, 4 and w.

	H5 Deflection (mm/V)	V5 Deflection (mm/V)
Cup 3	0.0327	0.0377
Cup 4	0.0535	0.0585
Cup w	0.0621	0.0671

The profiles taken on 16 May 2018 are plotted in Figure 3.8. This data was taken by measuring the charge collected by cups 4 and w as the deflection voltage for one of the directions was changed in steps of 10 V, and the other kept constant on the value that produced the peak current. An ion beam profile was taken for both cup 4 and cup w along both the horizontal and vertical axes. Modeling these profiles allows the ion flux in fC/mm^2 to be calculated for each

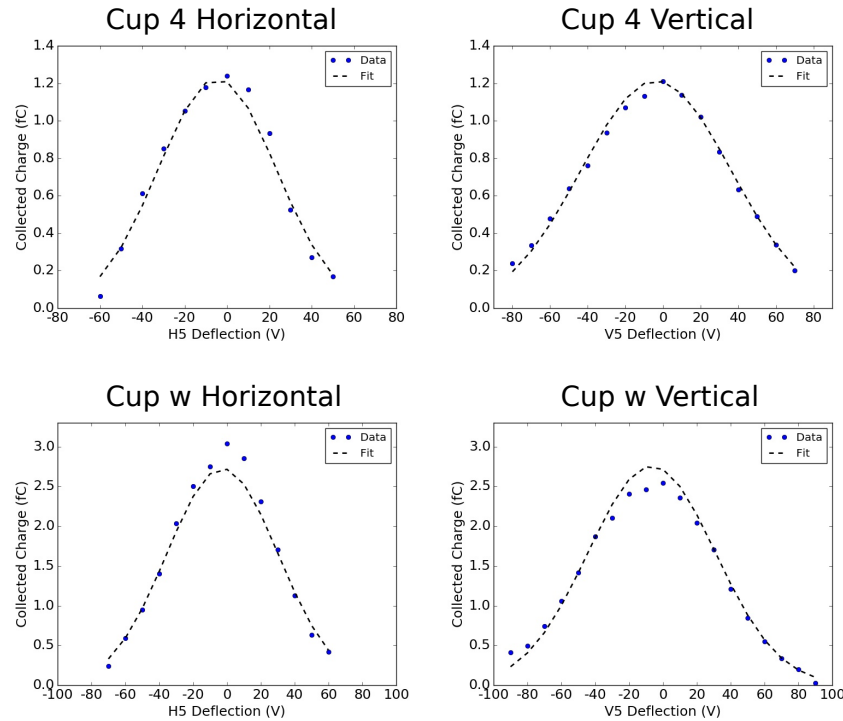


Figure 3.8: Data and fits to the ion beam profile simulation for cups 4 and w in both horizontal and Vertical directions.

cup. Since the ion beam width is close to the same size as the entry apertures of the Faraday cups, 2.08 mm and 3.00 mm for cups 4 and w respectively, they cannot be considered a pinholes ($FWHM_{beam} \gg d_{cup}$). In the simplified pinhole case, the Gaussian shape of the beam is being directly sampled and can be fit. To determine the beam parameters in the case of $FWHM_{beam} \cong d_{cup}$, a computational model was used to simulate the ion beam sampling procedure. First, a Gaussian distribution representing the ion beam was simulated in a 2D grid of 250×250 points. The cup signal is simulated by numerically integrating all the grid points within the cup diameter, shown as the circle in Fig. 3.10. The center of the ion beam was moved relative to the integration region to

simulate the ion beam being deflected in the measured beam profiles. This effect on the measured profile with respect to the Faraday cup aperture size is simulated in Fig. 3.9, keeping the ion beam width fixed. If the cup is smaller or the same size, as in the blue and red curves, the distortion is small. For the cup sizes larger than the beam width (green and purple), the distortion causes the ion beam to appear broader than it actually is.

The collected charge was simulated at each (H5,V5) voltage measured in the profiles, and the residual between the data and the model was minimized to extract the amplitude and widths of the ion beam at both cups 4 and w. The fits are shown in Fig. 3.8, and the extracted parameters are given in Table 3.4. The peak measured charge for the cup w profiles differ by 18%, thus the fits to the cup w data do not agree as well as those for cup 4. The effect of this is to find an intermediate peak density between that corresponding to the two profile peaks.

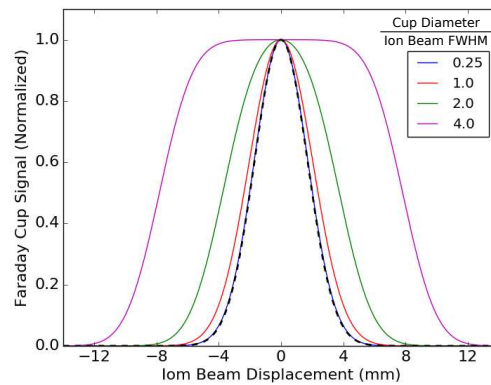


Figure 3.9: The effect of Faraday cup entry aperture size is shown. The simulated ion beam has a Gaussian profile with a FWHM of 4 mm (shown as black dashed line), and the Faraday cup diameter is varied from 1 mm to 16 mm. The peak heights have been normalized to demonstrate the shape differences.

Table 3.4: Best-fit parameters for the Ba⁺ ion beam profile simulation used for calibration of ion density. The uncertainties are the standard error of the fit.

	Cup Diameter (mm)	Amplitude (fC/mm ²)	Horizontal FWHM (mm)	Vertical FWHM (mm)
Cup 4	2.08	0.40 ± 0.01	3.31 ± 0.11	5.31 ± 0.14
Cup w	3.00	0.45 ± 0.01	4.47 ± 0.18	5.66 ± 0.19

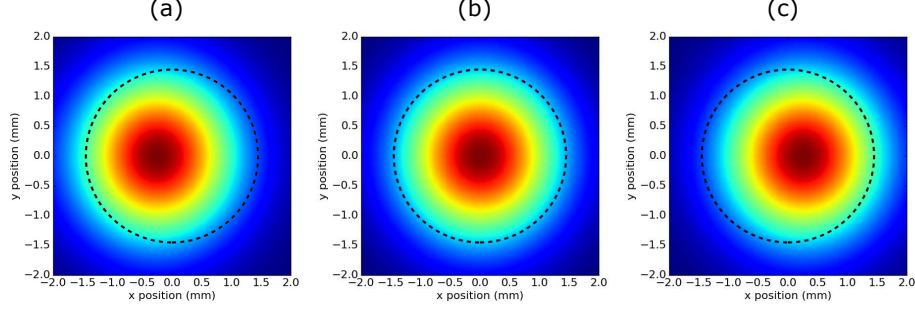


Figure 3.10: Three simulated positions of the ion beam relative to the Faraday cup as the ion beam is deflected to steer it across the plates, yielding a profile. The deflections shown are -0.25 mm (a), 0 mm (b), and +0.25 mm (c).

The area density of ions per pulse at the window, ρ_{ions} , in an experiment (in a plane perpendicular to the ion beam) is calculated by

$$\rho_{ions} = \frac{Q_4}{e} \frac{\rho'_4}{Q'_4} \frac{\rho'_w}{\rho'_4} \quad (3.7)$$

where Q_4 is the charge recorded just before or after an experiment by cup 4 for one pulse and the primed quantities are measured during calibration, e is the elementary charge. The second factor is the ratio of the best-fit value of the peak ion density at cup 4, $\rho'_4 = 0.40$ fC/mm², and the peak collected charge of the profiles taken with cup 4 during calibration, $Q'_{4,cal} = 1.23$ fC. The third factor is the ratio of the best-fit values for the peak densities from Table 3.4 at cups 4 and w, ρ'_4 and ρ'_w respectively during calibration, where $\rho'_w = 0.45$ fC/mm². Canceling out the common factor of ρ'_4 , the equation simplifies to

$$\rho_{ions} = \frac{Q_4}{e} \frac{\rho'_w}{Q'_4} \quad (3.8)$$

Using the calibrated density at the window, the number of ions in an area, A_{obs} , (again perpendicular to the ion beam) is given by the equation

$$N_{ions} = N_{pulses} \rho_{ions} A_{obs} \quad (3.9)$$

where N_{pulses} is the number of pulses of the ion beam. The observed area is defined differently for fixed laser images and scanned laser images. For fixed laser images, is the laser area, and for a

scanned laser images A_{obs} is the total area of the scan. Since the observation region (order μm^2) is much smaller than the ion beam size (order mm^2), the ion density is assumed to be uniform in the observation region. The profiles for cup w used in calibration (Fig. 3.8) differ in charge collected by cup w at the center of the beam by 18%. This affects the best-fit value of ρ'_w through Eq. 3.8. Thus an estimated uncertainty of $\pm 10\%$ is assigned to the ion density at the window.

There is also an uncertainty associated with the consistency of the alignment of the ion beam from cup 4 to the window position. This is estimated from the measured ion beam peak locations for cups 4 and w in Fig. 3.8, which are consistent to within about 10 V of deflection, corresponding to 0.6 mm of displacement. The uncertainty for general experiments is conservatively estimated as 1.0 mm. For the average ion beam width of 5.1 mm, this adds an uncertainty of +0% and -10% to the ion density, since this misalignment can only decrease the ion density observed from the central value.

Another source of uncertainty in the ion density at the window comes from the emission of secondary electrons by the Faraday cups. This uncertainty was estimated by biasing the electrodes of cups 3, 4 and w. A beam profile such as those shown in Fig. 3.8 was taken for each cup at three bias voltages, -15 V, 0 V, and +15 V in both horizontal and vertical directions. When the electrode is negatively biased, it will repel secondary electrons that may be emitted inside the cup, raising the signal. Conversely, a positive electrode bias will attract secondary electrons emitted in the cup. However, the positive bias may also draw electrons emitted from the front grounded plate through the aperture, artificially decreasing the signal. To estimate the effect of secondary electron emission, the peak of the profiles for 0 V and -15 V electrode biases are compared, and the values are given in Table 3.5. The horizontal profile for cup 4 shows an anomalously large difference between the biases. This was the first profile taken, and examination of the peak position indicated the beam drifted while taking this profile, and thus is removed from consideration. From the percent differences in collected charge when the cup is biased, an uncertainty of $\pm 10\%$ is attributed to secondary electron effects.

Conservatively adding the three uncertainties linearly, the uncertainty in the ion density at the window is +20% to -30%.

Table 3.5: Peak collected charge of ion beam profiles with Faraday cup electrodes biased.

	Collected Charge (fC)		Percent Difference
	0 V Bias	-15 V Bias	
Cup 3 Horizontal	14.06	14.41	2.5
Cup 3 Vertical	13.15	12.97	1.4
Cup 4 Horizontal	3.48	3.95	12.4
Cup 4 Vertical	3.31	3.73	11.8
Cup w Horizontal	11.50	9.19	22.3
Cup W Vertical	9.03	9.28	2.7

After the calibration was done, cup 4 was replaced with another Faraday cup with a larger aperture of $d = 2.95$ mm. Profiles of cups 4 and w were done as described above, and were fit using the same ion beam simulation method. The data and fits from these profiles are shown in Fig. 3.11. Due to improvement in cup design and a more similar entry aperture, the charge collected by cups 4 and w are similar. The best-fit values of the simulations are given in Table 3.6. The ion density at cup 4 has a slightly smaller peak and larger width compared to cup w, and likely due to the focus location of the ion beam. The charge of the entire ion beam is the same at cups 4 and w, indicating the response of the cups is the same. For experiments after the cup 4 replacement on June 5 2018, the ion density calibration uses the values from the new fits, i.e. $\rho'_w/Q'_4 = 0.145 \text{ mm}^{-2}$ in Eq. 3.8.

Table 3.6: Best-fit parameters for the Ba^+ ion beam profile simulation used for calibration of ion density for the replaced cup 4. The uncertainties are the standard error of the fit.

	Cup Diameter (mm)	Amplitude (fC/mm ²)	Horizontal FWHM (mm)	Vertical FWHM (mm)
Cup 4	2.95	1.55 ± 0.03	9.77 ± 0.20	4.24 ± 0.14
Cup w	3.00	1.34 ± 0.03	10.16 ± 0.27	4.70 ± 0.18

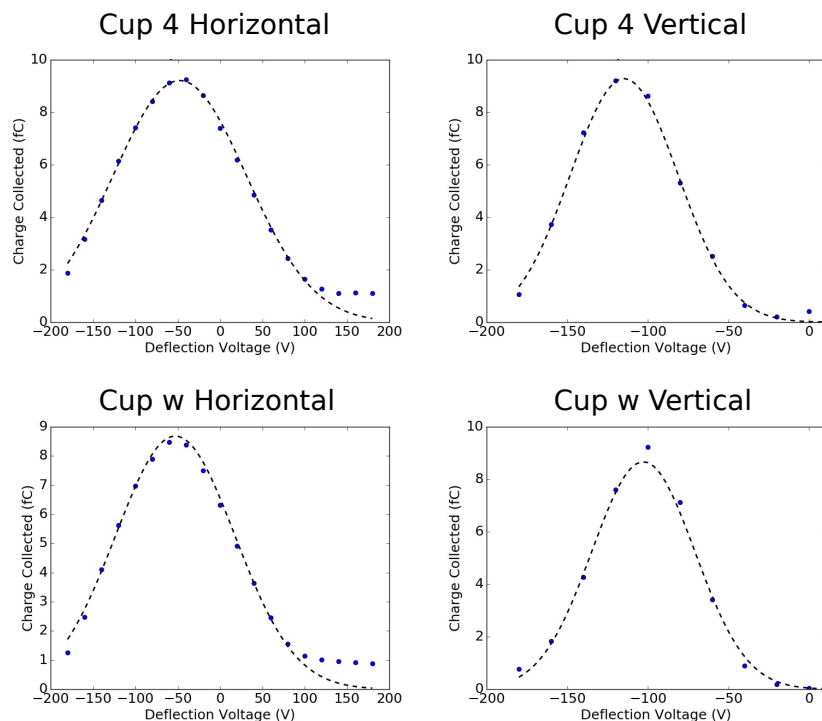


Figure 3.11: Data and fits to the ion beam profile simulation for cups 4 and w in both horizontal and Vertical directions after replacement of cup 4. This calibration was done on 6 June 2018.

3.2 Deposition of Ba^+ Ions into SXe Matrix

The Ba ions from the beam are focused onto a sample window and co-deposited with 99.995% purity Xe gas. The sample window is made of sapphire and cooled to cryogenic temperatures by an Advanced Research Systems Model DE-202 helium cryostat. This compact cryostat uses a two-stage Gifford-McMahon cycle to achieve temperatures of ~ 10 K at the cold finger. The window is held in a copper mount, with a layer of indium foil ensuring good thermal contact between the holder and window. The holder is threaded into the end of the copper cold finger of the cryostat. The temperature is controlled with a Lakeshore Model 325 temperature controller with a 25 W heater and a DT-470 thermal diode mounted to the sample holder. As shown in Figure 3.12, the window is tilted at an angle of 45° away from the ion beam to allow for access of the ion beam and Xe gas from the front, the excitation laser from the rear, and the collection optics from above.

The deposit is done at 50 K, and begins with the flow of Xe into the cryostat, throttled by a needle valve at setting 48 for ~ 6 s. This allows a small and controlled amount of Xe to be deposited

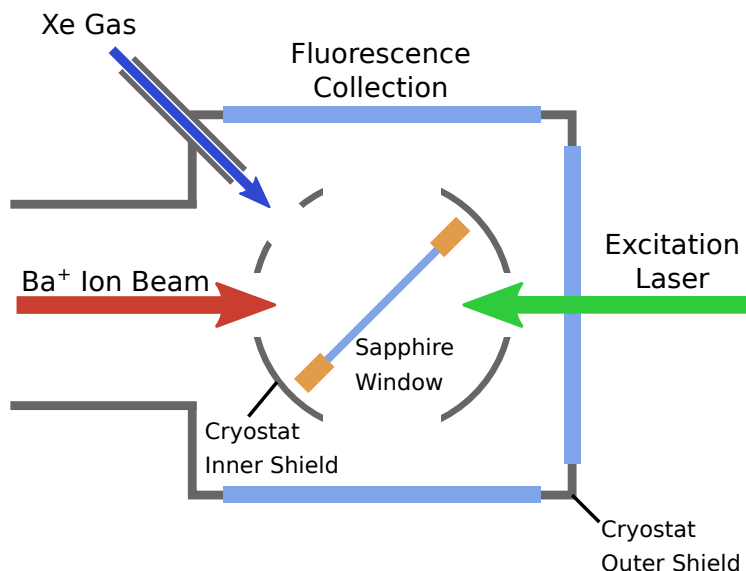


Figure 3.12: Sample window geometry, including the deposition, excitation and collection systems.

on the sapphire window before the Ba is implanted. Faraday cup 2, used as a beam block, is then retracted and the ion beam is pulsed, which may take a few seconds for a large (~ 5000) number of pulses. The ions pass through the induction plates to the window, and the induction signal is recorded on the oscilloscope. Cup 2 is then re-inserted, blocking the ion beam and also possible neutral atoms from the source. The flow of Xe is then stopped after another ~ 6 seconds. Thus the Ba^+ ions are implanted approximately in the middle of a SXe layer and isolated from any additional deposits of residual gases present in the vacuum system. The cryostat is cooled further to 11 K for observation. The process of deposition takes about 12-16 s from the time Xe gas is turned on to when it is shut off, depending on the number of Ba^+ pulses and how long the Xe is allowed to flow. In this time, a SXe layer of ~ 400 nm is deposited.

The growth rate of the SXe layer has been measured via the observation of interference fringes. The reflection of a 532 nm laser, sent in from the excitation laser beam path, was measured on a power meter, as shown in Fig. 3.13. As the SXe layer grows the reflection from the window surface and the SXe surface constructively and destructively interfere. Figure 3.14 shows these interference patterns for a variety of needle valve settings at 50 K.

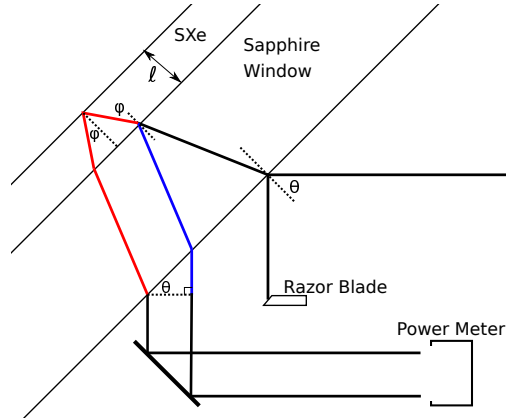


Figure 3.13: This diagram shows the set-up for the interference fringe measurement. The two separate paths are shown in red and blue, and this path difference is used to derive Eq. 3.10. The razor blade is used to remove interference from the reflection off the back of the window. In practice, the reflections are focused to allow the backside reflection to be picked off, and the reflections of interest to overlap on the power meter.

The growth rates are calculated from the period of the interference pattern (determined by fitting a sine function) by the following equation,

$$\frac{dl}{dt} = \frac{\lambda}{2Tn\cos(\phi)} \quad (3.10)$$

$$\phi = \sin^{-1}\left(\frac{\sin(\theta)}{n}\right)$$

where θ is the angle of the window with respect to the laser, ϕ is the refracted angle in the SXe, $\lambda = 532 \text{ nm}$ is the laser wavelength, $n=1.45$ is the index of refraction of SXe, and T is the interference oscillation period. The SXe growth rate with the typical setting of 48 is $T = \sim 6 \text{ s}$ and $dl/dt = \sim 34 \text{ nm/s}$.

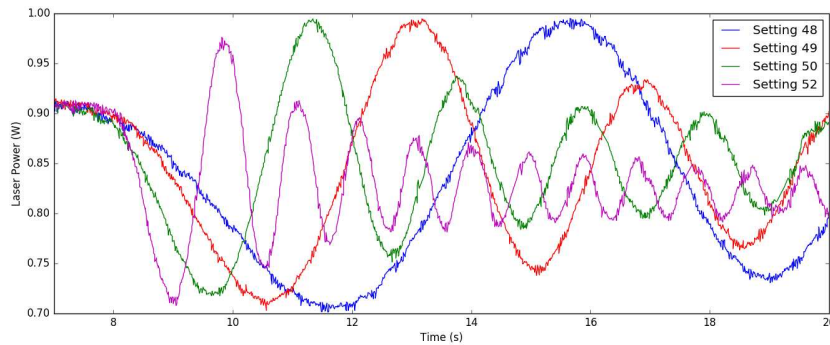


Figure 3.14: Interference fringes for 4 settings of the needle valve at 50 K.

After an experiment has been performed, the sample is heated to 100 K to evaporate the SXe deposit from the window. The Xe evaporates between 73 K and 78 K, as seen in Fig. 3.15, a recording by a Stanford Research Systems Model residual gas analyzer (RGA).

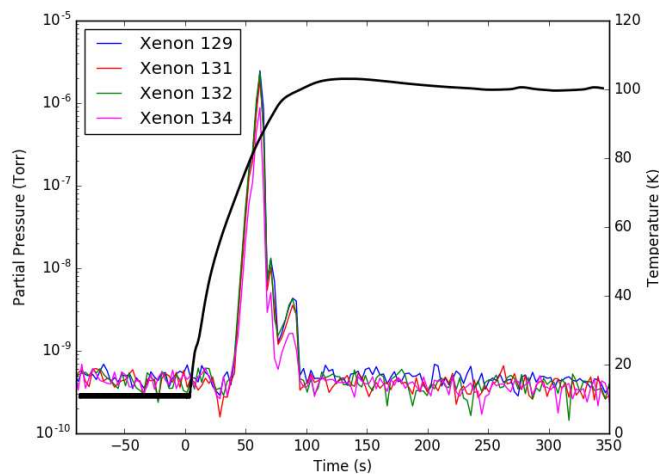


Figure 3.15: RGA data of SXe sample evaporation. The Xe layer evaporates between 73 K and 78 K. The residual gases such as hydrogen, nitrogen and oxygen also evaporate from the cryostat and possibly the window when the cold finger is heated.

3.3 Laser Excitation System

Barium atoms in solid xenon are excited by a Coherent 599 dye laser. Two dyes were used to cover the excitation spectrum from 542 nm-590 nm. Initially, Rhodamine 110 (R110) dye was used covering the lower wavelength range from 542 nm-566 nm. This dye was pumped by the 514 nm line of a Lexel-3500 Ar ion laser. The second dye used to cover the range 567 nm-590 nm is Rhodamine 6G (R6G), initially pumped by the same Ar ion laser as the R110 dye. To increase the output power of the R6G dye, the pump laser was changed to a Verdi V8 532 nm doubled Nd:YVO₄ laser, since the absorption of the R6G peaks near 532 nm [84]. The Coherent 599 dye laser uses a rotateable birefringent filter and a pair of thick and thin etalons in the laser cavity to select the output wavelength of the laser. In earlier work, only the birefringent filter was used, since the limited pump power of the Ar ion laser made achieving lasing in the cavity with the

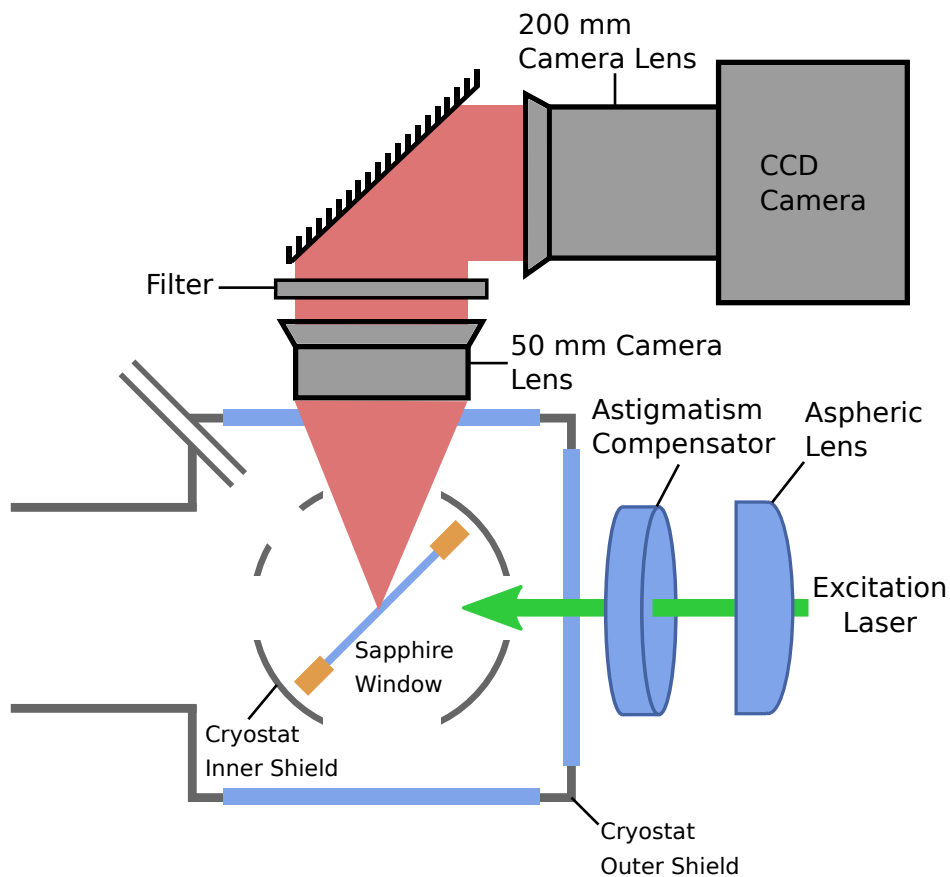


Figure 3.16: Schematic diagram of the optical setup showing both the laser focusing and fluorescence collection optics. The excitation laser is focused by a 7.9 mm focal length aspherical lens through the astigmatism compensator. The fluorescence is collimated by a 50 mm camera lens, passed through a filter to select the fluorescence peak of interest, and focused onto the CCD camera by a 200 mm camera lens.

etalons unfeasible. After the Ar ion pump laser was replaced by the Verdi laser, the etalons were installed to further narrow the emission of the dye laser to ~ 900 GHz (FWHM). The output of the laser was also passed through a sharp short-pass filter, tilted to cut right above the laser wavelength before being sent to the cryostat. This eliminates longer wavelength spontaneous emission of the dye from reaching the window.

The excitation and collection optics for the fluorescence tagging test setup are shown in Figure 3.16. For imaging of small numbers of atoms, and especially for the scanned imaging technique, achieving a small laser spot size and obtaining a sharp image of the fluorescence light are desirable. An aspherical lens (ThorLabs ASL10142-A) of focal length 7.9 mm was used to focus the laser on a small area. The 45° tilt of the sapphire window (Figure 3.12) introduces astigmatism

on the incoming laser beam. This astigmatism limits the minimum laser area that can be achieved since the x and y focal positions are different. To minimize the spot size, an astigmatism compensator is placed after the lens and just outside the cryostat. The compensator is an optical flat of 12.5 mm thickness placed at an angle of 9° in the opposite axis (y-axis) to the tilt of the window. The angle required to make the x and y focal positions the same was calculated by ray matrix analysis assuming a Gaussian laser beam. The angle was then finely adjusted to find the optimal focus size of the laser. This was done by recording images of the scattered light on the sapphire window as the lens is moved in steps along the optical axis. The spot was fit at each step by a 2D Gaussian (Eq. 3.11) to extract the image radii at $1/e^2$ intensity (“spot size”), w_x and w_y .

$$f(x, y) = Ae^{-\frac{2(x-x_0)^2}{w_x^2}} e^{-\frac{2(y-y_0)^2}{w_y^2}} \quad (3.11)$$

Plots of the image spot size vs. lens position are shown in Fig. 3.17. The location of minimum of these curves is the focal position, but the minimum image spot size is not the actual laser spot size due to the resolution limits of the camera ($20 \mu\text{m}$ pixels) and collection optics. This technique is used to ensure that the astigmatism compensator is at the correct angle, as indicated by the minima occurring at the same lens position.

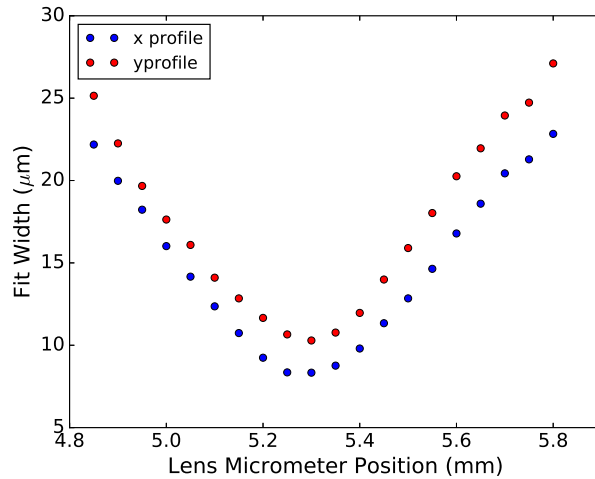


Figure 3.17: The x and y laser spot sizes from a 2D Gaussian fit to CCD images plotted vs. lens position. The location of the minimum indicates the optimal position of the lens for focusing.

By taking the measured laser beam size at the laser lens, $w_x = 3.36$ mm and $w_y = 3.80$ mm, and propagating it through the compensator, sapphire window, and half the SXe layer, the expected spot size can be calculated. The theoretical spot size for the dye laser pumped by the Verdi laser $w_x = 3.22$ μm and $w_y = 2.85$ μm . This assumes that there is no broadening due to scattering at the window surface where the laser beam enters, and the laser is a perfect TEM₀₀ mode. Fits to scanned images of Ba atoms indicate that the apparent laser spot size is somewhat larger than this theoretical prediction. The method used to estimate the apparent laser spot size and results is discussed in Sec. 3.6 later in this chapter.

A Melles-Griot No. 3 iris shutter (called the "laser shutter") is used to prevent bleaching of the Ba fluorescence from exposure to the excitation laser when the sample is not being imaged and is also used to reduce the effect of cryostat vibration. A LabVIEW program controls the laser shutter, allowing it to open only when the camera shutter is open, exposing the sample only when the fluorescence is being recorded. This program also measures the laser power with a Si-diode photometer (EG&G Model 460-1A meter and Model 460-2 diode) with the reflection from a pick-off plate and stores the time and power data in a separate file for each image. The ratio of the transmission to reflection of the pick-off plate is measured each day, to calculate the correct laser power incident on the sample window. The total exposure (power \times time) for each image is measured by integrating the power vs. time data of each image. The exposure time of each image is calculated by counting the data points where the laser is on, and multiplying by the measurement period for each point (22 ms on average).

3.3.1 Laser Scanning

The observation of individual Ba atoms in a resonant laser is an important advance that is required for barium tagging in nEXO. A wide (order mm²) laser beam could be used to image a large area all at once. However, this method is limited by the resolution of the light collection system. In this work, a focused laser is scanned over an area much larger than the laser spot size in a grid pattern. This is shown schematically in Figure 3.18. As the laser moves near a barium atom,

the fluorescence increases, and then decreases as the laser moves away. In this case, the resolution is limited by the size of the laser spot and grid spacing, allowing for potential improvement of the resolution. The implementation of laser scanning is done by moving the excitation laser lens.

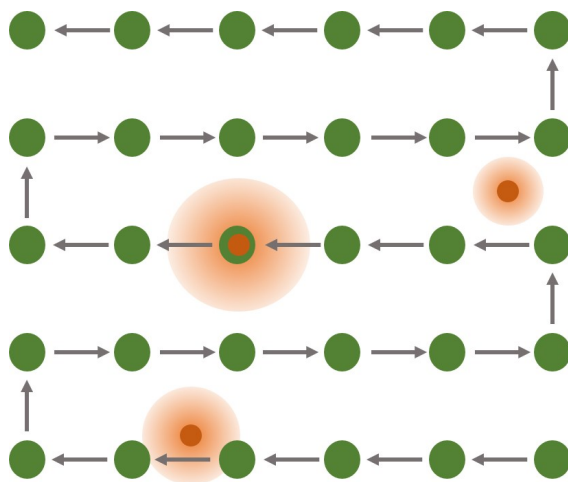


Figure 3.18: As the laser spot (green) is scanned in a raster pattern across the sample, it passes near individual Ba atoms (orange).

For a parallel input beam, the laser beam at the focus is moved sideways the same amount as the lens. Thus, scanning the lens in a grid pattern scans the laser across the sample in a similar pattern. Since moving the lens means the laser will not be aligned with the optical axis at all positions, an aspheric lens is used to reduce the aberrations.

The lens is mounted to two Newport CONEX-AP25 micro-positioning stages. Each one controls a single axis of motion, allowing the laser to be scanned in a grid. These stages have active position feedback, and the position is specified as repeatable to $0.2 \mu\text{m}$. For a typical scan, the step size is $4 \mu\text{m}$, which allows the laser to overlap the previous position, but limits the amount of pre-bleaching due to exposure to the low intensity wings of the laser before being illuminated by the full power of the laser (See full discussion of bleaching in Sec. 2.4.2). The stages are controlled by a LabVIEW program that triggers the CCD camera to take an image and records the laser power at each position, then moves the laser to the next position in the grid.

3.4 Fluorescence Collection System

The fluorescence is collected from above the cryostat, as shown in Figure 3.16. A 50 mm camera lens (Nikkor 50MM 1:1.4) is mounted above the cryostat to collimate the fluorescence. An x-y-z translation stage is used to center the lens over the laser spot on the window. A 25.4 mm diameter filter is placed above the lens to block light outside the spectral range of interest. For fluorescence spectroscopy, a 573 nm Raman filter is used to remove laser scatter. For imaging, a sharp-edged bandpass filter centered at 620 nm with a transmission FWHM of 19.3 nm (Semrock FF01-620/14-25) is used. Two flat mirrors transport the beam to a 200 mm camera lens (Nikkor-Q.C. Auto 1:4), which focuses the image onto a liquid nitrogen (LN) cooled CCD camera (Roper Scientific SPEC-10). The pixel size of the CCD is 20 μm . With the 4 \times magnification of the optics and 45 $^\circ$ tilt of the window, each pixel images a 5 μm \times 7 μm area of the window surface.

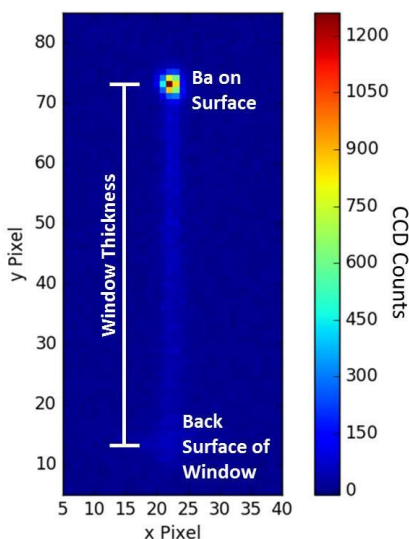


Figure 3.19: A sample image of Ba atoms deposited in SXe on the sapphire window excited by 615 μW of 572 nm laser light. This image was taken without the spectrometer through the 620 nm bandpass filter.

A sample image containing Ba atoms in the laser beam is shown in Figure 3.19. The excitation wavelength was 570 nm and a 620 nm bandpass filter was used to observe the 619 nm fluorescence peak. The spot at the top of the image is the surface of the window facing the ion beam, where the Ba⁺ ions are deposited. The narrow line extending below the Ba spot is the bulk sapphire

emission, with a very low background in the selected wavelength range from Cr^{3+} impurities in the sapphire. The broad spot at the bottom is the back surface of the window. It is somewhat out of focus for both the excitation laser and collection optics, thus it is weak and broad. With the limited resolution of the collection optics, the Ba spot is imaged with an average width of $w = 10.4 \mu\text{m}$.

3.5 Imaging Analysis

Once the images have been taken by the CCD camera, they are analyzed to measure the fluorescence of the Ba atoms. The process for integrating and scaling the fluorescence signals is explained in this section. In the first subsection, the analysis of images with a fixed (non-scanning) laser is discussed. Extending the analysis to create “composite images” of the Ba/SXe sample in the case of a scanned laser experiment is discussed in the second subsection.

A digitizing offset of 100 ± 3 counts per pixel is present in all images obtained by the CCD camera. This offset and any background not associated with the laser was measured by taking 5 images with the same camera parameters as used for data taking with the laser shutter closed. A measurement of this background is done for each experiment day. The average of these “dark frames” is subtracted from every camera image obtained before any data analysis is done.

3.5.1 Fixed Laser Analysis

To obtain the total fluorescence in fixed laser images, an area around the peak laser signal is integrated. This area is selected by looking at each image and determining the center of the Ba fluorescence spot by eye, around which the integration region of specified height and width is chosen. The integration region is drawn onto the image as a box, as in Fig. 3.20 and checked to ensure the area is appropriate. The Ba deposit in (a) has a clear fluorescence spot at the front surface of the window, with the dim line below the spot extending through the bulk of the window being due to the sapphire background. In a SXe-only deposit, (b), the surface background does not produce a clear spot, since it has been effectively bleached out almost entirely. In this case as well as for very low density Ba deposits, the same integration region is used as a recent Ba deposit.

The chosen region is checked using the end of the weak chromium line image from the window bulk. For a given data set, a fixed integration size is used, generally 4×4 pixels. If the peak laser position does not align well to integrate full pixels, the edge pixels are scaled by the fraction of the area inside the integration region for each pixel. A simple example is shown in Fig. 3.21 with the appropriate scale factors. This is done to keep a constant integration size, while not making it so large as to include extraneous background.

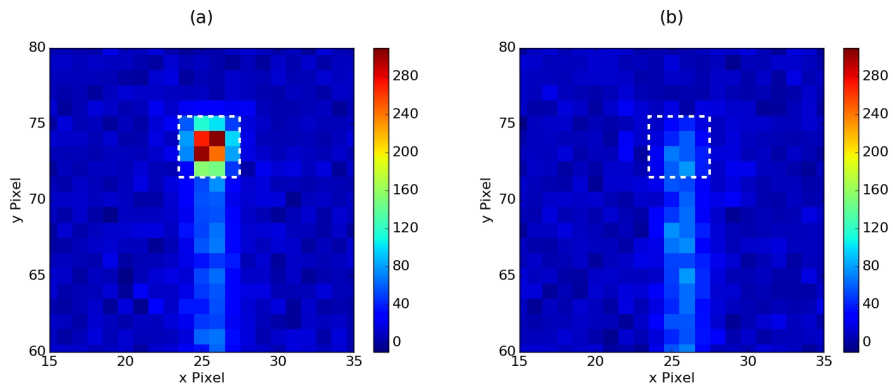


Figure 3.20: Two examples of images used to ensure that the integration region selected is appropriate.

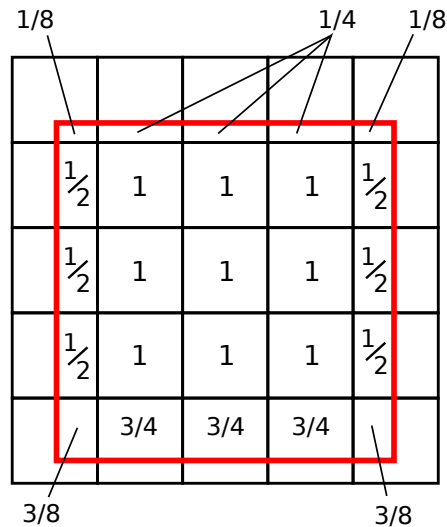


Figure 3.21: When the center and dimensions of the integration region do not align with pixel boundaries, the partial pixels are scaled by the included area fraction. This example shows the fractional contribution of each pixel in the integration area of 4×4 pixels.

Since the laser is gated as described in Sec. 3.7, the laser exposure (power \times time the shutter is open) is not uniform in each image. Thus, each integral is scaled by the laser exposure so that the signals can be compared between images. This is done either by dividing by the actual exposure, or in a “normalized” fashion by dividing the laser exposure by the average laser exposure before scaling the signal. The former is used when measuring the Ba fluorescence response in Sec. 4.1 and is also used in the composite scan images in Sec. 4.2. The use of this scaling is denoted by the use of “counts/mWs” units. The latter is used to correct for relative exposure differences when plotting the absolute counts of successive images, as in the turn-off study in Sec. 4.3.

3.5.2 Scanned Image Analysis

The set of images collected during a scanned laser experiment can be analyzed to create a “composite image” of the scan. These composites are made by integrating the area around the laser position in each CCD image corresponding to a particular laser position in the scan. Since a typical scan is 12×12 positions, selecting each integration region individually is time consuming and may not be accurate. To select the integration regions, the first frame is examined to determine the starting laser position, upon which an integration region is chosen as in the fixed laser images described in the previous section. The integration region center is moved by a fixed step for each frame, following the motion of the laser. As in the previous section, each frame has the integration region plotted on the CCD image to ensure that the initial integration region and step size chosen is correct. The integral for each frame is then associated with the laser position of that frame. Since the laser is rastered, as in Fig. 3.18, when the integrals are plotted to for the composite image, each even numbered row must be reversed to put the laser positions in the correct place. Each integral is scaled by the laser exposure recorded for the individual image. In this way, a fluorescence image of the surface can be created, and individual atoms resolved.

3.6 Laser Spot Size Determination

The size of the focused laser used to excite the Ba atoms is an important parameter used in calculations such as fluorescence efficiency and Ba ensemble fluorescence rate. The width of the laser at the focusing lens was measured, and ray matrix analysis was used to calculate the Gaussian beam waist, assuming a $TEM_{0,0}$ transverse mode. This is discussed in Sec. 3.6.1 If there is any imperfection in the laser mode or scattering of the laser as it passes through the sapphire window surfaces and the SXe layers frozen onto them, the actual beam may be wider than this ideal prediction. Since the resolution of the CCD camera is larger than the estimated spot size of the laser, the laser width cannot be measured by fitting a Gaussian to an image of the laser on the window. The method used to estimate the laser spot size from the composite scan images of individual Ba atoms is discussed in Sec. 3.6.2.

3.6.1 Ray Matrix Calculation

Ray matrices were used to calculate the beam waist in vacuum after it exits the surface of the sapphire window where the Ba/SXe layer is deposited. Since the SXe layer is very thin ($< 1 \mu\text{m}$), it does not significantly change the spot size of the beam, and is not used in the calculation. The initial conditions assume a collimated input laser, and the spot size was measured at the lens. The error function fits to a scanned razor-blade profile at the lens are shown in Fig. 3.22, with the resulting spot sizes of $3.36 \pm 0.07 \text{ mm}$ in the x-direction and $3.80 \pm 0.03 \text{ mm}$ in the y-direction.

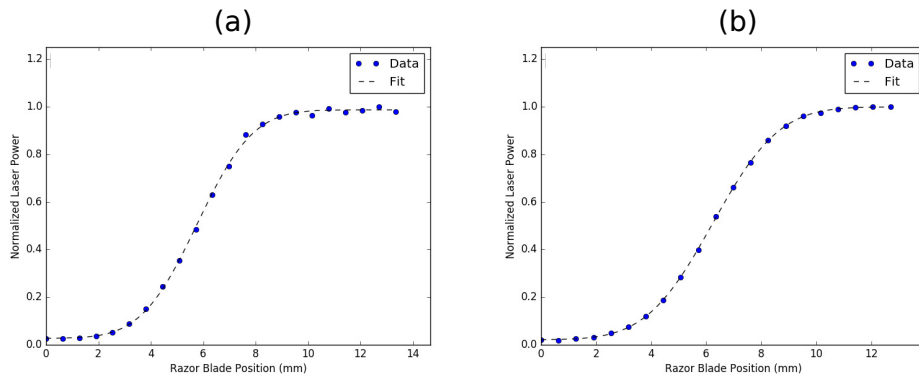


Figure 3.22: Fits to power profiles in the x-direction (a) and y-direction (b) taken by moving a razor blade across the laser beam.

The optical components in the ray matrix calculations are shown in Fig. 3.23. The laser passes through three windows, two of which are tilted in one of the transverse directions. The ray matrices for both tangential (W_t) and sagittal (W_s) planes for a prism are derived by J.-P. Taché [85]. The tangential plane is defined as the plane containing the optical axis where the incident ray makes a non-right angle with the surface. The sagittal plane is defined as the plane containing the optical axis where the incident ray is at a right angle to the surface. For the sapphire window, the y-z and x-z planes are the tangential and sagittal axes respectively. A window is the special case where the prism surfaces are parallel, and these ray matrices are given in Eq. 3.12:

$$W_t = \begin{pmatrix} 1 & \frac{L \cos^2(\theta)}{n \cos^2(\phi)} \\ 0 & 1 \end{pmatrix} \quad W_s = \begin{pmatrix} 1 & \frac{L}{n} \\ 0 & 1 \end{pmatrix} \quad L = \frac{T}{\cos(\phi)} \quad (3.12)$$

Here, T is the thickness of the window, L is the path length through the window, and n is the index of refraction of the window. The angles θ and ϕ are the incident and refracted angles of the ray. The full matrix including all of the components is shown below, and the relevant quantities for the matrices are summarized in Table 3.7. The matrices are multiplied first on the right and the last on the left.

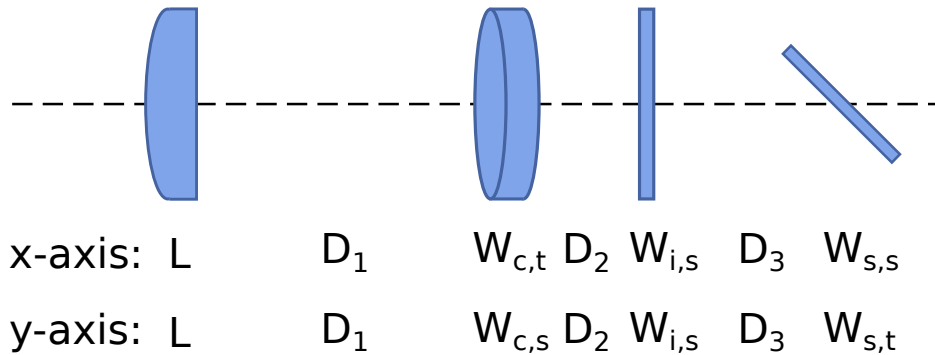


Figure 3.23: Optical components in the ray matrix calculation of the laser beam waist and their associated matrices. The window matrices are labeled for which window it is and which plane it is in. The windows are labeled c: compensator, i: cryostat input, s: sapphire. The window planes are labeled t: tangential, s: sagittal.

$$\begin{aligned}
M_x &= \begin{pmatrix} 1 & \frac{L_s}{n_s} \\ 0 & 1 \end{pmatrix} \begin{pmatrix} 1 & d_3 \\ 0 & 1 \end{pmatrix} \begin{pmatrix} 1 & \frac{L_i}{n_g} \\ 0 & 1 \end{pmatrix} \begin{pmatrix} 1 & d_2 \\ 0 & 1 \end{pmatrix} \begin{pmatrix} 1 & \frac{L_c \cos^2(\theta_c)}{n_g \cos^2(\phi_c)} \\ 0 & 1 \end{pmatrix} \begin{pmatrix} 1 & d_1 \\ 0 & 1 \end{pmatrix} \begin{pmatrix} 1 & 0 \\ -\frac{1}{f} & 1 \end{pmatrix} \\
M_x &= \begin{pmatrix} 1 - \frac{1}{f}(L_{tot} + \frac{L_c \cos^2(\theta_c)}{n_g \cos^2(\phi_c)}) & L_{tot} + \frac{L_c \cos^2(\theta_c)}{n_g \cos^2(\phi_c)} \\ -\frac{1}{f} & 1 \end{pmatrix} \quad L_{tot} = d_1 + d_2 + d_3 + \frac{L_s}{n_s} + \frac{L_i}{n_g} \\
M_y &= \begin{pmatrix} 1 & \frac{L_s \cos^2(\theta_s)}{n_s \cos^2(\phi_s)} \\ 0 & 1 \end{pmatrix} \begin{pmatrix} 1 & d_3 \\ 0 & 1 \end{pmatrix} \begin{pmatrix} 1 & \frac{L_i}{n_g} \\ 0 & 1 \end{pmatrix} \begin{pmatrix} 1 & d_2 \\ 0 & 1 \end{pmatrix} \begin{pmatrix} 1 & \frac{L_c}{n_g} \\ 0 & 1 \end{pmatrix} \begin{pmatrix} 1 & d_1 \\ 0 & 1 \end{pmatrix} \begin{pmatrix} 1 & 0 \\ -\frac{1}{f} & 1 \end{pmatrix} \\
M_y &= \begin{pmatrix} 1 - \frac{1}{f}(L_{tot} + \frac{L_c \cos^2(\theta_s)}{n_g \cos^2(\phi_s)}) & L_{tot} + \frac{L_c \cos^2(\theta_s)}{n_g \cos^2(\phi_s)} \\ -\frac{1}{f} & 1 \end{pmatrix} \quad L_{tot} = d_1 + d_2 + d_3 + \frac{L_i}{n_g} + \frac{L_c}{n_c}
\end{aligned}$$

Table 3.7: Table of the quantities used in the ray matrix calculation. These are the final values that simultaneously minimize the final spot size in both dimensions.

Symbol	Definition	Value
f	Focal length of asphere lens	7.90 cm
$d_{1,2,3}$	Distances in air/vacuum between components	68.44 cm (sum)
n_s	Index of refraction for sapphire	1.77
n_g	Index of refraction for glass	1.50
L_s	Path length in sapphire window	0.55 mm
θ_s	Angle of incidence on sapphire window	45°
ϕ_s	Angle of refraction in sapphire window	23.5°
L_c	Path length in compensator	12.58 mm
θ_c	Angle of incidence on compensator	9.5°
ϕ_c	Angle of refraction in compensator	6.3°
L_i	Path length in cryostat input window	3.00 mm
L_{tot}	Total path length from lens to focus	70.74 mm

To find the beam waist as measured after exiting the sapphire window, the quantity d_1 was varied to find a minimum value of w_x and w_y . This can be pictured physically as moving the lens along the z-axis until the beam is focused immediately after leaving the sapphire window. Simultaneously, the angle of the astigmatism compensator was varied until the minimum spot sizes

occurred for the same d_1 . The waists in the horizontal (x) and vertical (y) axes were calculated to be $w_{ox} = 3.22 \mu\text{m}$ and $w_{oy} = 2.85 \mu\text{m}$. These waists are defined as perpendicular optical axis of the laser. After the laser exits the sapphire window, it points horizontally in the same direction as when it enters the lens (i.e. the translations of the x and y axes are the same as the motion of the lens on the stages). Given that the window is tilted at 45° , w_y will be larger by a factor of $\sqrt{2}$ in the plane of the sapphire window surface, and thus in the plane of the Ba deposit. Since there is no tilt relative to the x direction, w_x is unaffected. The “effective size” of the laser relative to the Ba deposit is therefore $w_{sx} = 3.22 \mu\text{m}$ and $w_{sy} = 4.03 \mu\text{m}$, where the “s” subscript refers to the surface spot sizes.

3.6.2 Gaussian Fit to Composite Images

In the composite scan images of widely separated atoms, the fluorescence is proportional to the laser intensity experienced by the atom. Thus the signal from each laser position can be treated as a measurement of the laser intensity at the position of the atom, assuming that the laser and the window do not move. The composite image is therefore an image of the laser intensity in a grid. By fitting a 2D-Gaussian, Eq. 3.13, to a Ba peak in the composite images, the spot size of the laser in the SXe can be estimated.

$$f(x, y) = A e^{-\frac{2(x-x_o)^2}{w_x^2}} e^{-\frac{2(y-y_o)^2}{w_y^2}} + B \quad (3.13)$$

The fit parameters in Eq. 3.13 are the amplitude, A, the center location (x_o, y_o) , $1/e^2$ spot sizes (w_x and w_y), and a uniform offset, B. Once the widths are extracted in units of “scan steps”, they are multiplied by the step size of the scan to obtain the widths in microns. In this situation, the step size in the y-direction in the image is defined as the same the step size of the lens, which is $4 \mu\text{m}$ in both directions. The fits were done on images of two Ba atoms taken on 11 May 2018 (see Sec. 4.2), each of which was scanned twice. The best-fit widths and uncertainties are given in Table 3.8. The weighted average of the widths are $w_{ox} = 5.73 \mu\text{m}$ and $w_{oy} = 6.62 \mu\text{m}$, which corresponds to $w_y = 9.36 \mu\text{m}$ in the plane of the Ba atoms. These measured widths are significantly larger than

the calculated ideal focusing, $w_x = 3.22 \mu\text{m}$ and $w_y = 2.85 \mu\text{m}$, and is likely due to scattering in the SXe layers on both window surfaces. An example of the fit is compared to the data in Fig. 3.24, showing good agreement.

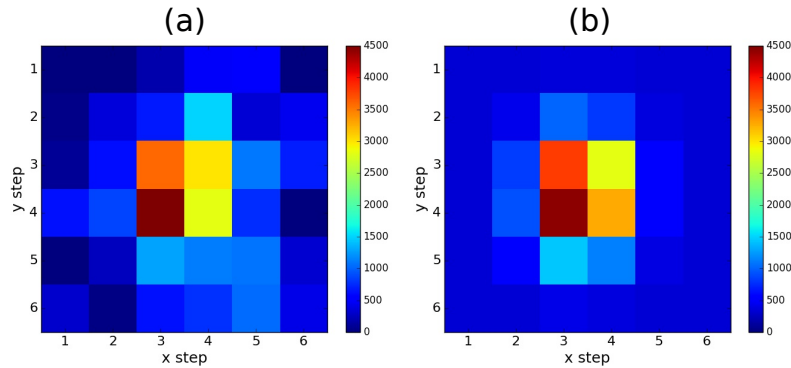


Figure 3.24: The data (a) and fit using the direct Gaussian method (b) for Scan 1 – Atom A of 11 May 2018 are plotted.

Table 3.8: Summary of the best-fit values for the laser widths. Scans “1” and “2” are shown in Results (Chap. 4) in Figs. 4.5 (b) and (c) respectively. Atoms “A” and “B” are the left and right atoms in these scans respectively.

	w_x	w_y
Atom A – Scan 1	5.31 ± 0.60	6.58 ± 0.60
Atom B – Scan 1	5.54 ± 0.52	6.79 ± 0.76
Atom A – Scan 2	6.42 ± 0.48	6.92 ± 0.55
Atom B – Scan 2	5.55 ± 0.48	5.78 ± 1.15
Weighted Average	5.73 ± 0.26	6.62 ± 0.40

3.7 Cryostat Vibration Compensation

The helium cryostat uses a Gifford-McMahon cycle to cool the sapphire window. This relies on a compressor to supply the high pressure helium that expands in the cold finger providing the cooling power. This cryostat uses the differential pressure of the helium to drive the displacer in the cryostat cold head. The pulses of high pressure helium moving the displacer in the cryostat

cause the cold finger to vibrate, moving the window relative to the laser beam. The effect of this vibration on the measurement of Ba fluorescence needs to be considered. If there were no vibration, the laser would simply illuminate the atoms in the focus area. As the window moves relative to the laser, different atoms are illuminated, though only those in the focus area are being excited at any moment in time. This means for larger Ba deposits that a larger number of individual atoms are contributing to the fluorescence signal, and each atom is illuminated for less time. This reduces the bleaching effect of prolonged exposure to laser excitation. In a composite image of a single atom, this vibration broadens the single Ba peak.

To mitigate the effect of cryostat vibration, laser gating is used. A shutter synchronized to the vibration of the cryostat passes the laser only when the window is in a specific place. Thus, the laser only illuminates the atoms in that spot on the window. To measure the vibration, a piezoelectric sensor (DENSO 89615-50010) is threaded into an aluminum mount bolted to the support structure of the cryostat cold head, and the signal is processed by the circuit shown in Figure 3.25. This

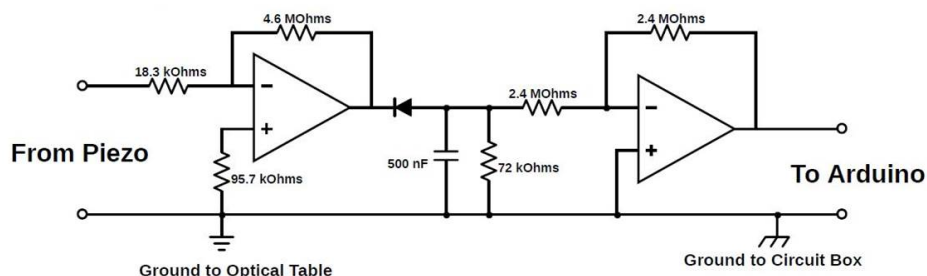


Figure 3.25: Circuit for processing the piezo-accelerometer’s signal to create a waveform that can be used for triggering the laser shutter.

circuit amplifies, rectifies and smooths the accelerometer signal to provide a reliable trigger pulse. The first op-amp is used in an inverting amplifier. The signal is half-wave rectified by the diode, and is smoothed by the RC path to ground. The second op-amp is used in a unity gain inverting amplifier to create a positive slope for triggering.

The waveform for one period of the processed signal is shown in Figure 3.26. The period is 417 ms, with one tall peak and one short peak per cycle. An Arduino micro-computer was

programmed to trigger on the large peak, and control the Melles-Griot No. 3 synchro-electronic shutter referred to as the “laser shutter” in Sec. 3.3. The program uses two parameters to adjust the timing of the laser shutter gating, a delay time and an open time. The delay time is the time between the trigger on the large pulse and the signal to open the shutter, and the hold time is how long the shutter is held open by the control signal.

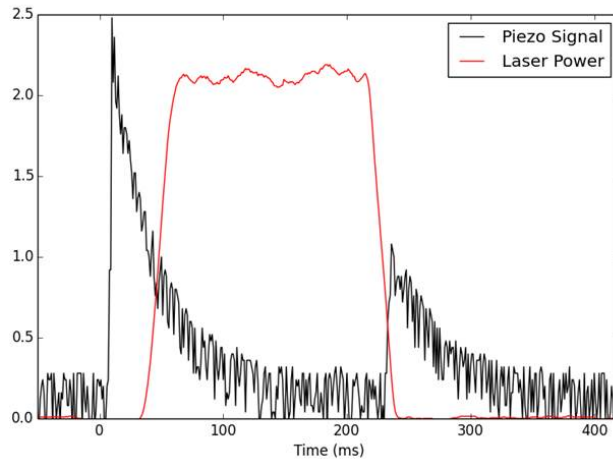


Figure 3.26: The processed signal from the piezoelectric vibration sensor (black) and laser power (red, arbitrary scale) are plotted over one period of cryostat vibration. The gating program was set to a 0 ms delay and 200 ms open time. Due to delays in the shutter electronics, the laser is on the sample from 50 ms - 220ms (FWHM).

To find the optimal gating parameters, a highly scattering dust spot, which is fixed on the sapphire window, was illuminated with a broad laser beam and tracked as the cryostat vibrates. The CCD camera recorded many 50 ms images for different delay times with the laser shutter held open for 100 ms in all cases. The camera and the laser shutter were not synchronized, thus the camera randomly sampled the location of the spot during the time the laser shutter was open. For each delay time, the location of the dust spot in each image was determined by fitting a 2D Gaussian. Since the delay time between the trigger pulse and the laser shutter opening is set for this data, the phase of the dust spot location relative to the trigger pulse is known.

To track the motion of the dust spot with better time resolution through the whole cycle, 50 ms CCD images were taken without the laser being gated, and a 2D Gaussian was fit to each image to

determine the location of the dust spot. The time of the middle of each frame was calculated and then adjusted by N times the 417 ms period of the cryostat cycle. That is, the cryostat vibration period was subtracted until the time was less than the period (Eq. 3.14), giving the image's time relative to the cryostat cycle,

$$t' = t - (\text{Int}(t/T) \times T) \quad (3.14)$$

Here, t is the time of the image relative to the start of the first image and T is the period of the cryostat cycle. All the dust spot fit x and y positions are plotted as a function of t' , in Fig. 3.27 (a) and (b) respectively. To obtain the start time of the first frame of these images relative to the cryostat cycle, the location of the dust spot in the first frame was compared to the average position of the dust spot in the gated images of known delay time. The dust spot position in the first frame best matches the average position of the dust spot in the time gate centered 75 ms after the trigger signal. The center time of the first frame of un-gated images was therefore advanced to $t = 75$ ms before the frame times were converted to t' . Since $t = t' = 75$ ms for the first frame, $t' = 0$ corresponds to the time of the trigger pulse.

The x, y positions of the data from Fig. 3.27 (a) and (b) are plotted in Fig. 3.27 (c), showing the 2D motion of the window through the cryostat cycle. The motion of the dust spot is generally sinusoidal in both directions, with the exception of the small kink at ~ 300 ms in the y motion. The x motion has a larger magnitude, and corresponds to the axis of motion of the displacer that moves inside the cold head. The first turning point of the motion is at ~ 100 ms, thus the laser position is fairly stable from $t' = 0$ ms to $t' = 200$ ms. The x and y positions of the dust spot during this time span both have a standard deviation of $1.2 \mu\text{m}$.

Fig. 3.28 (a), shows the laser coverage without gating, simulated by placing a 2D Gaussian of unit amplitude and widths $w_x = 3.22 \mu\text{m}$ and $w_y = 4.03 \mu\text{m}$, which represent the laser spot size in the plane of the window, at each dust spot location from the data shown in Fig. 3.27 (a) and (b). The 2D motion shows the window to oscillate between two poles located at about (5,5) and (15,3.5). The large value of the laser intensity at the poles of the motion compared to the axis between them indicates that the spot transitions quickly between the two poles. This is consistent

with the sinusoidal motion observed in Fig. 3.27. Since the motion of the window at the turning points is small compared to the spot size of the laser, there is minimal broadening of the laser intensity at the poles of the oscillation. Gating the laser to select either pole is therefore suitable to minimize the effect of the cryostat vibration.

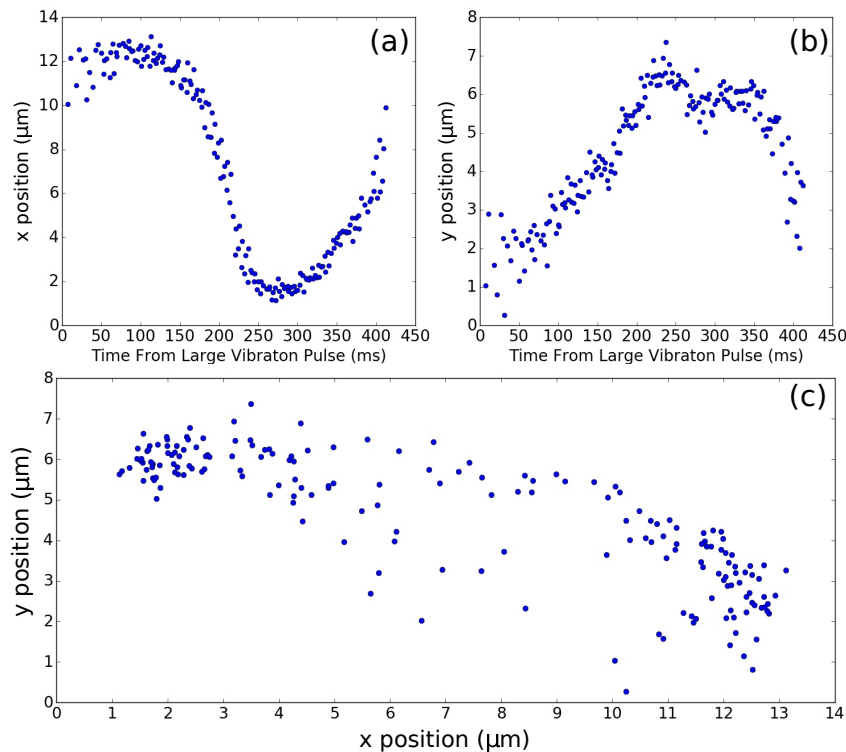


Figure 3.27: The location of the dust spot plotted through one cycle of the cryostat vibration, where 0 ms corresponds to the trigger on the large peak of the vibration signal. The x and y positions are shown in (a) and (b) respectively, and these x,y positions are shown in 2D in (c).

The best gating scheme minimizes the cryostat motion when the shutter is open while keeping a reasonable duty cycle. Since the window is fairly stationary at the right pole, the hold time was increased to improve the duty cycle as much as possible without adding much motion of the window. The settings that are used are a 0 ms delay and 200 ms hold time, and the laser transmission for this gating is plotted with the vibration sensor signal in Fig. 3.26. This choice of parameters was tested by taking 50 ms exposures with the laser gated, and compared to the data without laser gating shown in Fig. 3.27. The laser coverage for the gated laser data was simulated,

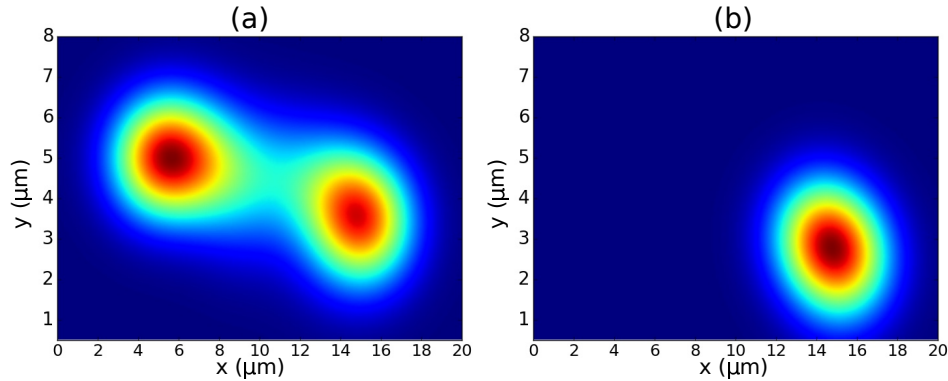


Figure 3.28: The laser coverage for the un-gated (a) and chosen gating of 0 ms delay and 200 ms hold (b).

and is shown in Fig. 3.28 (b), along with the un-gated coverage (a). Comparing the two shows these gating parameters select the lower-right pole of the vibration pattern as expected from the timing information in Fig. 3.27. This technique has been successful in minimizing the effect of the cryostat vibration, and achieves a 45% duty cycle.

3.7.1 Sapphire Background Reduction by Pre-Bleaching

The main background that can interfere with the measurement of the Ba fluorescence comes from the sapphire window used as a substrate for deposition of the Ba/SXe samples. An image of a SXe-only deposit is shown in Fig. 3.29. The spot at the top of the image is the background emitted from the front surface of the sapphire window. The blurred spot at the bottom of the image is the background from the back surface. The blurriness of the bottom spot arises from both the laser and collection optics being out of focus at the back surface. The thin line connecting the two spots is the weak Cr^{3+} emission from the sapphire bulk. This background is reduced by using low- Cr^{3+} impurity sapphire windows. This impurity occurs in sapphire at the ppt level, and produces the well known sharp line at 693 nm [86], as well as a weak broad background extending into the spectral region of interest for Ba emission around the 619 nm fluorescence line [49]. The tilt of the vertical sapphire bulk line is a result of the alignment of the imaging optics not providing an exact 90° rotation.

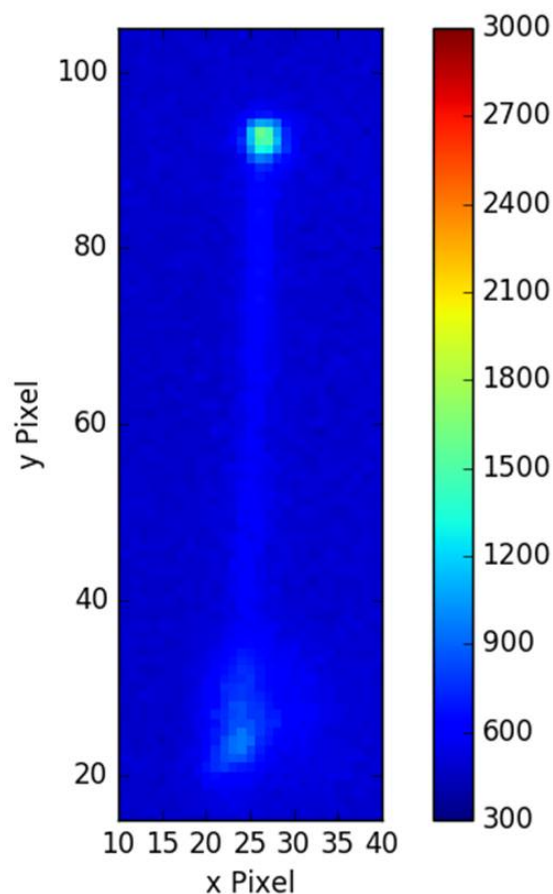


Figure 3.29: CCD image of a SXe-only deposit.

The surface background has been shown to photo-bleach when exposed to laser light in the visible range [49]. Many wavelengths have been used for bleaching, including 514.5 nm, 532 nm, 570-572 nm, and 580.5 nm. The background is reduced in preparation for Ba imaging by pre-bleaching the surface of the window at 100 K with an 80 mW 532 nm laser. This laser is sent along the same beam path as the excitation laser using a dichroic mirror and is focused through the same optics as the excitation laser. The focusing lens position along the optical axis is adjusted until the scatter from the window surface appears focused in the CCD image. Due to the smaller spot size on the focusing lens, the pre-bleaching laser is focused to a calculated minimum spot size of $\sim 8 \mu\text{m}$. For both the fixed and scanned images, the bleaching laser is repeatedly rastered across an area larger than the area of the observation region typically overnight ($\sim 16 - 24$ hours).

A composite image of the bleached “hole” with a SXe-only deposit is shown in Figure 3.30. The bleaching laser was scanned in a typical 14×14 grid with a step size of $8 \mu\text{m}$ with a total exposure time of 7 min per spot. This results in a background reduction of about a factor of 30 in an area of approximately $90 \times 90 \mu\text{m}$. The composite image was taken with 1.5 s of $\sim 48 \mu\text{W}$ of 570 nm laser exposure, using a 15×15 grid with step size $12 \mu\text{m}$ to cover the entire bleached area and the un-bleached background for comparison. For the composite image, the integration region for each image was expanded to 6×6 pixels to accommodate the de-focusing of the laser at the top and bottom of the scan area. The average background in the center $92 \times 92 \mu\text{m}$ (8×8 scan steps) of the bleached area is 746 counts/mWs, with a standard deviation of $\sigma = 347$ counts/mWs using a 4×4 integration region for comparison to experimental conditions. The laser is sufficiently focused in this region for the smaller integration size to capture the entire laser spot. This pre-bleaching procedure has been successful in providing the low, uniform background required for the single atom signal to be significantly above this background in an area larger than is typically scanned.

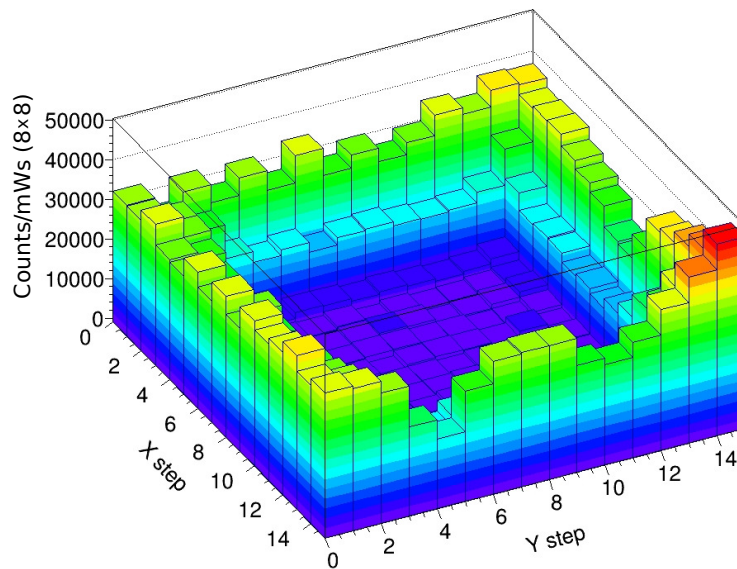


Figure 3.30: A raster scan composite image of the sapphire surface emission taken through the 619 nm band-pass filter is shown.

Some sapphire windows that were tested were chemically etched on the surface. The etching was carried out by collaborators at Stanford University. A solution of piranha acid (mix of sulfuric acid and hydrogen peroxide) was applied to both used and new sapphire windows, then the windows were washed with deionized water and blown dry with nitrogen gas. Using X-ray photoelectron spectroscopy (XPS) also conducted at Stanford, the surface of the un-etched windows was found to contain predominantly carbon, hydrogen and oxygen atoms. After the acid treatment, the surface more closely resembled the 40/60 aluminum/oxygen composition of sapphire. This indicates that some surface contamination was removed. The windows prepared in this way showed a lower initial surface background than the un-treated windows. After photo-bleaching, the background was not found to be significantly lower with the etched windows than the un-etched ones.

Chapter 4

Results

Three principal results are presented in this chapter. (1) Fluorescence at 619 nm from Ba atoms was imaged using a focused laser beam at a fixed position at densities ranging over 5 - 700 ions per observation region. This is discussed in Sec. 4.1. This study demonstrates the linear response of the fluorescence with respect to the number of atoms observed, and establishes an expected fluorescence signal level per atom normalized by laser power and observation time. (2) The focused laser was scanned across a Ba/SXe sample with a much lower Ba atom density to resolve individual Ba atoms within the scan region. This is discussed in Sec. 4.2. The capability to observe individual Ba atoms in an area of a SXe sample is a crucial step towards a practical Ba tagging technique for nEXO. This study also allows for an estimation of the fluorescence rate and quantum efficiency to be made. (3) After identification of a Ba atom peak in a scan, the laser was moved to the Ba location and the atom was observed to determine the behavior of the fluorescence over time. This is presented in Sec. 4.3.

4.1 Imaging of Ba Atoms with a Fixed Laser

Observation of Ba atoms down to the single atom level in a fixed, i.e. not rastered, laser beam via the 619 nm emission line have been presented in a previous dissertation [49]. This technique has been improved in several ways to increase the precision of the measurement.

The stability of the ion beam used as the source of Ba has been improved and as such, the measurement precision of the ion current has been improved. The entire beam line was cleaned and re-aligned using a diode laser mounted in place of the source. This process has allowed the ion beam to be run with fewer ion steering elements active, resulting in more reliable operation over the course of a data-taking run. This has reduced the shot-to-shot uncertainty of the beam significantly. Two additional Faraday cups have also been installed, cups 2 and 4. Faraday cup 2 is used with cup 1 to ensure the beam passes on-axis through the aperture leading to the final focusing lens (LD).

Cup 4 is used in tandem with cup 3 to ensure the beam is still on-axis immediately upstream of the sample, improving the coaxial alignment of the ion deposit and laser spot. Cup 4 is also used to measure the ion pulse charge for each deposit, and the ion density on the window is calibrated to cup 4 (details in Sec. 3.1.6).

To obtain more data in fixed laser beam studies, the scanning stages were used to sample four locations of each deposit, separated horizontally by 20 μm . This distance is large compared to the laser spot size (3.5 - 6.2 μm average), thus the measurements are independent of each other. The signals from the 4 locations were averaged and a standard deviation calculated for each deposit. This provides a more accurate value for the fluorescence observed than data taken at only one location, as in [49], and allows for an estimation of the uncertainty in the fluorescence rate.

The background was measured by taking images of SXe-only deposits regularly throughout the experiment. These background images were taken every third deposit. That is, a SXe-only deposit is made, followed by two Ba deposits of different densities, then another SXe-only deposit is made. Each sample is evaporated at 100 K before the next deposit is made. The background for the two Ba deposits is determined by averaging the SXe-only runs before and after the Ba deposit. This accounts for any small drift in the background level throughout the experiment. To ensure each Ba deposit has two SXe-only runs to estimate the background, the first and last deposits of any experiment series are SXe-only.

As discussed in Sec. 3.2, a Ba^+ ion beam is used as the source of Ba, co-deposited with Xe gas to create a sample of Ba atoms isolated in SXe after some neutralization of the ions occurs. The observed fluorescence counts as a function of Ba^+ ion density is plotted in Fig. 4.1 on a linear (a) and log-log (b) scale. Each point is the average of the integrated fluorescence signal in the four spots observed, and the error bars are the standard deviation. The counts recorded by the CCD camera were scaled by the power and exposure time to account for differences in these values between observations. The average laser power used was 19 μW , and the average exposure time was 4.3 s, with a focus area of 19.1 μm^2 . Details on the process of integrating and scaling the data by exposure are given in Sec. 3.5.1. The SXe-only background has been

subtracted from this data to obtain the Ba atom fluorescence. A linear fit performed on the data yields a fluorescence rate per ion deposited in the laser beam area of 284 ± 11 counts/mWs per ion. When the uncertainty in the ion density is taken into account per Sec. 3.1.6, the observed fluorescence rate is 284^{+57}_{-85} counts/mWs per ion. This is a lower limit on the fluorescence rate of Ba atoms, since there are two efficiencies to consider when converting from ions deposited to fluorescing atoms. The first is the neutralization efficiency of the ions when they are deposited in the SXe layer, and the second is the fraction of atoms in the single vacancy site that will emit the 619 nm fluorescence being observed. Thus, the number of fluorescing atoms will be less than or equal to the number of ions deposited, meaning the fluorescence rate per atom in this matrix site is higher than the rate measured by the fit to the data in Fig. 4.1 (a). The fluorescence rate is expected to be linear with ions deposited if Ba atoms are responsible for the emission observed. If the source of the 619 nm emission was a barium dimer (Ba_2), the rate would vary quadratically with ion density. The slope of a power law fit to the data in Fig. 4.1 gives 1.04 ± 0.05 , which is consistent with a linear relationship. This is confirming evidence that the 619 nm fluorescence is due to Ba atoms.

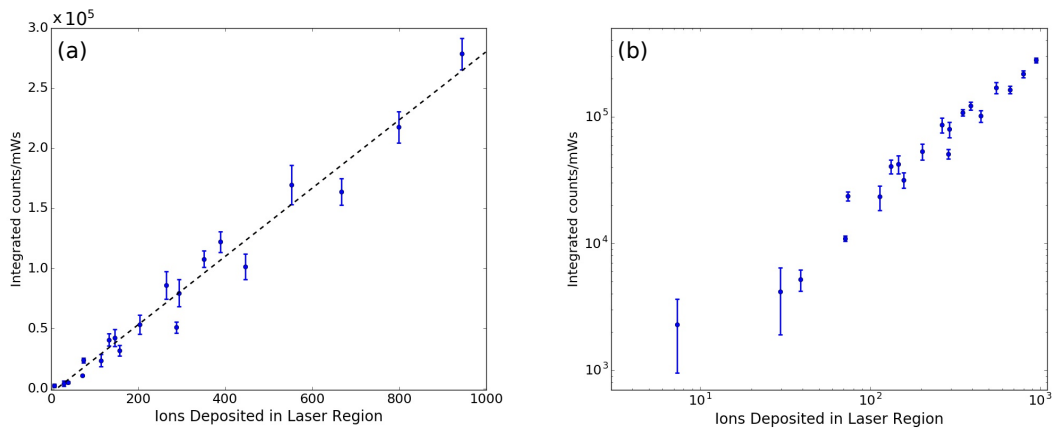


Figure 4.1: The 619 nm Ba fluoresce signal vs. the number of ions in the laser region is plotted on linear (a) and log-log (b) scales with the SXe-only background subtracted. The CCD counts have been scaled by the laser exposure (power \times time), which is on average $83 \mu\text{W s}$ for the data here. The points in each plot are the average value and the error bars are the standard deviation of the four positions measured. The dashed line in (a) is a linear fit of the data, with a slope of 284 ± 11 (1σ) counts/mWs per ion. A power law fit to the data has a slope of 1.04 ± 0.05 (1σ).

This data was also used to investigate the effectiveness of sample evaporation to remove Ba from the sample, i.e. the degree to which each deposit can be treated as independent of the “history” of previous deposits. This property is required for a future nEXO probe, since each Ba tag also must not have any signal from previous tag attempts. To measure any residual Ba fluorescence, the difference in background between the last SXe-only deposit before and the SXe-only deposit immediately after a Ba deposit was calculated. In Fig. 4.2, the differences are plotted vs. the number of ions deposited in the Ba run immediately before the later SXe-only deposit. The points in this plot are the average of the four spots imaged, and the error bars are the standard deviation. If some observable Ba is being left behind, there will be an increase in the fluorescence observed as a function of much Ba was deposited. A linear fit was done to the data and the slope is found to be 0.04 ± 0.43 counts/mWs per ion. This is consistent with zero, verifying that little or no Ba is being left behind. To set a limit on the amount of residual Ba, the maximum slope of the linear fit line divided by the minimum value of the measured fluorescence rate, 284 ± 11 counts/mWs per ion, gives a fractional limit of $\leq 0.16\%$ residual barium remaining in the next deposit on the sapphire window after evaporation.

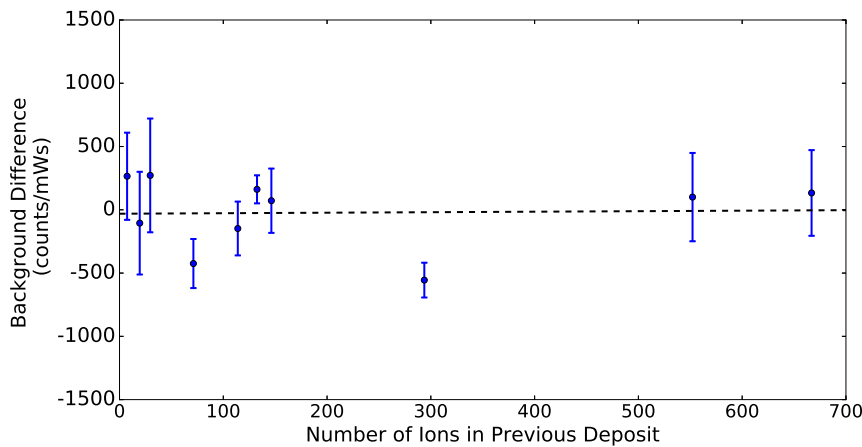


Figure 4.2: The difference in the last SXe-only deposit before and the SXe-only deposit immediately following a Ba⁺ ions deposited. The fit has a slope of 0.04 ± 0.43 counts/mWs per ion, and is shown as the dashed black line.

4.2 Imaging of Ba Atoms with a Scanned Laser

To obtain images of single Ba atoms in the SXe deposit, the scanning stages were used to move the laser in a grid pattern across the sample. To ensure widely separated resonant Ba atoms, the Ba⁺ ion density deposited was reduced by $\sim 10\times$ from the minimum density used in the fixed laser experiments to about 2×10^{-2} ions/ μm^2 . This gives the ions an average spacing of ~ 7 μm . Since it turns out that a small percentage of the ions deposited neutralize to atoms in the SV site we are probing, the spacing of observable atoms is much larger, with low probability of overlap of atoms in one laser area.

The scan pattern was a 12×12 grid with the laser lens moved in steps of 4 μm in both the x and y directions. Due to the 45° tilt of the sapphire window, the step size in the plane of the Ba deposit is 4.0 μm in x and 5.7 μm in y. Each camera exposure was 7 s, which is about 3 s of laser exposure due to the gating of the laser. Including the 800 ms readout time per frame of the camera, each scan takes 19 min to complete. In general, several scans are done for a deposit, which means the sample may be held at 10 K for up to an hour. These scan parameters are used in all the scanning data presented in this work.

The background is measured by taking scans of SXe-only deposits with the same parameters as the Ba scans. Since the process of scanning is more time consuming, fewer SXe-only backgrounds are taken than in the fixed laser experiments. A SXe-only scan was taken at the beginning and at the end of the experimental run.

Four frames of a Ba scan are shown in Fig. 4.3. A digitizing offset of 99 ± 3 counts per pixel has been subtracted per Sec. 3.5. Each of the four images are of subsequent laser positions moving left-to-right across the sample. In the first image (a), the laser is not illuminating the atom, and thus the signal is at background level. In the second image (b), the laser is nearly centered on the position of a Ba atom, and a large Ba fluorescence signal is observed. In the third image (c), the laser has moved away from the position of the atom, but is still illuminating it with the wings of the laser spot. Diminished but distinguishable fluorescence signal is still observed from the Ba

atom. In the fourth image (d), the laser has moved completely away from the atom, and the signal is again at background level.

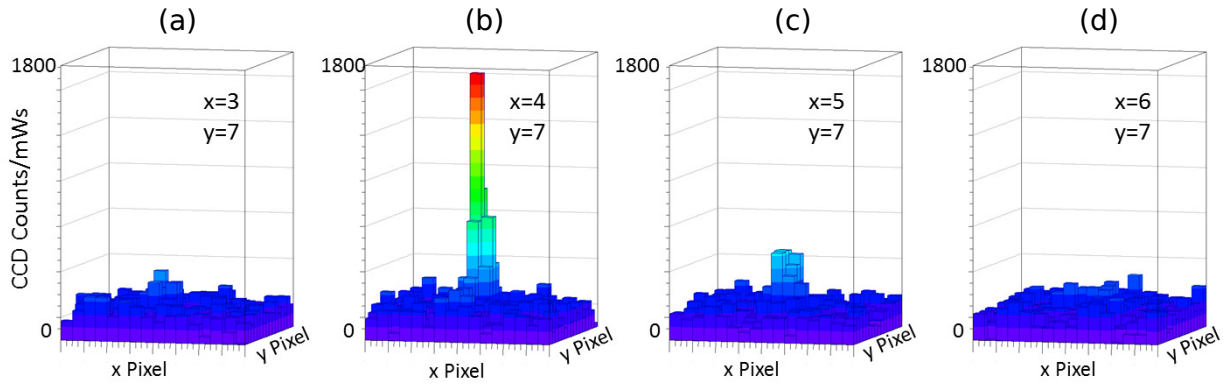


Figure 4.3: Four sequential images from the scan of a Ba/SXe deposit. The laser moves from left to right in the series of images. The coordinates in each image indicate the position in steps in the composite scan.

The four frames of the scan closest to the Ba atom are shown in Fig. 4.4. It is observed that the brightest fluorescence in each image is in pixel $(x,y) = (34,28)$, despite the laser being in a different location for each image. This confirms that this is a single atom “in” this pixel position, i.e. in that $5 \mu\text{m} \times 7 \mu\text{m}$ area of the sample. The sum of the images in Fig. 4.4 (e) shows a tight image of fluorescence peaking in that pixel.

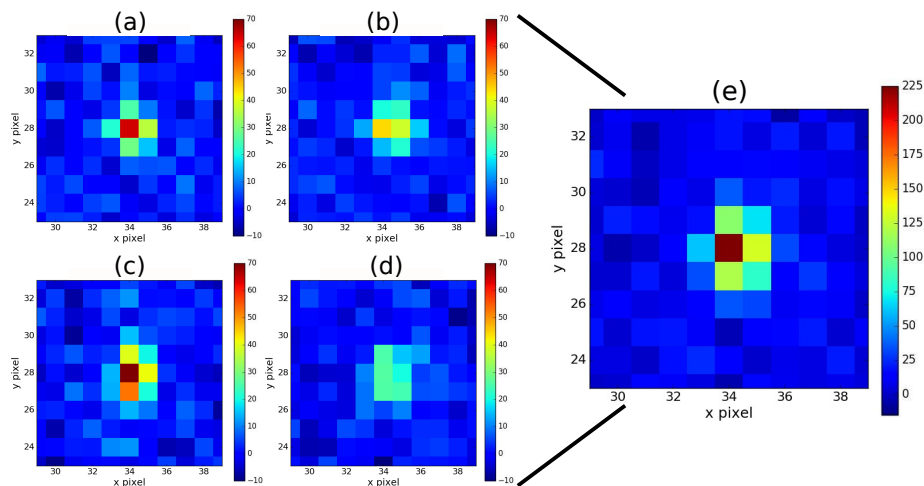


Figure 4.4: Four images of fluorescence from a Ba atom are shown (a) - (d). In each image, pixel $(x,y) = (34,28)$ is the brightest, despite each image having a different laser location. These four images are summed in (e), showing a tight fluorescence spot coming from this pixel.

The composite images of four scans, created as discussed in Sec. 3.5.2, using 4×4 integration regions are shown in Fig. 4.5. The first scan (a) is of a SXe-only deposit. It has a low and fairly uniform background level. The second scan (b) is of a Ba/SXe deposit with 63_{-19}^{+13} Ba⁺ ions deposited in the scanned region. This composite images shows two strong peaks due to Ba atom fluorescence of similar strengths. The images in Figs. 4.3 and 4.4 are from the left Ba peak in this scan. A second scan (c) of this deposit was done immediately following the scan in (b). The peaks present in the first scan persist in the same locations, and with similar heights in counts/mWs. The last scan of the series (d) is of another SXe-only deposit made at the end of the experimental run. It is similar to (a), indicating that the background did not change much throughout the experiment.

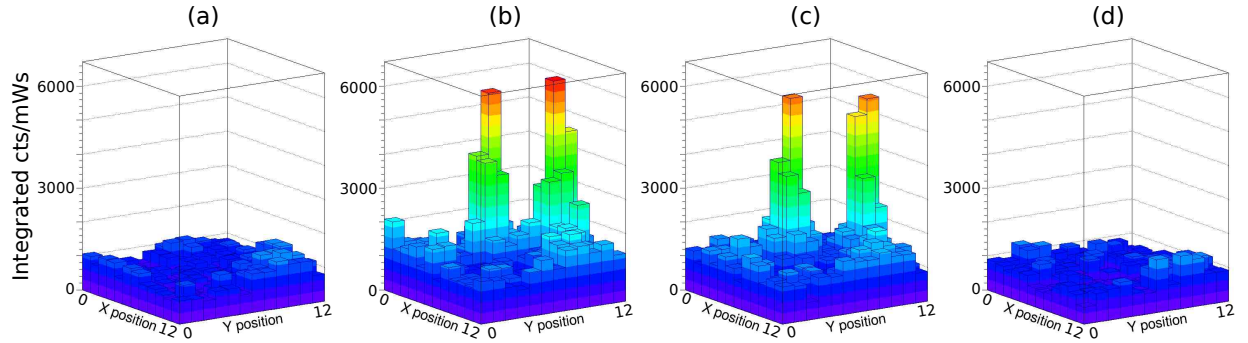


Figure 4.5: Composite images without backgrounds subtracted of three deposits are shown. A SXe-only deposit was scanned (a), showing low and flat background, then evaporated. Following this, a Ba/SXe deposit was done, and two Ba atom peaks were identified (b). Another scan of the same area was done immediately after, showing the persistence of the Ba atom peaks (c). This is followed by a SXe-only deposit, which is consistent with the earlier background scan, indicating the Ba was completely evaporated from the sample (d).

The fluorescence rate of a single Ba atom in the scan is,

$$F = \frac{R \times \epsilon_{ccd}}{\epsilon_{coll}} \quad (4.1)$$

where F is the fluorescence rate of a single Ba atom in photons/mWs, $\epsilon_{ccd} = 2.38$ is the specified number of photons collected per CCD count including CCD quantum efficiency at 619 nm, and $\epsilon_{coll} = 1.1 \times 10^{-2}$ is the collection efficiency of the optics [49]. R is the count rate in counts/mWs

of the camera, given as the amplitude of a 2D Gaussian fit to the Ba atom peak composite image. This fit is done with the average of the SXe-only background composite images in Fig. 4.5 (a) and (d) subtracted. The fluorescence rates of the atoms in Figs. 4.5 (b) and (c) were found to be 1.1×10^6 photons/mWs and 1.0×10^6 photons/mWs for the left and right atoms respectively.

The fluorescence efficiency, ϵ_f , can be determined from these fluorescence rates using Eq. 4.2, repeated below in a more convenient form:

$$\epsilon_f = \frac{F A_l hc}{\sigma_{sxe}(\lambda_{ex}) \lambda_{ex}} \quad (4.2)$$

In this equation, hc/λ_{ex} is the energy of a photon at the excitation wavelength of $\lambda_{ex} = 570$ nm. A_l is the laser area, obtained using $A_l = \frac{1}{2}\pi w_x w_y$ where $w_x = 5.72$ μm and $w_y = 9.39$ μm are the average laser spot sizes from Table 3.8 projected into the plane of the Ba atom. The absorption cross-section, $\sigma_{sxe}(\lambda_{ex}) = 8.5 \times 10^{-16}$ cm^{-2} was obtained from the curve in Fig. 2.10. This yields a fluorescence efficiency of 39% for the left atom and 36% for the right atom. The uncertainty on both the fluorescence rate and efficiency is high, perhaps on the order of a factor of 2, due to uncertainty on ϵ_{coll} and the assumptions upon which the estimation of σ_{SXe} was based.

4.3 Ba Fluorescence Turn-off

To investigate the persistence of the fluorescence, the laser was moved close to the position of the atom on the left in Fig. 4.5 (b) and (c). Once the laser was moved to the atom's location, 50 exposures of 3 s were taken. Fig. 4.6 shows the collected fluorescence vs. exposure time (blue points) of the atom. The points are 3×3 integrals of each CCD image around the laser area. To estimate an uncertainty in the CCD counts for each point in Fig. 4.6, the Poissonian uncertainty, \sqrt{N} , in the number of collected photons, N , is combined with the measured digitizing noise of 3 counts/pixel in quadrature. The integrated counts and associated uncertainties are then scaled by the relative laser exposure to correct for small exposure differences between images. The methods for calculating the normalized power and exposure time are described in Sec. 3.5.1.

The fluorescence of the atom persists for the first 8 exposures before dropping abruptly to the background level. This “turn-off” of the fluorescence is a hallmark of a single atom. Fig. 4.6 also shows the collected fluorescence vs. time for a location away from the Ba peak on the same deposit (green points), and for a SXe-only deposit (red points). The average laser power for these images was $20 \mu\text{W}$.

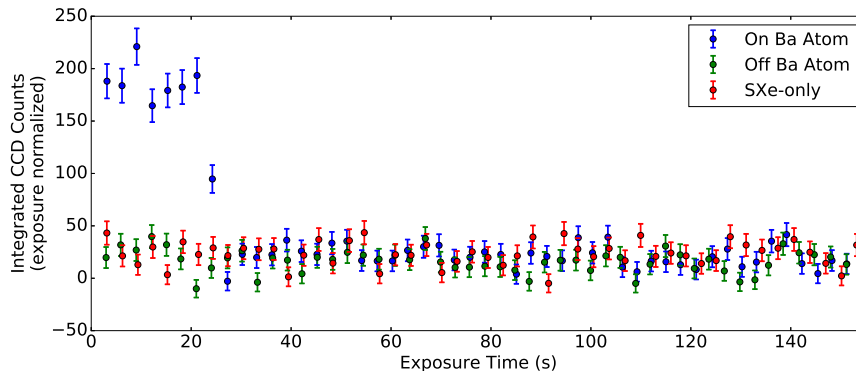


Figure 4.6: The fluorescence vs. time for three laser spots are plotted. The blue points are near the location of the Ba atom on the left in Fig. 4.5 (b) and (c), $(x,y)=(4.75,6.00)$. For the green points the laser is at a location away from this Ba peak where no strong fluorescence was observed, $(x,y)=(7.50,6.00)$. For the red points the laser is at the center of the SXe-only deposit shown in Fig. 4.5 (d).

For the first 7 images in which the atom is fluorescing, an average of 399 photons ($2.38 \text{ CCD counts/photon}$) are detected in each image, compared to the SXe-only background level of 56 ± 27 photons per 3 s exposure. Thus, the fluorescence signal of this Ba atom is 14σ above the background fluctuations with $65 \mu\text{W s}$ of laser exposure. The peak pixel of the Ba atom peak is at $(4,7)$ in the scan grid. The peak counts in the first and second scans are 258 and 272, respectively. This is higher than the average of 187 counts for the first 7 points in Fig. 4.6, due to the fact that the fixed laser was not positioned optimally when moved to the laser location. The pixel closest to the laser position, $(5,6)$, has 182 and 169 counts in the first and second scans, which is in agreement with the fluorescence signal measured at the chosen laser position. The signal to background fluctuation ratio of the fluorescence can also be specified for the duration of the emitted fluorescence of the atom after the laser has been moved to its location. A total of about 3300 photons were detected from

this Ba atom before turning off after ~ 30 s of exposure, including the two previous scans done. For comparison, 555 ± 62 photons were collected from 30 s of SXe-only background, with the uncertainty being the standard deviation of the five 30 s integrations of the SXe-only background. The signal of this Ba atom's fluorescence with 30 s of observation is 53σ above the background fluctuations, which is a significant improvement over the 3 s observation time.

The total number of photons emitted by this Ba atom is of interest can be calculated, including the exposure during the 2 scans. This was done by constructing the composite images in Fig. 4.5 without scaling by laser exposure and using a 3×3 integration region. The number of photons emitted during the scans was determined by summing the counts from a 2×2 group of adjacent laser locations constituting the Ba peak with the average of the SXe-only runs subtracted. When these counts are included, 5602 total fluorescence photons were detected from this Ba atom. Using the light collection efficiency of 1.1%, this corresponds to 5.2×10^5 photons emitted.

After the atom was observed for 150 s, and was seen to turn off, another scan of the original laser area was done. The composite image of this scan is shown in Fig. 4.7 (b) with the scanned image taken before the turn-off experiment (a), which is the same composite image as Fig. 4.5 (c), for comparison. As expected, the peak from the turned-off Ba atom is no longer present in the second scan.

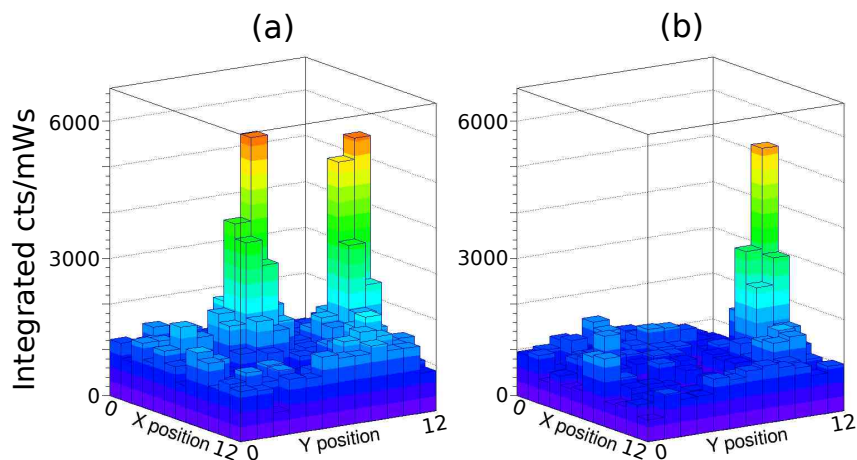


Figure 4.7: Composite images of the scan immediately preceding (a) and the scan following (b) the turn-off of the Ba fluorescence. The peak corresponding to the turned-off atom is absent after the Ba atom ceased fluorescing.

The scanning procedure was repeated for another Ba/SXe deposit, done before the final SXe-only scan in Fig. 4.5 (d). This deposit had 452_{-136}^{+90} Ba⁺ ions in the scan area. A 3D plot of the composite image of this run is shown in Fig. 4.8 (c) with the first SXe-only background and the Ba scan in Figs. 4.5 (a) and (b), respectively, shown for comparison. The two strong peaks observed in (c) have similar peak signals to those in the earlier deposit (b), and are attributed to single Ba atom fluorescence. These two atom peaks are close together, which makes fitting a 2D Gaussian to extract the peak height difficult. A reasonable fit was obtained for the taller atom peak, and it returned a fluorescence rate of 1.19×10^6 photons/mWs, and a fluorescence efficiency of 40.0%, which are similar to these quantities for the atoms fit in the previous deposit. This image also shows three weaker peaks at the edges of the scanned region, located at (7,1), (12,8) and (9,12). These may be due to barium atoms slightly outside the scanned region, that are partially illuminated by the laser at the edge of the scan.

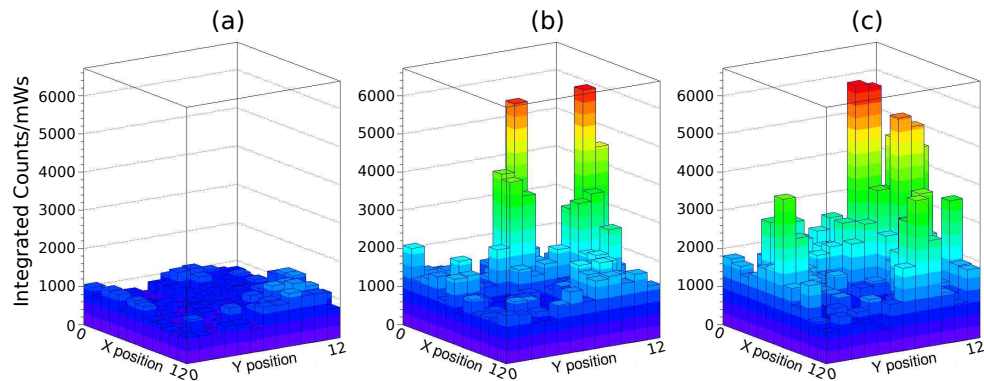


Figure 4.8: Composite images of the scans of different deposits are shown. The scan of another Ba/SXe deposit with 452_{-136}^{+90} Ba⁺ ions deposited is shown in (c). Several Ba atom peaks are present in this composite image. The scans in (a) and (b) are the same as shown Fig. 4.5 (a) and (b), and are reproduced on the same scale as (c) for comparison.

After a scan of the sample was done, the laser was moved to the location of the largest Ba peak, and 50 exposures of 3 s were taken. The laser was then moved off of the Ba spot to position (7.5,7.5), and 50 more 3 s exposures were taken. The 3×3 integrals of these images, normalized for exposure differences, are shown in Fig. 4.9. The SXe-only background and the error bar defi-

nition are the same as in as Fig. 4.6. For the first 7 images with full Ba fluorescence, an average of 568 photons were collected in 58 $\mu\text{W s}$ of laser exposure, which is 21σ above background fluctuations. In this case, the laser was actually moved to the correct atom position, resulting in higher signal than in Fig. 4.6. A total of 4181 photons were detected from the scan image and the first 7 fixed laser images, resulting in a signal level 89σ above the background fluctuations. Including the photons collected in the scan from a 2×2 area around the peak location, a total of 5367 photons were detected, corresponding to 5.1×10^5 total emitted photons from this atom, which is similar to the Ba atom discussed earlier.

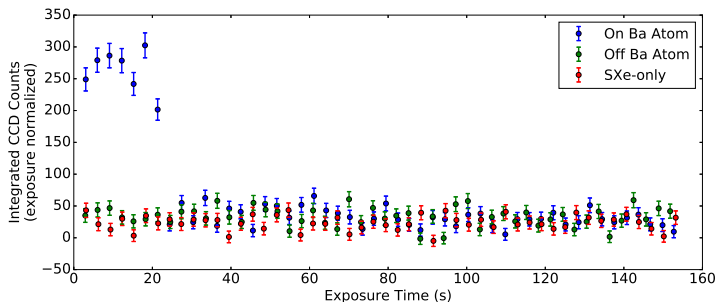


Figure 4.9: Fluorescence vs. time for the large central Ba atom observed in Fig. 4.8 (c), as well as a spot away from the atom. The SXe-only background run used is the same as in Fig. 4.6. This atom exhibits higher signal than the Ba atom in that figure. This is due to more accurately centering the laser on the atom.

4.4 Additional Ba Scan and Fluorescence Turn-off Experiments

Individual Ba atoms were observed in Ba deposits on four additional days in June, 2018. Each experiment day is treated separately, since the quality of the conditions for the SXe deposits varied between days. Generally, the conditions were stable throughout a day of several deposits and laser scans. After scanning the deposits for Ba atom peaks, the laser was moved to one or more (but not necessarily all) of the detected peaks and the time dependence of the fluorescence was observed.

4.4.1 Scan Results

Due to the differences in background level, the scans for the following experiments will all be presented with the SXe-only background subtracted. One example of the SXe-only background on each day is shown in Fig. 4.10, and the average value and standard deviation of that composite image is given in Table 4.1. It can be seen that the SXe-only background for 11 May 2018 was significantly lower than the other days. Scans from this day were discussed in Sec. 4.3.

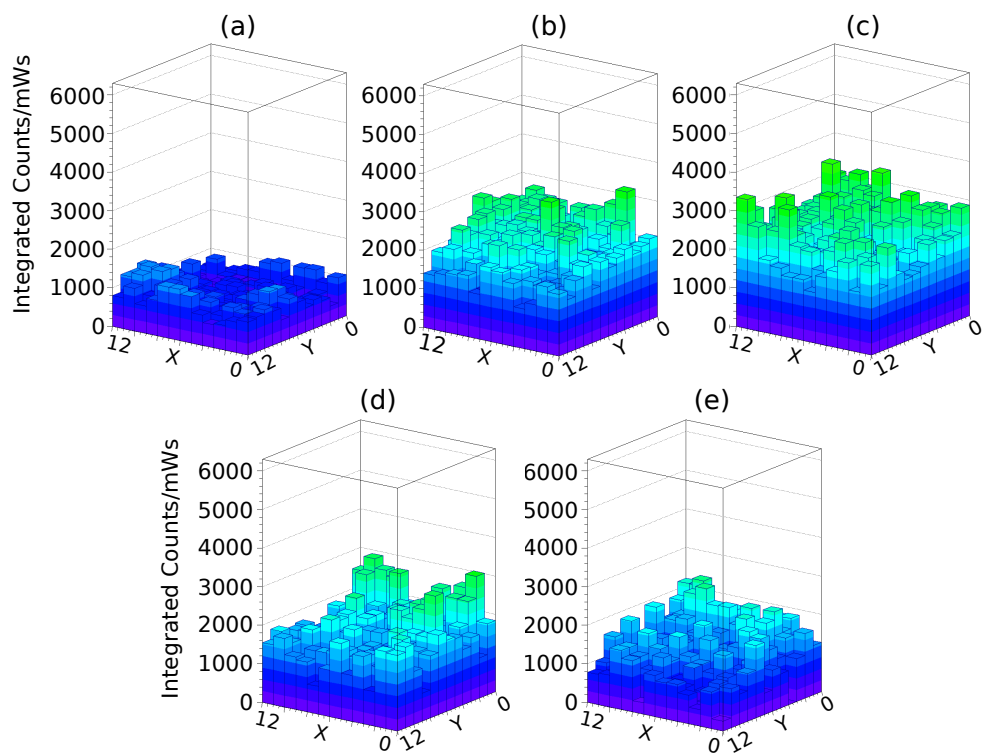


Figure 4.10: An example of a SXe-only composite image from each experiment is shown. The dates are: (a) 11 May 2018, (b) 13 June 2018, (c) 14 June 2018, (d) 20 June 2018, and (e) 21 June 2018.

A total of 7 additional Ba/SXe deposits were scanned over the other four days of experiments. The composite images of the first scan of each Ba/Xe deposit with the average SXe-only background composite image subtracted are shown in Figs. 4.11 - 4.14, grouped by experiment day. In each of these figures, strong Ba fluorescence peaks are observed, and the strongest peaks are labeled. For each strong Ba atom peak, the peak height and ratio of the peak height to the standard

Table 4.1: Average counts/mWs and standard deviations for SXe-only background laser scans. Values are given for both the single scan examples in Fig. 4.10 and the average SXe-only composite image constructed from all the background images on a given day.

Experiment Day	Scan Shown in Fig. 4.10 (counts/mWs)	Average Xe Composite Scan (counts/mWs)
11 May 2018	791 ± 269	779 ± 223
13 June 2018	2009 ± 452	2150 ± 303
14 June 2018	2312 ± 461	2875 ± 437
20 June 2018	1673 ± 482	2025 ± 402
21 June 2018	1213 ± 501	1149 ± 370

deviation of the average xenon composite image, σ_{bkg} , are given in Table 4.2. The Ba fluorescence peaks in the 11 May 2018 experiment have the highest peak/ σ_{bkg} values. The larger background fluctuations on the other days limited this ratio, but the Ba peaks are still clearly visible.

The clearest Ba peak heights are consistently in the range $\sim 2800 - 5800$ counts/mWs, with a few exceptions. Three of the Ba peaks observed on 13 June 2018 are below this range, and the strongest, atom 3, is only 3141 counts/mWs high, and is highly localized to one laser position. The reason for the Ba fluorescence signal to be low on this day is not understood. The remaining days had Ba peak heights in the nominal range. The Ba peaks found on 14 June 2018 are of typical height with one significant outlier, atom 5, which has about twice the usual peak height. This anomalously high signal appears in both scans of the deposit, and when the laser was moved to the location of the atom. The Ba ion deposits are sparse enough to make the probability of two atoms being within one laser area low, but this possibility cannot be fully dismissed. The final two days 20-21 June 2018 show both a lower SXe-only background and consistent strong peak heights in the nominal range. The system was baked out for two days immediately before these experiments, and a lower residual gas level might contribute to the higher quality of these scans. Despite the variation in background and fluorescence strength over the experiments, Ba atoms were reliably imaged via laser scanning, demonstrating that this technique is robust.

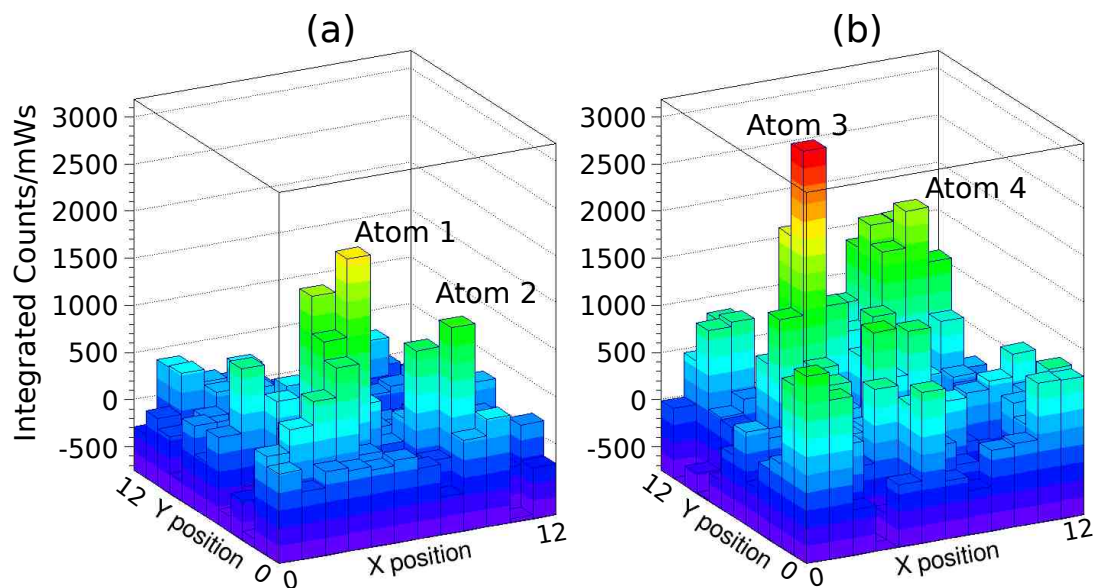


Figure 4.11: Composite images of the first scan of two Ba/SXe deposits on 13 June 2018. The scans in (a) and (b) have 163_{-49}^{+33} and 144_{-43}^{+28} Ba^+ ions deposited respectively. The locations of four strong peaks due to individual Ba atoms are labeled.

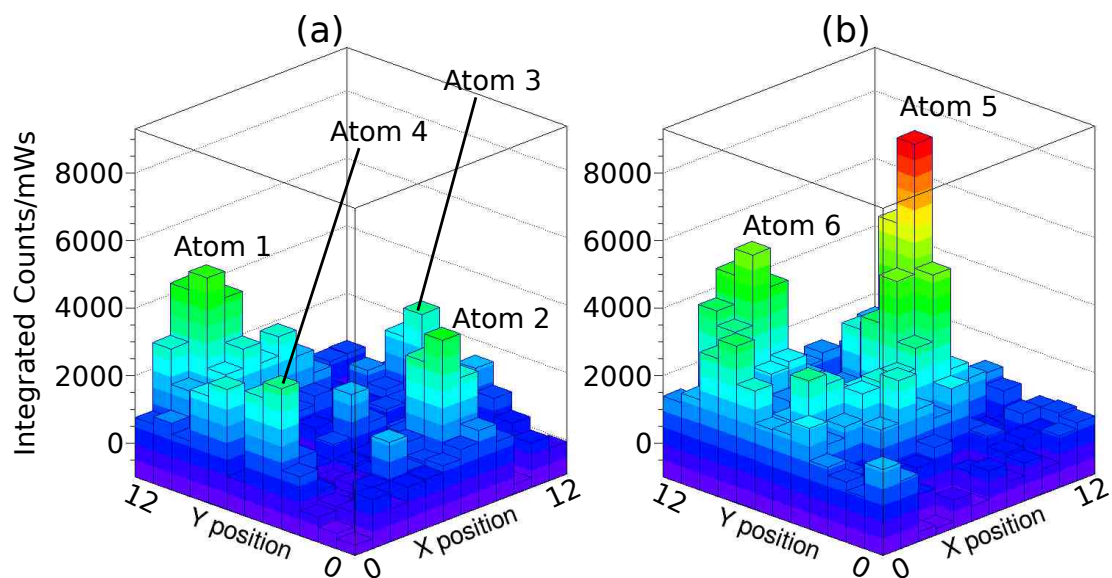


Figure 4.12: Composite images of the first scan of two Ba/SXe deposits 14 June 2018. The scans in (a) and (b) have 181_{-54}^{+36} and 142_{-43}^{+28} Ba^+ ions deposited respectively. The locations of six strong peaks due to individual Ba atoms are labeled.

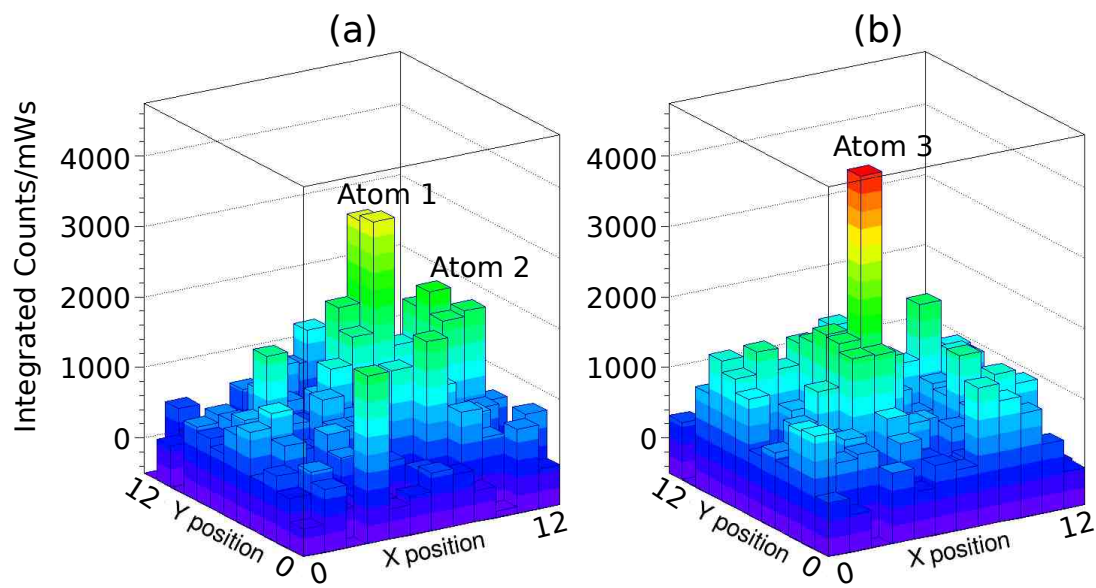


Figure 4.13: Composite images of the first scan of two Ba/SXe deposits 20 June 2018. The scans in (a) and (b) have 124_{-37}^{+25} and 128_{-38}^{+26} Ba^+ ions deposited respectively. The locations of three strong peaks due to individual Ba atoms are labeled.

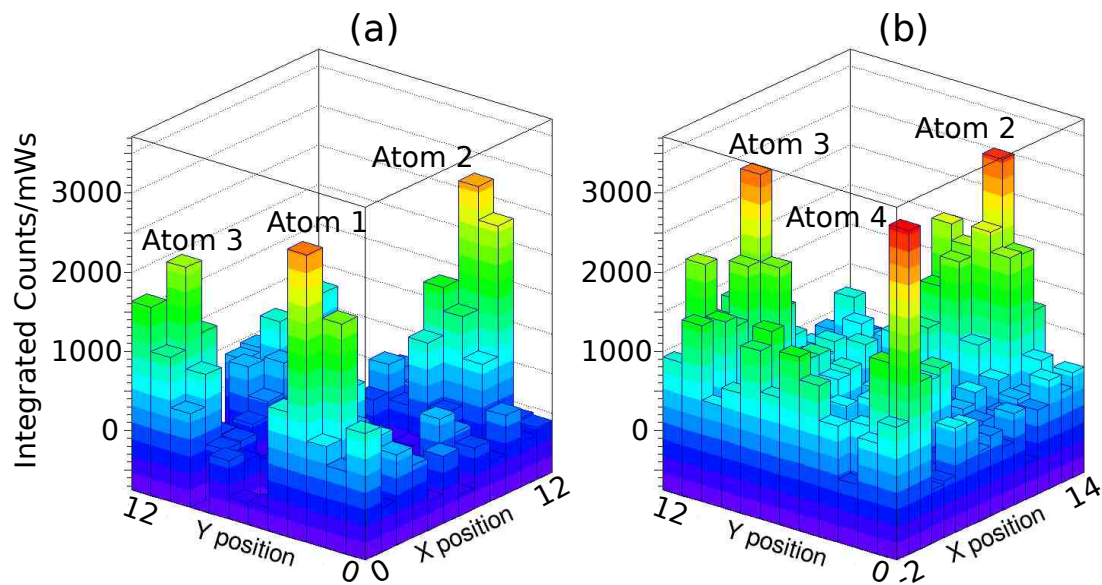


Figure 4.14: Composite images of two scans of the same Ba/SXe deposit on 21 June 2018. The first scan (a) used the same scan parameters as all the previous scans, and has 127_{-38}^{+26} Ba^+ ions deposited in the scanned area. The repeat scan in (b) used an expanded scan of 16×12 with the same $4 \mu\text{m}$ step. The grid was started 2 steps left of the first scan, and this change is reflected in the axis label. The second scan found another strong peak outside the original scan area, as well as two of the atoms found in the original scan.

Table 4.2: Table of data for each single Ba atom fluorescence peak observed. These values correspond to 3 s exposures at about 60 μW

Experiment Day	Atom	Peak Value (counts/mWs)	Peak Value/ σ_{bkg}
11 May 2018	1	4865	22
	2	5369	24
	3	5715	27
	4	4470	20
13 June 2018	1	2147	7
	2	1326	4
	3	3141	10
	4	1857	6
14 June 2018	1	4863	11
	2	3969	9
	3	2957	7
	4	3158	7
	5	8865	20
	6	5353	12
20 June 2018	1	3227	8
	2	2842	7
	3	4258	11
21 June 2018	1	2886	8
	2	2732	7
	3	2114	6
	4	3332	10

Fluorescence rates and efficiencies of each Ba atom were calculated, as described in Sec. 4.2. A reasonable 2D Gaussian fit to the Ba atom fluorescence signal was not always obtained, particularly for atoms located near the edge of a scan. This was also occasionally the case for the weaker of two closely spaced atom peaks. The averages, weighted by the fit uncertainties, and standard deviations for the atoms observed on each day are given in Table 4.3. The overall average fluorescence rate is 8.6×10^5 photons/mWs, and the average fluorescence efficiency is 30%. As noted in Sec. 4.2, the uncertainties on these values are high.

Table 4.3: The fluorescence rates and efficiencies of the Ba atoms observed for which a fit to the peak was obtained, combined by experiment day. The values and uncertainties for the fluorescence rate and efficiency for all days are a weighted average and the standard deviation of the mean of the values for each day.

Experiment Day	# of Atoms	Fluorescence Rate (photons/mWs)	Fluorescence Efficiency (%)
11 May 2018	3	$11.2 \pm 0.8 \times 10^5$	38.6 ± 2.8
13 June 2018	2	$6.4 \pm 0.8 \times 10^5$	21.9 ± 2.6
14 June 2018	5	$9.2 \pm 0.6 \times 10^5$	31.8 ± 2.0
20 June 2018	2	$7.2 \pm 0.8 \times 10^5$	24.9 ± 3.0
21 June 2018	3	$10.1 \pm 1.2 \times 10^5$	34.8 ± 4.0
All Days	15	8.6×10^5	30

4.4.2 Additional Fluorescence Turn-off Results

Many of the atoms identified in the additional composite images were observed for an extended period of time with the laser fixed on the peak, as discussed in Sec. 4.3. A total of 16 atoms, including the two from the 11 May experiment have been studied. The fluorescence vs. time plots of the atoms in each deposit are plotted together. The plots for each day are shown in Figs. 4.15 - 4.18, with the atom numbering defined in Figs. 4.11 - 4.14. On 13 June, the background was estimated by taking 3 s images of a spot away from any Ba atoms in the first Ba deposit. For the subsequent days, the SXe-only background was measured by taking 3 s images at the center of a SXe-only deposit. The average and $\pm 1\sigma$ level of the background from each day is shown as the black dashed line and gray band in the fluorescence vs. time plots. Of the 14 atoms observed, 7 persisted fluorescing throughout the entire observation period, generally ~ 640 s, with one fluorescing for over 800 s. The persistence time and laser exposure for each atom are calculated by summing the exposure time and integrated laser exposure in each image up to the last image before the fluorescence signal drops to the background level. Results are given in Table 4.4. The longest exposure, for atom 1 on 13 June, produced 7.5×10^4 detected photons, or 6.8×10^6 emitted photons from a single Ba atom.

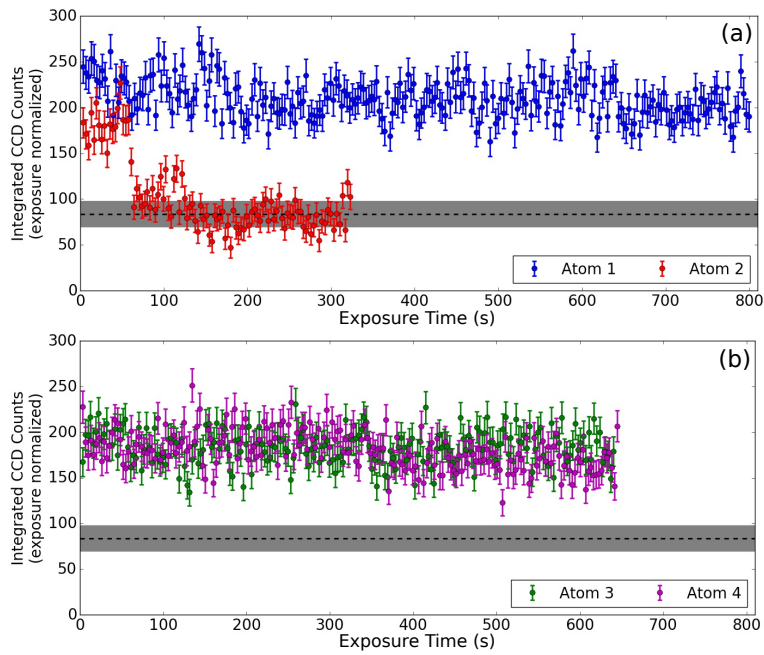


Figure 4.15: The fluorescence vs exposure time for the four atoms observed in the two deposits on 13 June 2018.

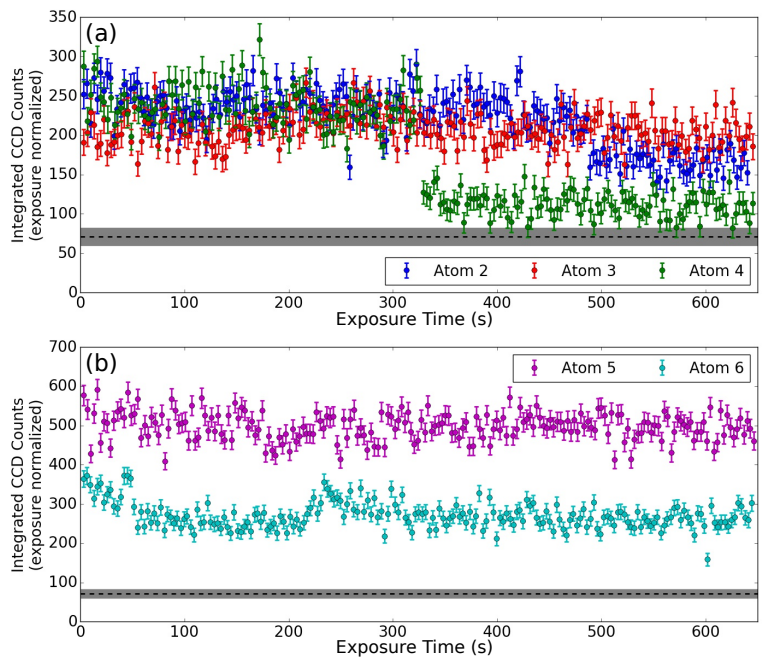


Figure 4.16: The fluorescence vs exposure time for five of the six atoms identified in the two deposits on 14 June 2018.

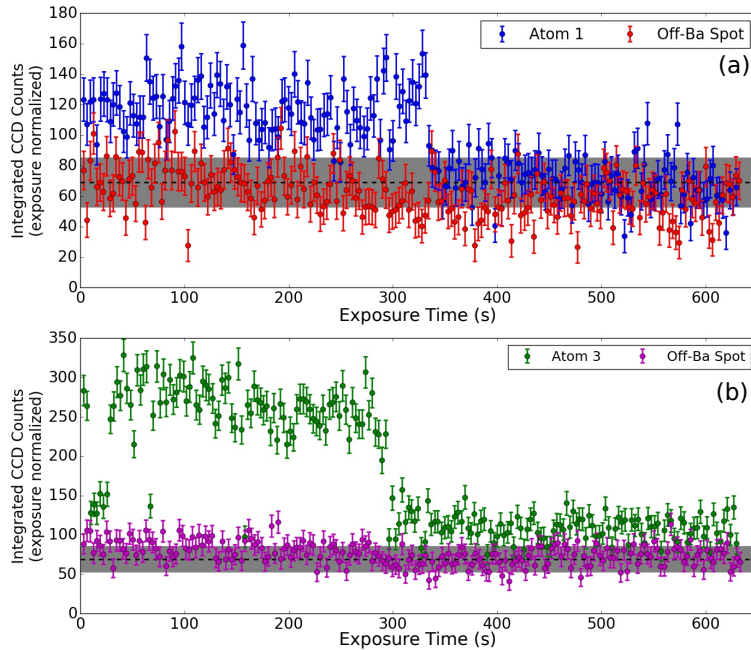


Figure 4.17: The fluorescence vs exposure time for the two atoms observed in the two deposits on 20 June 2018.

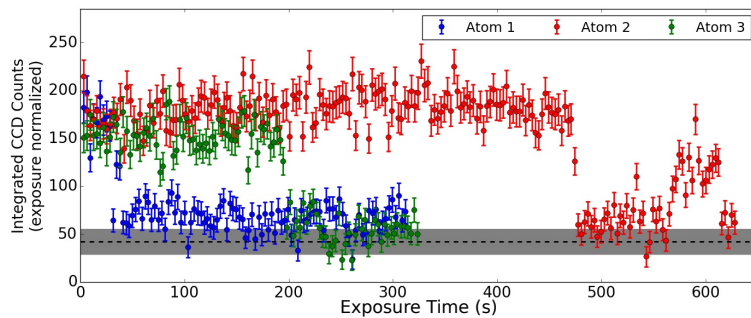


Figure 4.18: The fluorescence vs exposure time for the three atoms observed in the first scan of the deposit on 21 June 2018.

Four atoms were observed with the laser fixed on their location on 13 June, and the fluorescence vs. time data of these atoms are shown in Fig. 4.15. Three of the atoms (1, 3, and 4) persist for the entire observation time. Atom 1 persists for 800 s and was the atom observed for the longest time. On 14 June, five atoms were observed. The fluorescence vs. time data for each atom are shown in Fig. 4.16. Four of the atoms (2, 3, 5 and 6) persisted for the entire 640 s observation time. Atom 5 has notably higher signal, as mentioned before. The high signal may be due to more than one resonant atom being illuminated by the laser at one position. Four atoms were observed on 20

June. Plots of the fluorescence vs. time data for these atoms are shown in Fig. 4.17. Both atoms cease fluorescing while being observed. A location not near any Ba atoms in each deposit were also observed, and are both consistent with the SXe-only background level. On 21 June, all three atoms were observed to turn off, with persistence times varying from 28 s - 471 s.

Two of the atoms appear to resume fluorescing after having turned off. Atom 3 on 20 June turns off once for ~ 18 s near the beginning, and for a single 3 s image twice later in the observation. The atom fully turns off after 292.8 s, and does not fluoresce again for the remaining time. Atom 2 on the following day (21 June) turns off after 471 s, and then returns to fluorescing for ~ 40 s, at a lower rate than before turning off. A “blinking” behavior has been observed in both single molecules and quantum dot fluorescence. We do not yet have enough statistics to characterize the blinking of Ba atoms in SXe. The partial loss or return of fluorescence might be due to blinking on a time scale shorter than the 3 s image times, giving a lower average fluorescence rate for that image. Clearly, this blinking process needs more investigation, as the mechanism leading to this behavior is not understood at this time.

The number of photons collected and signal to σ_{bkg} ratios for a single 3 s image and a 21 s integration was calculated. A 21 s integration time was chosen to give a comparable measure for all atoms observed, since it is the shortest turn off time of all the atoms observed. The fluctuations in the 21 s integrations were estimated by binning the 3 s background images in groups of seven and taking the standard deviation of the bins. Results are given in Table 4.5. A mean of 373 photons are collected in a 3 s image for the atoms observed and the signal is $13\sigma_{bkg}$ above the background fluctuations. For the 21 s integrations, a mean of 2625 photons were collected from the Ba atoms, and the mean signal to σ_{bkg} ratios is 36 for these longer integrations.

Table 4.4: The persistence of the fluorescence is given for each atom observed. This table considers only the images taken after the scans were done.

Experiment Day	Atom	Persistence Time (s)	Exposure (mWs)
11 May 2018	1	24.3	0.53
	2	21.3	0.40
13 June 2018	1	> 800	> 21.57
	2	57.7	1.40
	3	> 640.1	> 12.44
	4	> 644.7	> 13.35
14 June 2018	2	> 640.1	> 11.54
	3	> 645.1	> 16.41
	4	326.1	7.57
	5	> 646.2	> 13.40
	6	> 644.1	> 13.46
	20 June 2018	1	331.3
	3	292.8	3.46
21 June 2018	1	28.5	0.56
	2	471.0	6.21
	3	194.7	3.97

Table 4.5: Collected photons and signal to background fluctuation ratios for all individual Ba atoms observed. The 21 s integrations are created by summing successive groups of 7 consecutive image signals. The reported number is the average over all the different groups.

Experiment Day	Atom	3 s Image		21 s Integration	
		Collected Photons	Signal/ σ_{bkg}	Collected Photons	Signal/ σ_{bkg}
11 May 2018	1	370*	14	2795	64
	2	568	21	3980	89
13 June 2018	1	299	9	2091	27
	2	233	7	1597	21
	3	237	7	1665	22
	4	230	7	1610	21
14 June 2018	2	356	14	2506	30
	3	324	12	2277	28
	4	397	15	2766	34
	5	1016 [†]	39	7110	86
	6	478	18	3325	40
20 June 2018	1	121	3	798	8
	3	442	11	3144	30
21 June 2018	1	308	10	2164	23
	2	332	11	2329	25
	3	262	8	1843	20

* Laser not centered on atom location

[†] Potential atom overlap

Chapter 5

Conclusions

Individual Ba atoms implanted in SXe have been imaged by laser induced fluorescence of the 619 nm emission line using a focused laser scanning procedure developed in this thesis. This is the first demonstration of resolved imaging of single atoms in a solid noble element. This work is a major step towards a practical Ba tagging technique for the rejection of backgrounds in a neutrinoless double beta decay ($0\nu\beta\beta$) search with the proposed nEXO experiment.

Low densities of Ba ions were co-deposited with xenon, with some of the Ba^+ ions neutralizing in the SXe matrix, to create samples of Ba atoms in solid xenon. The 619 nm fluorescence rate vs. the number of Ba^+ ions deposited in the laser region was found to be 284_{-85}^{+57} counts/mWs per ion. A linear relationship between the fluorescence rate and the number of Ba^+ ions deposited was observed, indicating this fluorescence is due to Ba atoms, rather than Ba_n molecules. A technique for scanning the excitation laser was developed and used to image individual Ba atoms deposited in the SXe matrix. The repeatability of this technique was demonstrated by imaging 21 individual Ba atoms over five days of experiments. Although the background from SXe-only deposits varied between experimental runs, atoms were successfully imaged in each run, demonstrating the robustness of the technique. A fluorescence efficiency of about 30% was measured for the 15 Ba atoms. After imaging the Ba atoms using the scanning method, the laser was moved to the location of an atom and the fluorescence level was observed as a function of laser exposure. Of the 16 Ba atoms investigated, 9 ceased fluorescing while being observed after 0.4 - 7.6 mW s of laser exposure. This sudden turn-off of the fluorescence is a hallmark of single atoms. The effectiveness of removing Ba atoms from the sample by evaporation at 100 K has also been demonstrated to a limit of $\leq 0.16\%$. This is crucial for a potential nEXO application, since it allows the tagging of a Ba daughter from a suspected $0\nu\beta\beta$ event to be independent of previous tags. The results of the imaging experiments presented in this thesis are accepted for publication in Nature [87].

Collaboration with J.G. McCaffrey and B. Gervais has led to the assignment of the 619 nm fluorescence to Ba atoms in a single vacancy (SV) site of the SXe matrix. The mechanism for the formation of this site from incident Ba⁺ ions was developed by Silverman and Fajardo [71] for the Na/Ar system, which is a good analogy for Ba guest atoms in SXe. When the Ba⁺ ions are deposited in the SXe layer, their tight binding with Xe prefers a single vacancy matrix site. After the ion neutralizes, the atom is held in the SV site by the cohesion energy of the matrix, thus cannot displace the neighbor Xe atoms to create the larger vacancy site preferred by the Ba atom. Preliminary molecular dynamics simulations by B. Gervais have produced an excitation spectrum that agrees in shape and width with the observed spectrum [77]. The uncertainty in the Ba-Xe potential at such close range has prevented close agreement on the peak excitation and emission wavelengths, and the calculation of this potential is being refined.

5.1 Future Work

Barium atoms in SXe are known to fluoresce at other wavelengths, corresponding to the Ba atom occupying different matrix sites [43]. Expanding the single atom imaging technique developed here to these other sites is desirable for an eventual nEXO application, as a high Ba tagging efficiency is required. Our group has imaged down to the ~ 1000 atom level for both the 577 nm and 590 nm emission lines [43, 49]. These lines exhibit significantly faster bleaching than the 619 nm line, and thus require higher photon detection efficiency to image since fewer total photons are emitted. With the refining of the scanning technique and the use of a more sensitive electron-multiplying CCD camera, single atoms may be imaged using these emission lines. In addition to demonstrating the ability to image individual atoms in different matrix sites, this may allow a determination of the site occupancy ratios under conditions of 2 keV Ba⁺ ion implantation to be made. Implementing a laser with a wider tuning range than available with the current dye laser and a mechanism for changing fluorescence filters quickly would allow multiple matrix sites to be imaged in the same Ba/SXe deposit.

The Ba daughter is most likely to be in the Ba^+ charge state after $\beta\beta$ decay [40]. Since the neutralization fraction upon freezing into SXe may not be unity, the capability of imaging single Ba^+ would be highly beneficial to a complete Ba tagging technique for nEXO. Our group has also investigated the fluorescence of Ba^+ ions in SXe [43]. The ions were excited between 460 nm - 490 nm, and emission peaks at 532, 553, 568, 635, and 669 nm were observed. The bleaching behavior of the 532 nm and 568 nm lines was studied, and found to be negligible after the first 10 seconds of exposure at an excitation rate of $1 \times 10^7 \text{ s}^{-1}$ for deposits of large numbers of Ba^+ ions [88]. This is encouraging for extending the scanning technique to image individual Ba^+ ions.

A cryogenic probe and extraction device with the ability to freeze Ba^+ ions into SXe out of a liquid xenon cell is also being developed in this group. A copper holder for a sapphire window has been attached to replicate the imaging set-up used for this thesis. Thus the results presented in this work are directly applicable to imaging Ba atoms on the cryoprobe under development. The extraction and detection of Ba atoms on the probe may help determine if the Ba^+ are predominantly neutralized or remain as ions and the favored Xe matrix sites when extracted at low energy from liquid Xe, as opposed to the 2 keV deposition energy of the ion beam source. Integrating the two systems to image single Ba atoms extracted from LXe is the ultimate goal for demonstration of a viable Ba tagging scheme for nEXO.

Bibliography

- [1] C.D. Ellis and W.A. Wooster. The average energy of disintegration of radium E. *Proc. R. Soc. Lond. A*, 117:109–123, 1927.
- [2] E. Fermi. *Zeitschrift für Physik*, 88(161), 1934.
- [3] C. L. Cowan, F. Reines, F. B. Harrison, H. W. Kruse, and A. D. McGuire. Detection of the free neutrino: a confirmation. *Science*, 124(3212):103–104, 1956.
- [4] B. T. Cleveland et al. (Homestake Experiment). Measurement of the Solar Electron Neutrino Flux with the Homestake Chlorine Detector. *ApJ*, 496:505–526, mar 1998.
- [5] K. S. Hirata et al. (Kamiokande Collaboration). Results from one thousand days of real-time, directional solar-neutrino data. *Phys. Rev. Lett.*, 65:1297–1300, Sep 1990.
- [6] J. N. Abdurashitov et al. (SAGE Collaboration). Results from SAGE (the russian-american gallium solar neutrino experiment). *Phys. Lett. B*, 328(1):234 – 248, 1994.
- [7] P. Anselmann et al. (GALLEX Collaboration). GALLEX results from the first 30 solar neutrino runs. *Phys. Lett. B*, 327(3):377 – 385, 1994.
- [8] Q.R. Ahmad et al. (SNO Collaboration). Direct evidence for neutrino flavor transformation from neutral-current interactions in the Sudbury Neutrino Observatory. *Phys. Rev. Lett.*, 89:011301, Jun 2002.
- [9] B. Aharmim et al. (SNO Collaboration). Combined analysis of all three phases of solar neutrino data from the Sudbury Neutrino Observatory. *Phys. Rev. C*, 88:025501, Aug 2013.
- [10] Y. Fukuda et al. (Super-Kamiokande Collaboration). Evidence for oscillation of atmospheric neutrinos. *Phys. Rev. Lett.*, 81:1562–1567, Aug 1998.
- [11] K. Abe et al. (Super-Kamiokande Collaboration). Atmospheric neutrino oscillation analysis with external constraints in Super-Kamiokande I-IV. *Phys. Rev. D*, 97:072001, Apr 2018.

- [12] M. Fukugita and T. Yanagida. Baryogenesis without grand unification. *Phys. Lett. B*, 174(1):45–47, 1986.
- [13] E. Kh. Akhmedov, V. A. Rubakov, and A. Yu. Smirnov. Baryogenesis via neutrino oscillations. *Phys. Rev. Lett.*, 81:1359–1362, Aug 1998.
- [14] J. B. Albert et al. (EXO-200 Collaboration). Search for neutrinoless double-beta decay with the upgraded EXO-200 detector. *Phys. Rev. Lett.*, 120:072701, Feb 2018.
- [15] J. B. Albert et al. (nEXO Collaboration). Sensitivity and discovery potential of the proposed nEXO experiment to neutrinoless double- β decay. *Phys. Rev. C*, 97:065503, Jun 2018.
- [16] C. Patrignani et al. (Particle Data Group). *Chin. Phys. C*, 40(100001), 2016.
- [17] N. Aghanim et al. Planck 2018 results. VI. Cosmological parameters. 2018.
- [18] M. Kleesiek et al. β -Decay Spectrum, Response Function and Statistical Model for Neutrino Mass Measurements with the KATRIN Experiment. 2018.
- [19] M. Goeppert-Mayer. Double beta-disintegration. *Phys. Rev.*, 48, Sep 1935.
- [20] W. H. Furry. On transition probabilities in double beta-disintegration. *Phys. Rev.*, 56, Dec 1939.
- [21] S. Herrin. *Double beta decay in xenon-136: measuring the neutrino-emitting mode and searching for majoron-emitting modes*. PhD dissertation, Stanford University, 2013.
- [22] Murray Gell-Mann, Pierre Ramond, and Richard Slansky. Complex Spinors and Unified Theories. *Conf. Proc.*, C790927:315–321, 1979.
- [23] Tsutomu Yanagida. Horizontal symmetry and masses of neutrinos. *Conf. Proc.*, C7902131:95–99, 1979.
- [24] K. S. Babu and V. S. Mathur. Radiatively induced seesaw mechanism for neutrino masses. *Phys. Rev. D*, 38:3550–3553, Dec 1988.

- [25] Rabindra N. Mohapatra and Goran Senjanović. Neutrino mass and spontaneous parity non-conservation. *Phys. Rev. Lett.*, 44:912–915, Apr 1980.
- [26] A. D. Sakharov. Violation of CP Invariance, C asymmetry, and baryon asymmetry of the universe. *Pisma Zh. Eksp. Teor. Fiz.*, 5:32–35, 1967. [Usp. Fiz. Nauk161,no.5,61(1991)].
- [27] S.F. King. Neutrino mass models. *Rept.Prog.Phys.*, 67, 2004.
- [28] I. Gil-Botella. Neutrino physics. *arXiv:1504.03551 [hep-ph]*, 2015.
- [29] M. Tanabashi et al. (Particle Data Group). *Phys. Rev. D*, 98(030001), 2018.
- [30] K.A. Olive et al. (Particle Data Group). *Chin. Phys. C*38, 090001, 2014.
- [31] M. Auger et al. The EXO-200 detector, part I: Detector design and construction. *JINST*, 7:P05010, 2012.
- [32] M. Redshaw et al. Mass and double beta decay Q value of Xe-136. *Phys.Rev.Lett.*, 98(053003), 2007.
- [33] J. B. Albert et al. Measurement of the Drift Velocity and Transverse Diffusion of Electrons in Liquid Xenon with the EXO-200 Detector. *Phys. Rev. C*, 95(2):025502, 2017.
- [34] F. LePort et al. A Magnetically-driven piston pump for ultra-clean applications. *Rev. Sci. Instrum.*, 82:105114, 2011.
- [35] D. S. Leonard et al. Systematic study of trace radioactive impurities in candidate construction materials for EXO-200. *Nucl. Instrum. Meth.*, A591:490–509, 2008.
- [36] J. B. Albert et al. Investigation of radioactivity-induced backgrounds in EXO-200. *Phys. Rev. C*, 92(1):015503, 2015.
- [37] J. B. Albert et al. (EXO-200 Collaboration). Improved measurement of the $2\nu\beta\beta$ half-life of ^{136}Xe with the EXO-200 detector. *Phys. Rev. C*, 89(1):015502, 2014.

- [38] S. Al Kharusi et al. (nEXO Collaboration). nEXO Pre-Conceptual Design Report. arXiv:1805.11142 [physics.ins-det], 2018.
- [39] C. Jillings. The SNOLAB science program. *J. Phys.: Conf. Ser.*, 718(062028), 2016.
- [40] M. K. Moe. Detection of neutrinoless double-beta decay. *Phys. Rev. C*, 44:R931–R934, Sep 1991.
- [41] K. Twelker and S. Kravitz for the EXO Collaboration. Barium tagging from nEXO using resonance ionization spectroscopy. *Physics Procedia*, 61:278 – 282, 2015. 13th International Conference on Topics in Astroparticle and Underground Physics, TAUP 2013.
- [42] T. Brunner et al. An RF-only ion-funnel for extraction from high-pressure gases. *Int. J. Mass Spectrometry*, 379:110, 2015.
- [43] B. Mong et al. Spectroscopy of Ba and Ba⁺ deposits in solid xenon for barium tagging in nEXO. *Phys. Rev. A*, 91(2):022505, 2015.
- [44] A. Kramida, Yu. Ralchenko, J. Reader, and NIST ASD Team. NIST Atomic Spectra Database (ver. 5.6.1), [Online]. Available: <https://physics.nist.gov/asd> [2019, February 7]. National Institute of Standards and Technology, Gaithersburg, MD., 2018.
- [45] V.A. Dzuba and J.S.M. Ginges. Calculations of energy levels and lifetimes of low-lying states of barium and radium. *Phys. Rev. A*, 73(032503), 2006.
- [46] J. Migdalek and W.E. Baylis. Multiconfiguration Dirac-Fock calculations of two electric quadrupole transitions in neutral barium. *Phys. Rev. A*, 42(6897), 1990.
- [47] S. Niggli and M. C. E. Huber. Transition probabilities in neutral barium. *Phys. Rev. A*, 35:2908–2918, Apr 1987.
- [48] S. De, U. Dammalapati, K. Jungmann, and L. Willmann. Magneto-optical trapping of barium. *Phys. Rev. A*, 79:041402, Apr 2009.

- [49] T. Walton. *Imaging Single Barium Atoms in Solid Xenon for Barium Tagging in the nEXO Neutrinoless Double Beta Decay Experiment*. PhD dissertation, Colorado State University, 2016.
- [50] V.E. Bondybey, A.M. Smith, and J. Agreiter. New developments in matrix isolation spectroscopy. *Chem. Rev.*, 96, 1996.
- [51] F.O. Ellison. A method of diatomics in molecules. I. general theory and application to H_2O^1 . *J. Am. Chem. Soc.*, 85(3540), 1963.
- [52] F. London. The general theory of molecular forces. *Trans. Faraday Soc.*, 33:8b–26, 1937.
- [53] H. Hellmann. A new approximation method in the problem of many electrons. *J. Chem. Phys.*, 3(1):61–61, 1935.
- [54] W. E. Baylis. Semiempirical, pseudopotential calculation of alkali noble gas interatomic potentials. *J. Chem. Phys.*, 51(6):2665–2679, 1969.
- [55] E. Whalley and W. G. Schneider. Intermolecular potentials of argon, krypton, and xenon. *J. Chem. Phys.*, 23(9):1644–1650, 1955.
- [56] H Harima, K Tachibana, and Y Urano. Empirical interatomic potentials for Ba-rare-gas systems deduced from an absorption measurement. *J. Phys. B*, 15(20):3679–3693, oct 1982.
- [57] N. Runeberg and P. Pyykkö. Relativistic pseudopotential calculations on Xe_2 , RnXe , and Rn_2 : The van der Waals properties of radon. *International Journal of Quantum Chemistry*, 66(2):131–140.
- [58] B. Davis and J. McCaffrey. Absorption spectroscopy of heavy alkaline earth metals Ba and Sr in rare gas matrices - CCSD(T) calculations and atomic site occupancies. *J. Chem. Phys.*, 144(044308), 2016.
- [59] Alexei A. Buchachenko and Larry A. Viehland. Interaction potentials and transport properties of Ba, Ba^+ , and Ba^{2+} in rare gases from He to Xe. *J. Chem. Phys.*, 148(15):154304, 2018.

- [60] John C. Tully. Diatomics in molecules potential energy surfaces. I. first-row triatomic hydrides. *J. Chem. Phys.*, 58(4):1396–1410, 1973.
- [61] Marie-Catherine Heitz, Laurent Teixidor, Nguyen-Thi Van-Oanh, and Fernand Spiegelman. Relaxation dynamics of photoexcited calcium deposited on argon clusters: Theoretical simulation of time-resolved photoelectron spectra. *J. Phys. Chem. A*, 114(9):3287–3296, 2010.
- [62] A. I. Krylov, R. B. Gerber, M. A. Gaveau, J. M. Mestdagh, B. Schilling, and J. P. Visticot. Spectroscopy, polarization and nonadiabatic dynamics of electronically excited Ba(Ar)_n clusters: Theory and experiment. *J. of Chem. Phys.*, 104(10):3651–3663, 1996.
- [63] Philip M. Morse. Diatomic molecules according to the wave mechanics. II. vibrational levels. *Phys. Rev.*, 34:57–64, Jul 1929.
- [64] J. Franck and E. G. Dymond. Elementary processes of photochemical reactions. *Trans. Faraday Soc.*, 21:536–542, 1926.
- [65] Edward Condon. A theory of intensity distribution in band systems. *Phys. Rev.*, 28:1182–1201, Dec 1926.
- [66] H. A. Jahn and E. Teller. Stability of polyatomic molecules in degenerate electronic states. I. orbital degeneracy. *Proc. R. Soc. Lond. A*, 161(905), 1937.
- [67] B. Gervais B. Davis and J. McCaffrey. An investigation of the sites occupied by atomic barium in solid xenon - A 2D-EE luminescence spectroscopy and molecular dynamics study. *J. Chem Phys.*, 148(124308), 2018.
- [68] J. Rose, D. Smith, B. E. Williamson, P. N. Schatz, and M. C. M. O’Brien. Magnetic circular dichroism and the Jahn-Teller effect in the $^2S \rightarrow ^2P$ transition of sodium and lithium atoms isolated in xenon matrixes. *J. Phys. Chem.*, 90(12):2608–2615, 1986.
- [69] Y. Sonnenblick, Z.H. Kalman, and I.T. Steinberger. Growth and crystal structures of solid xenon and krypton. *Journal of Crystal Growth*, 58(1):143 – 151, 1982.

- [70] J. G. McCaffrey. private communication.
- [71] Derek C. Silverman and Mario E. Fajardo. Matrix isolation spectroscopy of Na atoms deposited as Na^+ ions. *J. Chem. Phys.*, 106(22):8964–8966, 1997.
- [72] Ronald A. Aziz and M.J. Slaman. The argon and krypton interatomic potentials revisited. *Molecular Physics*, 58(4):679–697, 1986.
- [73] Simon Tam and Mario E. Fajardo. Matrix isolation spectroscopy of metal atoms generated by laser ablation. III. the Na/Ar, Na/Kr, and Na/Xe systems. *J. Chem. Phys.*, 99(2):854–860, 1993.
- [74] K. Vaskonen, J. Eloranta, and H. Kunttu. Trapping of laser-vaporized alkali metal atoms in rare-gas matrices. *Chem. Phys. Lett.*, 310:245–251, September 1999.
- [75] Jussi Ahokas, Toni Kiljunen, Jussi Eloranta, and Henrik Kunttu. Theoretical analysis of alkali metal trapping sites in rare gas matrices. *J. Chem. Phys.*, 112(5):2420–2426, 2000.
- [76] G. Reza Ahmadi, J. Almlöf, and I. Røeggen. The interatomic potential for the $X1\sigma^+$ state of ArNa^+ , NeNa^+ and HeNa^+ . *Chem. Phys.*, 199(1):33 – 52, 1995.
- [77] B. Gervais. private communication.
- [78] W H. Breckenridge and Clifton Merrow. Exclusive production of $\text{Ba}(6s6p\ ^3\text{P}_2)$ in the collisional deactivation of $\text{Ba}(6s6p\ ^1\text{P}_1)$ by the rare gases. *J. Chem. Phys.*, 88:2329–2333, 02 1988.
- [79] Dmitry S. Bezrukov, Nadezhda N. Kleshchina, Inna S. Kalinina, and Alexei A. Buchachenko. Ab initio interaction potentials of the Ba, Ba^+ complexes with Ar, Kr, and Xe in the lowest excited states. *J. Chem. Phys.*, 150(6):064314, 2019.
- [80] M. Menzinger and L. Wahlin. High intensity, low energy spread ion source for chemical accelerators. *Rev. Sci. Inst.*, 40(102), 1969.

- [81] Beam Imaging Solutions.
- [82] R. LaBelle. *Isotopically selective atom counting using photon burst mass spectroscopy*. PhD dissertation, Colorado State University, 1993.
- [83] R. D. LaBelle, W. M. Fairbank, and Richard A. Keller. Detection of fast Mg ions using the photon-burst method. *Phys. Rev. A*, 40:5430–5433, Nov 1989.
- [84] Paul C. Beaumont, David G. Johnson, and Barry J. Parsons. Photophysical properties of laser dyes: picosecond laser flash photolysis studies of rhodamine 6G, Rhodamine B and Rhodamine 101. *J. Chem. Soc., Faraday Trans.*, 89:4185–4191, 1993.
- [85] J.-P. Taché. Ray matrices for tilted interfaces in laser resonators. *Appl. Opt.*, 26(3):427–429, Feb 1987.
- [86] T.H. Maiman. Stimulated optical radiation in ruby. *Nature*, 187(4736), 1960.
- [87] C. Chambers et al. (nEXO Collaboration). Imaging individual barium atoms in solid xenon for barium tagging in nEXO. *Accepted for publication in Nature*, arXiv:1806.10694, 2019.
- [88] S. Cook. *Detection of small numbers of barium atoms implanted in solid xenon for the EXO experiment*. PhD dissertation, Colorado State University, 2012.